

Magnetism of Individual Adatoms and of Epitaxial Monolayers

THÈSE N° 4411 (2009)

PRÉSENTÉE LE 5 JUIN 2009

À LA FACULTÉ SCIENCES DE BASE

LABORATOIRE DE NANOSTRUCTURES SUPERFICIELLES

PROGRAMME DOCTORAL EN PHYSIQUE

ÉCOLE POLYTECHNIQUE FÉDÉRALE DE LAUSANNE

POUR L'OBTENTION DU GRADE DE DOCTEUR ÈS SCIENCES

PAR

Anne LEHNERT

acceptée sur proposition du jury:

Prof. O. Schneider, président du jury

Prof. H. Brune, directeur de thèse

Dr C. Carbone, rapporteur

Prof. M. Schmid, rapporteur

Prof. W.-D. Schneider, rapporteur



ÉCOLE POLYTECHNIQUE
FÉDÉRALE DE LAUSANNE

Suisse
2009

Abstract

This thesis reports on the magnetism of low coordinated Fe and Co atoms in different chemical and electronic environments. The objective of this research was to contribute to the fundamental understanding of the magnetic properties, such as magneto-crystalline anisotropy energy (MAE), orbital and spin magnetic moment, of surface supported transition metal (TM) atoms and one atomic layer thick epitaxial TM films. A detailed knowledge on the interplay of electronic hybridization and magnetic properties is mandatory to elaborate new materials with high perpendicular magnetic anisotropy and acceptable writing field for future use in magnetic recording devices. The magnetic properties of the different experimental systems were investigated by x-ray absorption spectroscopy, x-ray magnetic circular dichroism, and magneto-optical Kerr effect (MOKE) and they were correlated to the morphology obtained by scanning tunneling microscopy (STM).

The first part focuses on the effect of electronic hybridization between isolated $3d$ TM atoms and different kinds of substrates. First, we considered $4d$ and $5d$ TM substrates known for their high magnetic polarizability due to the close onset of ferromagnetism. Deposition of single Fe and Co atoms on Rh(111), Pd(111), and Pt(111) produces an increasing MAE going from Rh to Pd and finally to Pt that we directly correlate to the increasing spin-orbit constant of the substrate interlinking the induced magnetic moment and the MAE. Further we investigated single Fe and Co atoms on two different insulating layers, namely $\text{Al}_2\text{O}_3/\text{Ni}_3\text{Al}(111)$ and $\text{Cu}_2\text{N}/\text{Cu}(001)$, providing an efficient decoupling of the TM $3d$ states from the conduction electrons of the substrates. In case of the alumina film the absorption spectra of Fe and Co show a pronounced multiplet structure. On Cu_2N the multiplet features of the adatoms are less defined due to the lower thickness of the screening layer. On both insulating layers we find a common out-of-plane easy axis, highly unquenched orbital moments, and giant MAE values of several meV/atom which are due to the formation of strong anisotropic bonds with the O and N atoms, respectively.

The second part is dedicated to single atom thick layers of Fe and Co deposited on Pt(111) and Rh(111). We find the MAE to be strongly enhanced compared with bulk and we establish a direct proportionality between the induced magnetic moment of the topmost substrate layer and the MAE. The study of bimetallic $\text{Fe}_{1-x}\text{Co}_x$ alloys on platinum reveal

a material with high MAE (0.5 meV at the equiatomic composition), large saturation magnetization ($3 \mu_B$ to $2\mu_B$ going from Fe to Co), and perpendicular magnetization easy axis. These characteristics hint at new possibilities for the further miniaturization of the grain size in recording devices.

In the last part the theoretical description of the MOKE for ultra-thin films is extended to the transverse geometry and improved analytic formulae for the polar and longitudinal geometry are presented. This finding was used to optimize the Kerr signal for a new MOKE setup which is fully integrated in an ultrahigh vacuum chamber combining *in situ* MOKE and STM. The setup performance was demonstrated for a continuous film of 0.9 monolayers (ML) Co/Rh(111) with in-plane easy axis and for a superlattice of nanometric double layer Co islands on Au(11,12,12) with out-of-plane easy axis. The detection limit is 0.5 ML for transverse and 0.1 ML for polar Kerr geometry corresponding for island superlattices with the density of Co/Au(11,12,12) to islands composed of about 50 atoms. Moreover, the setup holds two independent ways to measure the MAE which is either by thermally induced magnetization reversal or by applying a torque onto the magnetization by turning the magnetic field. Both ways yield similar results for 1.1 ML Co/Au(11,12,12).

Keywords : magnetic impurities, magnetic thin films, magnetic anisotropy, iron, cobalt, gold, rhodium, palladium, platinum, x-ray magnetic circular dichroism (XMCD), magneto-optical Kerr effect (MOKE), scanning tunneling microscopy (STM)

Version abrégée

Cette thèse porte sur le magnétisme des atomes de Fe et de Co de basse coordination en différents environnements chimiques et électroniques. L'objectif de cette étude a été la contribution aux connaissances fondamentales des propriétés magnétiques des métaux de transition (MT) $3d$ sous forme d'atomes isolés et des couches minces en surface par la mesure de l'énergie d'anisotropie magnétocristalline (MAE), le moment de spin et le moment orbital. Une bonne connaissance de l'impact de l'hybridisation électronique sur les propriétés magnétiques est nécessaire pour créer des nouveaux matériaux avec une anisotropie perpendiculaire élevée et une haute densité d'aimantation qui paraissent actuellement les meilleurs candidats pour les mémoires magnétiques. Dans ce but, nous avons réalisé des mesures de spectroscopie d'absorption de rayons X, de dichroïsme magnétique circulaire de rayons X (XMCD) et d'effet Kerr magnéto-optique (MOKE). Celles-ci ont été corrélées à la morphologie obtenue par la microscopie à effet tunnel (STM).

Dans une première partie, nous avons essayé relever l'effet de l'hybridisation électronique entre des atomes isolés de Fe et de Co et différents types de substrats. Nous avons tout d'abord considéré des MT $4d$ et $5d$ qui sont sous forme volumique proche de satisfaire le critère d'ordre ferromagnétique. Nous trouvons que la MAE des atomes de Fe et de Co change avec la nature du substrat sur lequel ils sont déposés: elle est d'autant plus importante partant du Rh(111), puis Pd(111) jusqu'au Pt(111). Cette augmentation reflète l'augmentation du couplage spin-orbite, qui relie le moment magnétique induit et la MAE. Nous avons ensuite étudié des atomes isolés de Fe et de Co sur des couches isolantes, dont une est le Al_2O_3 sur le $\text{Ni}_3\text{Al}(111)$ et l'autre le Cu_2N sur le $\text{Cu}(001)$, qui découplent effectivement les états $3d$ des MT des électrons de conduction du substrat. Dans le cas de l'alumine les spectres d'absorption de Fe et de Co montrent une structure prononcée de multiplet qui est moins marquée sur le nitrite de cuivre, en raison de l'épaisseur plus faible de la couche Cu_2N . Hormis cette différence, nous trouvons sur les deux isolants un axe facile d'aimantation hors-plan, des moments orbitaux importants et des MAE atteignant quelques meV/atome. Ces MAE géantes sont dues à la formation des liaisons fortes et anisotropes avec l'oxygène respectivement l'azote.

La deuxième partie porte sur les propriétés magnétiques de monocouches de Fe et de

Co déposées sur le Pt(111) et le Rh(111). Ces systèmes présentent une MAE beaucoup plus importante que dans le matériau massif ainsi qu'une relation directe entre le moment induit dans la couche supérieure du substrat et la MAE. L'étude des alliages bimétalliques $\text{Fe}_{1-x}\text{Co}_x$ sur le platine montre toutes les caractéristiques nécessaires pour l'enregistrement magnétique. Nous mesurons en effet une forte MAE (0.5 meV pour $\text{Fe}_{0.5}\text{Co}_{0.5}$), un moment magnétique important (entre $3\mu_B$ et $2\mu_B$ passant de Fe à Co) et un axe facile hors-plan. Ces résultats suggèrent de pousser les limites dans la miniaturisation, dans la même direction que les dispositifs de stockage magnétique.

Le point de départ de la dernière partie est la théorie du MOKE en général qui est ensuite appliquée aux couches fines. Nous réexaminons qualitativement la rotation et l'ellipticité Kerr et nous redécrivons leurs expressions pour la configuration polaire, longitudinale et transverse. Nous discutons ensuite cette dérivation pour optimiser le signal Kerr pour une nouvelle expérience MOKE qui est placée dans une enceinte à ultrahaut vide. Ce dispositif combine des mesures MOKE et STM *in situ*. La performance de la nouvelle expérience est démontrée à l'aide d'une couche continue de 0.9 monocouches (MC) Co/Rh(111) ayant une axe facile dans le plan et un réseau d'îlots double couches nanométriques de Co sur Au(11,12,12). La limite de détection établie est de 0.5 MC en configuration transverse et de 0.1 MC en configuration polaire ce qui correspond à une taille de 50 atomes/îlot pour un réseau de nano-îlots de même densité que celle pour Co/Au(11,12,12). Dans cette gamme de sensibilité la nouvelle expérience présente l'avantage unique de disposer de deux façons indépendantes pour mesurer la MAE. La première se base sur le renversement d'alimentation activé thermiquement et la deuxième sur l'application d'un couple sur le moment magnétique en tournant le champ appliqué. Les deux donnent des résultats comparables pour 1.1 MC Co/Au(11,12,12).

Mots clés : impuretés magnétiques, couche mince magnétique, anisotropie magnétique, fer, cobalt, or, rhodium, palladium, platine, dichroïsme magnétique circulaire de rayons X (XMCD), effet Kerr magnéto-optique (MOKE), microscopie à effet tunnel (STM)

Contents

1	Introduction	1
2	XAS, XMCD, and XMLD	5
2.1	X-ray absorption spectroscopy	5
2.2	XAS with circularly polarized light	9
2.3	XAS with linearly polarized light	13
3	Magnetism of Single Atoms	15
3.1	Fe and Co single atoms on Rh(111), Pd(111), and Pt(111)	17
3.2	Fe and Co single atoms on Al ₂ O ₃ /Ni ₃ Al(111)	22
3.2.1	Oxygen adsorption and oxide formation on Ni ₃ Al(111)	22
3.2.2	Magnetic properties of Al ₂ O ₃ on Ni ₃ Al(111)	23
3.2.3	Isolated Fe and Co atoms	24
3.2.4	Beam induced change of the XAS white line	27
3.2.5	Larger Fe clusters	30
3.3	Cu ₂ N	32
3.3.1	Sample Preparation	34
3.3.2	Single Fe and Co atoms on Cu ₂ N/Cu(001)	34
3.3.3	XMCD versus IETS results	39
4	Co and Fe ultra-thin films on highly polarizable substrates	41
4.1	Fe _x Co _{1-x} monolayers on Pt(111)	43
4.1.1	Structural results from STM	44
4.1.2	XAS on granular Fe _x Co _{1-x} films	46
4.1.3	MOKE of continuous Fe _x Co _{1-x} films	49
4.1.4	Experiment versus theory	50
4.1.5	Electronic structure analysis	52
4.2	Fe and Co on Rh(111)	56
4.2.1	XAS and XMCD study of 1 ML thick granular films	57
4.2.2	MOKE of granular and continuous films	61

4.2.3	Experimental results of Co and Fe multi-layers	62
4.2.4	MOKE of continuous $\text{Fe}_x\text{Co}_{1-x}$ monolayer films on Rh(111)	64
4.2.5	Experiment versus theory	64
4.3	Conclusions	66
5	Magneto - Optical Kerr Effect	69
5.1	Historical Introduction	69
5.1.1	Faraday effect	70
5.1.2	Kerr effect	71
5.2	Analytical and Numerical Solution of the Maxwell Equations	72
5.2.1	The thin film limit	76
5.2.2	The thick film limit	79
5.3	UHV compatible MOKE setup	79
5.4	First Measurements	86
5.4.1	Co/Rh(111)	86
5.4.2	Co/Au(11 12 12)	89
6	Conclusions and Perspectives	93
A	Spherical harmonics for s, p, and d orbitals	95
B	Faraday Rotation	99
	Bibliography	101

Chapter 1

Introduction

The phenomenon magnetism is known for hundreds of years (about 600 BC) by describing the attractive force of lodestone on iron. The name lodestone (*lode* being old English for to lead) used for a certain form of magnetite, comes up in connection with its use for navigation leading mariners on the ocean. The property of a material to align in an external magnetic field (for a compass needle it is the earth's magnetic field) can be traced down to the atomic scale. Whether a material is at the end magnetic depends on *i*) if the composing atoms are magnetic and *ii*) how the atoms arrange within the crystal. The arrangement of magnetic atoms with respect to each other is classified as ferro-, ferri-, and antiferromagnetism. When regarding a free atom we realize that its magnetic moment is determined by quantum-mechanical laws summarized in a set of rules going under Hund's name. For a filled or empty atomic shell the moment is zero, but for partially filled electronic shell a non-zero moment results. According to Hund's rules almost all elements of the periodic table have a non-zero magnetic moment. This concept of quantum behavior was demonstrated in the famous experiment by Stern and Gerlach who directed a beam of silver atoms through an inhomogeneous magnetic field and observed two separated Ag spots on the detection screen. Ag has 47 electrons and the outer 5s electron is unpaired giving rise to a spin-only magnetic moment. In solid state, however, *ferromagnetism* persists only for a few elements, namely iron, cobalt, nickel, and gadolinium.

In between the atomic and bulk limit matter is known to behave in a non straight-forward predictable way. A colorful example are Au nanoparticles having an intense red color for diameters less than 100 nm. Already the Romans added gold salts to their sand and soda ash mixtures and found that by careful annealing they could produce a red transparent glass that was used to decorate church windows. There are numerous other examples of modified material properties in reduced dimensions. Here, we concentrate on the magnetic properties of low coordinated atoms either as a surface supported single atom or in a one atom thick epitaxial film.

Magnetic single atoms at surfaces can exhibit anisotropies that are large enough to maintain a stable spin orientation at low temperatures. The large anisotropies are of interest as a possible way to shrink magnetic bits below the size at which the domain magnetization direction in current thin-film magnetic materials become unstable at room temperature. Besides this technological relevance, magnetic single atoms are of great scientific interest as simple model systems. Their well-known local environment makes them better understandable and comparison with theory more direct [1, 2, 3, 4, 5, 6]. Surface supported single atoms may be described with either classical or quantum behavior [1, 7, 8, 9, 10, 11]. In a classical picture, the stability of the magnetization direction is determined by the size of the magneto-crystalline anisotropy energy (MAE) limiting the probability of thermally induced magnetization reversal. In quantum systems, tunneling can cause discrete changes of the magnetization, eventually leading to a finite, temperature-independent probability for switching [10].

In the limit of single atoms, appropriate tools to study their magnetic properties are needed. Owing to X-ray magnetic circular dichroism (XMCD) developed in the 1990s [12, 13, 14, 15, 16] we are today able to probe the magnetic properties of concentrations as small as 0.002 monolayers (ML) [17], where we define 1 ML as the density of atoms in the topmost layer of the substrate. XMCD allows to extract independently the orbital and spin magnetic moment as well as to probe the MAE which is a major advantage compared with other magnetometry tools, solely able to measure the total magnetic moment [15, 18, 19, 20, 21]. Still, the typical size of a x-beam is of the order of a few hundred μm^2 which makes XMCD a spatially averaging technique. To get information on single atoms or clusters a mandatory requirement is the fabrication of well defined ensembles, such as surfaces with only single atoms or monodisperse clusters each of them in an identical environment with sufficient mutual distance to exclude interactions [1, 22, 11]. The realization of such samples is one of the challenges is surface science nowadays. Comparing results from XMCD with new local techniques helps gaining a clearer and deeper understanding in the magnetic properties at the atomic scale [23, 9, 24, 10, 17, 6].

Increasing the lateral coordination by considering two dimensional nanostructures or single atom thick films, we have one more degree of freedom namely the lattice mismatch between the nanostructure or film and the substrate. Lattice distortions may decide about the magnetic order as it is observed for 1 ML Fe on Rh where the (001) surface produces antiferromagnetic order [25] while the (111) surface leads to ferromagnetic order (this work). Co/Ru(0001) shows a spin-reorientation from in-plane for 1 ML to out-of-plane for 2 ML which is associated with structural relaxation [26]. Similarly, CoO films grown on different substrates reveal a change in magnitude and orientation of the magnetic moments as a function of the strain in the films induced by the substrate [27]. Furthermore, the creation of disordered bimetallic alloys or carefully designed bimetallic islands open up viable routes to design new materials with large MAE and saturation

magnetization [28, 29, 30].

In chapter 2 we review the fundamentals of x-ray absorption spectroscopy (XAS), x-ray magnetic circular dichroism (XMCD) and x-ray magnetic linear dichroism (XMLD). The experimental setup is described and by means of a pair of measured XAS the data analysis process is exemplified and the sum rules presented.

In chapter 3 we present XMCD studies of single Fe and Co atoms on different metallic and insulating substrates in order to investigate the influence of adatom-substrate electronic hybridization on the magnetic properties. On the $4d$ respectively $5d$ transition metal surfaces Rh(111), Pd(111), and Pt(111) we are specially interested in the effect of the induced magnetic moment contributing via spin-orbit coupling to the MAE. The spin-orbit coupling constant increases from Rh over Pd to Pt which is expected to be reflected in the strength of the MAE [1, 31]. The insulating surface layers Al_2O_3 and Cu_2N strongly limit the hybridization of the adatom's $3d$ electrons with the conduction electrons of the substrate. For example, atomic spin values were found for Fe and Co on Cu_2N using IETS [9, 32]. Hence, we can consider Al_2O_3 and Cu_2N as prototypes for nano-insulators due to their limited thickness of only 2 ML and 1 ML, respectively. Moreover, a large MAE of 6.2 meV/Fe atom and 6.2 meV/Co atom was deduced from the excitation spectra. We intend to compare the IETS results with XMCD which allows to obtain in addition to the spin moment the orbital magnetic moment which is supposed to play a major role in the anisotropic behavior [33].

Chapter 4 is mainly dedicated to single atom thick layers of Fe and Co deposited on Pt(111) and Rh(111). Pt is a $5d$ transition metal whereas Rh is $4d$ one, both having slightly different lattice parameters (3.92 Å for Pt and 3.80 Å for Rh) and electronic ground states (both have 1s electron, Pt has 9 d electrons and Rh 8). We investigated the magnetic properties with XMCD and MOKE that we correlate to the morphology using STM. We compare the magnetic properties of the ML films with those of the single atoms discussed in chapter 3. Further, we studied $\text{Fe}_x\text{Co}_{1-x}$ monolayers on Pt(111) because for distorted FeCo alloys an exceptional large MAE close to 1 meV/atom has been found [34, 35]. The maximum MAE is at about 60% Co content while the maximum magnetic moment is found for 30% Co. Theoretic investigations were carried out in the group of P. Weinberger for $\text{Fe}_x\text{Co}_{1-x}/\text{Pt}(111)$ and in the one of J. Hafner for Fe and Co on Rh(111).

In chapter 5 the fundamentals of the magneto-optical kerr effect (MOKE) are given and the theoretical description for ultra-thin films is extended to the transverse geometry and improved formulae for the polar and longitudinal geometry are presented. This finding was used to optimize the Kerr signal for a new MOKE setup which is fully integrated in an ultrahigh vacuum chamber combining *in situ* MOKE and STM. We describe the setup and demonstrate its coverage detection limit on the basis of a continuous film of 0.9 monolayers (ML) of Co/Rh(111) with in-plane easy axis and for a superlattice of

nanometric double layer Co islands on Au(11,12,12) with out-of-plane easy axis. The vector-field generated by a four pole electromagnet allows us to apply a torque on the magnetization M by turning the magnetic field by an angle α . Measuring M *vs.* α allows us to infer the MAE and to compare it with the one obtained from thermally induced magnetization reversal.

Chapter 2

XAS, XMCD, and XMLD

In this chapter the theoretical background of x-ray absorption spectroscopy (XAS), x-ray magnetic circular dichroism (XMCD), and x-ray magnetic linear dichroism (XMLD) is given. The clear advantage of soft x-rays in probing magnetism is the element specificity which is due to the strong localization of the core levels and allows to trace the origin of the magnetic properties. The spectral line shape sheds light on the chemical environment and electronic state of the probed atom. Furthermore, XAS is a quantitative tool allowing the separate determination of the orbital magnetic moment L and the spin magnetic moment S using sum rules.

2.1 X-ray absorption spectroscopy

The property of matter to absorb light or more general electromagnetic waves with any wavelength is well known. Empirically, x-ray absorption obeys an exponential decay law with distance. The intensity I diminishes with the penetration depth z according to

$$I = I_0 e^{-\mu z} \quad (2.1)$$

where I_0 is the intensity at the surface ($z = 0$) and μ the absorption coefficient. μ is a function of the incident photon energy and this function is characteristic for each material whereof XAS takes advantage.

X-ray absorption is a purely quantum mechanical process which involves the transition of a core electron to an empty valence state. The transition probability $w_{i \rightarrow f}$ per unit time from an initial state i to a final state f is known as Fermi's Golden rule [36]:

$$w_{i \rightarrow f} = \frac{2\pi}{\hbar} |\langle f | \mathcal{H}_{int} | i \rangle|^2 \delta(\varepsilon_f - \varepsilon_i - \hbar\omega). \quad (2.2)$$

\mathcal{H}_{int} describes the photon-electron interaction and the delta function $\delta(\varepsilon_f - \varepsilon_i - \hbar\omega)$ guarantees that a transition takes only place if the photon energy $\hbar\omega$ matches the energy

difference between the initial state ε_i and the final state ε_f . The interaction hamiltonian is

$$\mathcal{H}_{int} = \frac{e}{m_e} \mathbf{p} \cdot \mathbf{A} \quad (2.3)$$

where e is the electron's charge, m_e its mass, \mathbf{p} the electron momentum operator, and \mathbf{A} the vector potential of the photon field. In free space the relation between \mathbf{A} and the electric field \mathbf{E} is $\mathbf{E} = -\partial\mathbf{A}/\partial t$. For an incident plane electromagnetic wave \mathbf{A} writes

$$\mathbf{A} = A_0 \mathcal{E} e^{i\mathbf{k}\mathbf{r}} \quad (2.4)$$

where A_0 is the vector potential amplitude and \mathcal{E} a unit vector giving the polarization. In the electric dipole approximation only the first term of the Taylor expansion of $e^{i\mathbf{k}\mathbf{r}}$ is kept. Neglecting higher order terms is reasonable for a photon energy range up to $\hbar\omega = 1000$ eV. We further use the commutation law $\mathbf{p} = m_e/i\hbar[\mathbf{r}, H]$ to obtain finally

$$w_{i \rightarrow f} = \frac{2\pi}{\hbar} e^2 |A_0|^2 \frac{(\varepsilon_f - \varepsilon_i)^2}{\hbar^2} |\langle f | \mathcal{E} \mathbf{r} | i \rangle|^2 \delta(\varepsilon_f - \varepsilon_i - \hbar\omega). \quad (2.5)$$

The absorption cross section is defined as the ratio $w_{i \rightarrow f} \cdot \hbar\omega$ divided by $2\varepsilon_0 c |A_0|^2 \omega^2$. $w_{i \rightarrow f} \cdot \hbar\omega$ is the energy removed from the incident beam by the photoelectric effect and $2\varepsilon_0 c |A_0|^2 \omega^2$ the energy of the photon beam crossing a unit area perpendicular to the propagation direction [37]. The energy integral over the absorption cross section yields the polarization dependent resonant X-ray absorption intensity

$$I_{res} = 4\pi^2 \frac{e^2}{4\pi\varepsilon_0 \hbar c} \hbar\omega |\langle f | \mathcal{E} \mathbf{r} | i \rangle|^2 \quad (2.6)$$

where $\frac{e^2}{4\pi\varepsilon_0 \hbar c} = \frac{1}{137}$ is the fine structure constant. The remaining task is to calculate the transition matrix element $\langle f | \mathcal{E} \mathbf{r} | i \rangle$. $\mathcal{E} \mathbf{r}$ is a tensor operator and writes

$$z = r \sqrt{\frac{4\pi}{3}} Y_{1,0} \quad \text{for linear polarization,} \quad (2.7)$$

$$\frac{1}{\sqrt{2}}(x + iy) = r \sqrt{\frac{4\pi}{3}} Y_{1,1} \quad \text{for right circular polarization, and} \quad (2.8)$$

$$\frac{1}{\sqrt{2}}(x - iy) = r \sqrt{\frac{4\pi}{3}} Y_{1,-1} \quad \text{for left circular polarization.} \quad (2.9)$$

$Y_{l,m_l}(\vartheta, \phi)$ are the well-known spherical harmonics [36]. The operator $(x \pm iy)$ can be expressed as V_{\pm} and the z operator as V_z [38]. According to the Wigner-Eckart-Theorem the matrix element $\langle f | \mathcal{E} \mathbf{r} | i \rangle$ is non-zero only if the orbital quantum number l of the final state differs by 1 from the initial state, and $\Delta m_l = +1$ for right circular polarization, $\Delta m_l = -1$ for left circular polarization, and $\Delta m_l = 0$ for linear polarization. The spin is unaffected; hence, $\Delta s = 0$. The dipole selection rules entail the following possible transitions for the 3d and 4d transition metals:

K	$1s$	\rightarrow	$4p_{1/2}$
L_2	$2p_{1/2}$	\rightarrow	$4s, 3d_{3/2}$
L_3	$2p_{3/2}$	\rightarrow	$4s, 3d_{3/2}, 3d_{5/2}$
M_2	$3p_{1/2}$	\rightarrow	$5s, 4d_{3/2}$
M_3	$3p_{3/2}$	\rightarrow	$5s, 4d_{3/2}, 4d_{5/2}$

A simple picture of x-ray absorption gives the so-called one-electron model, which neglects all "passive", i.e. not directly involved, electrons in the absorption process. Within the one-electron model Erskin and Stern predict a XMCD signal for Ni and suggest a synchrotron radiation source to conduct the experiments [39]. Their model it is quite intuitive and often used in x-ray absorption literature, as we will do in the following.

The initial state $|i\rangle$ and final state state $|f\rangle$ are treated as atomic wave functions and only the initial state is treated relativistically, i.e. with spin-orbit coupling. For the final state the complete basis functions are

$$|f\rangle = |R_{n',l'}(r); l', m'_l, s', m'_s\rangle = R_{n',l'}(r) Y_{l',m'_l}(\vartheta, \varphi) \chi_{s',m'_s} \quad (2.10)$$

where $R_{n,l}(r)$ is the radial component, $Y_{l,m_l}(\vartheta, \varphi)$ the angular part and χ_{s,m_s} the spin part. n, l, m_l, s, m_s are the eigenvalues of the complete set of commuting observables $\{H, \mathbf{L}^2, L_z, \mathbf{S}^2, S_z\}$ specifying the quantum state of the system. For the initial state, the spin-orbit coupling of the core levels makes m_l and m_s no longer good quantum numbers and the angular momentum operators $\mathbf{J} = \mathbf{L} \pm \mathbf{S}$ and \mathbf{M} with the eigenvalues $j = l \pm s$ and m_j are introduced [36]. The basis functions of the initial state are

$$|i\rangle = |R_{n,l}(r); j, m_j, l, s\rangle = \sum_{m_l, m_s} |R_{n,l}(r); l, m_l, s, m_s\rangle \langle l, m_l, s, m_s | j, m_j\rangle \quad (2.11)$$

where $C_{l,m_l} = \langle l, m_l, s, m_s | j, m_j\rangle$ are the Clebsch-Gordan coefficients. Explicit forms of the initial state wave functions and the spherical harmonics are given in the appendix A. In order to calculate

$$\left| \sum_{m_l} C_{l,m_l} \langle R_{n',l'}(r); l', m'_l, s', m'_s | \mathcal{E} \mathbf{r} | R_{n,l}(r); l, m_l, s, m_s \rangle \right|^2 \quad (2.12)$$

we can evaluate separately

$$\delta(m_s, m'_s) \quad \text{the spin part,} \quad (2.13)$$

$$\langle R_{n',l'}(r) | r | R_{n,l}(r) \rangle \quad \text{the radial part, and} \quad (2.14)$$

$$\langle l', m'_l | \mathcal{E} \frac{\mathbf{r}}{r} | l, m_l \rangle \quad \text{the angular part.} \quad (2.15)$$

The spin part is the usual delta function. The radial part is

$$\mathcal{R} = \langle R_{n',l'}(r) | r | R_{n,l}(r) \rangle = \int_0^\infty R_{n',l'}^*(r) R_{n,l}(r) r^3 dr. \quad (2.16)$$

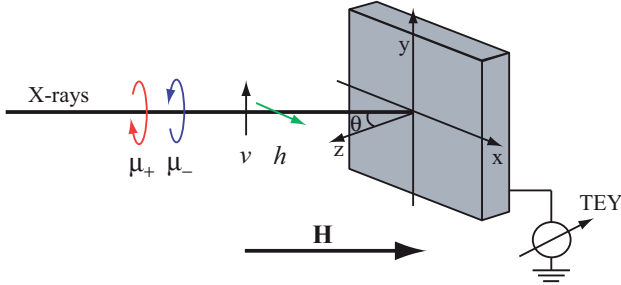


Figure 2.1: Sketch of the experimental setup. The incoming x-ray beam is parallel to the applied field \mathbf{H} . The angle included in between the surface normal and the applied field vector is called θ .

\mathcal{R} is strongly localized in the core region and gives x-ray absorption spectroscopy its elemental specificity. The angular part will be evaluated for circularly and linearly polarized light in the following two sections.

Experimentally, the most direct way to measure x-ray absorption is the transmission method requiring for soft x-rays an extremely thin sample [15]. We use bulk samples and measure x-ray absorption therefore indirectly in the total electron yield (TEY) mode which benefits of one of the decay products of the core-hole which is created upon x-ray absorption. In the TEY mode all electrons emerging from the sample are detected, simply by measuring the current necessary to compensate for the lost charge. The probing depth is ~ 10 nm in the soft x-ray regime which is due to the limited escape depth of the electrons. Hence, the TEY gives information about the first few tens atomic layers near the surface while most of the bulk information is suppressed and is hence very well suited to study surface supported single atoms and epitaxial films of a few atomic layers.

The measurements presented in chapter 3 and 4 were carried out at the ID08 beamline of the European Synchrotron Radiation Facility (ESRF) in Grenoble. The available energy range of the synchrotron light is 400 - 1600 eV fitting the binding energy of the $2p$ levels of the $3d$ transition metals and of the $3p$ levels of the $4d$ transition metals. The undulators provide almost 100% circularly or linearly polarized light. Our interest is focused on the bulk ferromagnetic elements Fe, Co, and Ni as well as on the substrates Rh, Pd, and Pt, having a non-magnetic ground state in bulk, but known to be highly polarizable [40, 41, 42, 1, 31].

A sketch of the experimental setup is shown in Fig. 2.1. The variable magnetic field is collinear with the x-ray beam and the sample has a rotational degree of freedom about the y -axis. The magnetic field vector \mathbf{H} and the x-ray beam form an angle θ with the surface normal. Typically, the sample is rotated from normal incidence ($\theta = 0^\circ$) to grazing

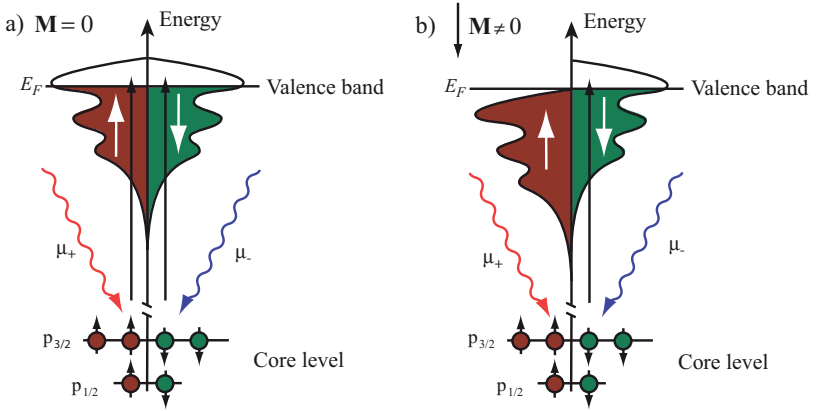


Figure 2.2: Schematic representation of L edge X-ray absorption of a) a nonmagnetic metal and b) a magnetic metal using left and right circularly polarized light. The asymmetry in the spin up and spin down states gives rise to a XMCD signal.

incidence ($\theta = 70^\circ$) in order to investigate out-of-plane versus in-plane magnetization and consequently to infer the magneto-crystalline anisotropy energy. The absorption coefficients μ_+ and μ_- for circularly polarized light are defined for parallel and antiparallel alignment of the photon helicity with respect to the applied field \mathbf{H} . Using linearly polarized light, the absorption coefficients h and v are measured with the electric field vector in the horizontal plane and in the vertical plane, respectively.

2.2 XAS with circularly polarized light

An example for x-ray absorption using circularly polarized light is shown in Fig. 2.2. Conservation of angular momentum requires the transfer of the photon angular momentum of the incident photon to the excited electron. If the photoelectron is excited from a spin-orbit split core level, the angular momentum of the photon can be transferred in part to the spin through the spin-orbit coupling. In ferromagnetic materials the valence shell is split due to the exchange interaction and the unequal spin-up and spin-down populations act as a filter for the excited photoelectrons. In the specific case of a strong ferromagnet shown in Fig. 2.2 b) only spin-down electrons can be excited, since the majority states are fully occupied.

In an x-ray absorption experiment the energy of the incident beam is scanned over the core levels and each of them gives rise to one peak. The L_3 peak corresponds to

	$ 2, 2\rangle$	$ 2, 1\rangle$	$ 2, 0\rangle$	$ 2, -1\rangle$	$ 2, -2\rangle$
$ \frac{1}{2}, +\frac{1}{2}\rangle$	$\frac{4}{15}$		$(\frac{2}{45})$		
$ \frac{1}{2}, -\frac{1}{2}\rangle$		$\frac{1}{15}$		$(\frac{1}{15})$	
$ \frac{3}{2}, +\frac{3}{2}\rangle$					
$ \frac{3}{2}, +\frac{1}{2}\rangle$	$\frac{2}{15}$		$(\frac{1}{45})$		
$ \frac{3}{2}, -\frac{1}{2}\rangle$		$\frac{2}{15}$		$(\frac{2}{15})$	
$ \frac{3}{2}, -\frac{3}{2}\rangle$			$\frac{1}{15}$		$(\frac{2}{5})$

Table 2.1: Transition probabilities from the spin-orbit split p states to the final d states having \downarrow spin for right (left) circular polarized light.

transitions from the $p_{3/2}$ states to the valence band and the L_2 peak to the $p_{1/2}$ to valence band transitions. The $p_{3/2}$ state has a lower binding energy and contains 4 of 6 p electrons, hence the L_3 edge occurs at lower photon energy and has a larger peak area compared to the L_2 edge (see Fig. 2.3). Theoretically, the ratio of the $L_3:L_2$ peak area is 2 : 1 if all (minority) final states were empty.

This can be verified by explicitly calculating the transition probabilities. As an example, the angular part given in equation (2.15) is evaluated for the transition from the $|\frac{1}{2}\rangle = \frac{\sqrt{2}}{\sqrt{3}}Y_{1,1}|\downarrow\rangle - \frac{1}{\sqrt{3}}Y_{1,0}|\uparrow\rangle$ initial state to the $Y_{2,2}|\downarrow\rangle$ final state for right circular polarized light. Since $\langle\downarrow|\uparrow\rangle = 0$, we need to calculate only

$$\left| \int \int \sin \vartheta d\vartheta d\phi Y_{2,2}^* \sqrt{\frac{4\pi}{3}} Y_{1,1} \frac{1}{\sqrt{3}} Y_{1,0} \right|^2 = \frac{4}{15}. \quad (2.17)$$

All transition probabilities to final states with \downarrow spin are summarized in Table 2.1. The total x-ray absorption ($\mu_+ + \mu_-$) is $\frac{8}{9}$ and $\frac{4}{9}$ at the L_3 and L_2 edge, respectively. The $L_3 : L_2$ ratio is as expected 2 : 1. The magnetic dichroism ($\mu_+ - \mu_-$) is $-\frac{2}{9}$ at the L_3 edge and $\frac{2}{9}$ at the L_2 edge, i.e., the ratio is $-1 : 1$. Note that $\sum_{L_2, L_3} (\mu_+ - \mu_-) = 0$ implying that the expectation value of the orbital moment vanishes in agreement with Hund's rules and the orbital momentum sum rule given in equation (2.18). Note that our elements of interest Fe, Co, Ni, Rh, Pd, and Pt have more than 5 d electrons.

In order to better predict the shape of a x-ray absorption spectrum more realistic final state wave functions need to be considered. For atomic systems, the dipole allowed transition probabilities in the fully relativistic model including valence-band spin-orbit coupling are given in Refs. 43 and 44. In solids the hybridization of atomic orbitals can be described using a tight-binding band structure approach, i.e., the valence band wave functions are linear combinations of the atomic orbitals [45, 46]. Fully relativistic tight-binding calculations of x-ray absorption and magnetic circular dichroism are presented

by Smith *et al.* in Ref. 44. Today, numerous codes exist to calculate XAS and XMCD line shapes in the relativistic local spin density approximation (LSDA) [47, 48, 49]. LSDA gives good results for the K edge of transition metals and $L_{2,3}$ edges of rare earth, but these calculations are not appropriate for the $L_{2,3}$ edges of $3d$ transition metals, because core-hole valence-electron interactions in the excited atom are neglected. These are quite large for the valence electron and the $2p$, $3s$, or $3p$ core-hole and give rise to multiplet effects [50, 51].

Thole *et al.* show in a localized ion model that the integral of the XMCD signal over both absorption edges is directly related to the local orbital moment L by [18]

$$L = -\frac{4}{3}h_d \frac{\int_{L_3+L_2}(\mu_+ - \mu_-)dE}{\int_{L_3+L_2}(\mu_+ + \mu_-)dE} = -\frac{4}{3}h_d \frac{q}{t}. \quad (2.18)$$

On an equal footing a relation of XAS and XMCD signal to the effective spin $S_{eff} = S+7D$ moment was derived [19]

$$S + 7D = -h_d \frac{6 \int_{L_3}(\mu_+ - \mu_-)dE - 4 \int_{L_3+L_2}(\mu_+ - \mu_-)dE}{\int_{L_3+L_2}(\mu_+ + \mu_-)dE} = -h_d \frac{6p - 4q}{t}. \quad (2.19)$$

Both equations are given in units of μ_B/atom , h_d is the number of holes in the $3d$ states and D is the magnetic spin dipole moment. The dipolar term arises from a non-spherical intra-atomic spin distribution, making the expectation value of D orientation dependent. When averaging XMCD intensities of samples magnetically saturated along all Cartesian axes, S and D can be determined separately [52]. In samples exhibiting magneto-crystalline anisotropy, L is orientation dependent and the anisotropy of L can be linked to the magneto-crystalline anisotropy energy [21, 20]. The measured expectation values L , S , and D are the projection of \mathbf{L} , \mathbf{S} , and \mathbf{D} momentum operators onto the quantization axis defined by the incident light direction. The notation L_θ and D_θ clarifies the crystal orientation during the measurement. Note that S is isotropic to second order and no index is needed.

The integrals p , q , and t of the x-ray absorption and magnetic circular dichroism spectra are labeled in Fig. 2.3 showing XAS and XMCD recorded at the Co $L_{2,3}$ edges for a 1.25 ML thick Co film on Rh(111). Figure 2.3 a) represents the raw absorption spectra of the clean Rh(111) substrate and the Co thin film normalized to the incident photon flux I_0 . The background signal of the clean substrate is recorded prior to Co deposition in order to isolate the absorption signal exclusively originating from the Co film. Figure 2.3 b) shows the XAS after background subtraction and a two-step function, taking into account non-resonant absorption of $2p \rightarrow 4s$ transitions. In Fig. 2.3 c) the non-resonant absorption has been subtracted in order to isolate the contribution of the $2p \rightarrow 3d$ transitions. The sum of both helicities and the corresponding integral are shown. In Fig. 2.3 d) the XMCD spectrum is displayed together with the corresponding integral.

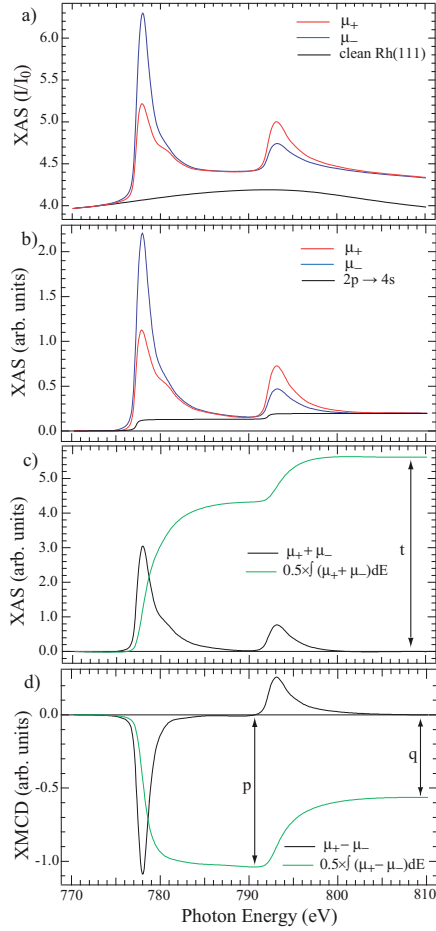


Figure 2.3: XAS and XMCD spectra recorded at the Co $L_{2,3}$ edges for a 1.25 ± 0.15 ML Co film on Rh(111) deposited at $T = 10$ K. The external field is $\mu_0 H = \pm 5$ T and $\theta = 70^\circ$. a) Absorption spectra normalized to the incident photon flux (I_0) for parallel ($\mu_+ = I_+/I_0$) and antiparallel ($\mu_- = I_-/I_0$) alignment of photon helicity with respect to the magnetic field. The black line is the background signal acquired on the clean Rh(111) surface. b) Resulting XAS after the subtraction of the background signal. The two-step function accounts for non-resonant absorption. c) Total resonant absorption signal, i.e., the sum of μ_+ and μ_- without the $2p \rightarrow 4s$ transitions as well as the corresponding integral. d) XMCD spectrum with the corresponding integral calculated from spectra shown in b).

The sum rules (equations (2.18) and (2.19)) allow to compute the magnetic moments with the input of h_d , e.g. from theoretical investigations. A value independent of h_d can be obtained by taking the ratio

$$r = \frac{L}{S + 7D} = \frac{L}{S_{eff}}. \quad (2.20)$$

Further, it is a good number even away from saturation and r can be used as an estimate of L . Provided $7D$ is small compared with S and that S_{eff} varies slowly with the coordination number of the atom a numerical value of L may be obtained by identifying S_{eff} for clusters, larger islands, or monolayer films, which are easier to saturate.

2.3 XAS with linearly polarized light

Linear dichroism describes the angle dependent effects when either the direction of the electric field vector \mathbf{E} relative to the sample is changed and the applied field vector \mathbf{H} is unchanged (first kind), or the direction of \mathbf{H} is rotated while the x-ray polarization is fixed (second kind). For linear x-rays the electric field vector acts like a search light for the direction of the maximum and minimum number of empty valence states. Hence, the transition intensity is directly proportional to the number of empty states in the direction of \mathbf{E} . The transition probabilities of the matrix element $\langle f | \mathcal{E} \mathbf{r} | i \rangle$ are given in Table 2.2. In nonmagnetic samples the anisotropy arises only from the anisotropic charge and - complementary to this - empty state distribution caused by bonding, i.e., linear dichroism of first kind is observed. For magnetic samples an additional anisotropy may exist relative to the magnetization direction. If the origin of dichroism is due to nonuniform spatial bonding we speak of x-ray *natural* linear dichroism (XNLD) and if of magnetic origin we speak of x-ray *magnetic* linear dichroism (XMLD). The XMLD signal is proportional to M^2 , which means that linear dichroism measurements are suited to detect the magnetic moment per atom in antiferromagnetic samples [53, 46].

XNLD and XMLD can be separated in temperature dependent studies or by comparing linear magnetic dichroism measurements of first and second kind. In ferromagnetic samples the atomic spins are aligned by the exchange interaction and a nonspherical distortion of the atomic charge develops via the spin-orbit interaction. The effect of the spin-orbit coupling on the charge density can be visualized by plotting the charge densities of the spin-orbit split p and d manifolds (see Table A.3). The exchange interaction lifts the degeneracy of the $|j, m_j\rangle$ substates which leads to an unequal spectral contribution. This can be directly observed in the measured XMLD line shape [54]. The XMLD intensity is significantly smaller than the corresponding XMCD intensity [54, 15, 13]. Despite the small XMLD signal and the demanding experimental implementation, the linear dichroism of second kind - i.e., fixing the x-ray polarization vector along the easy axis and then rotating the magnetization from the easy to the hard axis with a sufficiently strong

	$ 2, 2\rangle$	$ 2, 1\rangle$	$ 2, 0\rangle$	$ 2, -1\rangle$	$ 2, -2\rangle$
$ \frac{1}{2}, +\frac{1}{2}\rangle$		$(\frac{2}{15})$	$\frac{4}{45}$		
$ \frac{1}{2}, -\frac{1}{2}\rangle$			$(\frac{4}{45})$	$\frac{2}{15}$	
$ \frac{3}{2}, +\frac{3}{2}\rangle$		$\frac{1}{5}$			
$ \frac{3}{2}, +\frac{1}{2}\rangle$		$(\frac{1}{15})$	$\frac{8}{45}$		
$ \frac{3}{2}, -\frac{1}{2}\rangle$			$(\frac{8}{45})$	$\frac{1}{15}$	
$ \frac{3}{2}, -\frac{3}{2}\rangle$				$(\frac{1}{5})$	

Table 2.2: Transition probabilities from the spin-orbit split p states to the final d states with spin \uparrow (\downarrow) for linearly polarized light.

magnetic field - allows to infer directly the magneto-crystalline anisotropy [55, 56].

Chapter 3

Magnetism of Single Atoms

The electronic ground state of a free atom is given by Hund's rules which summarize as follows:

1. The ground state corresponds to a minimum of the Coulomb energy which is achieved by keeping electrons spatially as far apart as possible. If the number of electrons is smaller than $2l + 1$, where l is the orbital angular momentum, all electrons can have parallel spins without multiple occupation of any one-electron level in the shell, corresponding to a maximum S value. We assign each electron to levels with different values of m_l .
2. Electrons that orbit in the same direction minimize their Coulomb repulsion and have parallel angular momenta, corresponding to maximum total orbital moment L .
3. The lowest spin-orbit energy corresponds to collinear \mathbf{S} and \mathbf{L} . When the shell is more than half full \mathbf{S} and \mathbf{L} point in the same direction; the highest value of J is lowest in energy. For atoms with less than half-filled shells, \mathbf{S} and \mathbf{L} are antiparallel; now the lowest value of J has the lowest energy.

For a more than half full d shell we have¹:

	$m_l = -2,$	$-1,$	$0,$	$1,$	2	S	L	$7D$	$\frac{L}{S}$	$\frac{L}{S+7D}$
d^6	$\uparrow\downarrow$	\downarrow	\downarrow	\downarrow	\downarrow	4	2	-2	1/2	1
d^7	$\uparrow\downarrow$	$\downarrow\uparrow$	\downarrow	\downarrow	\downarrow	3	3	-1	1	3/2
d^8	$\uparrow\downarrow$	$\downarrow\uparrow$	$\downarrow\uparrow$	\downarrow	\downarrow	2	3	1	3/2	1
d^9	$\uparrow\downarrow$	$\downarrow\uparrow$	$\downarrow\uparrow$	$\downarrow\uparrow$	\downarrow	1	2	2	2	2/3

¹Note that we include for the total orbital ($L = |\sum g_L m_l|$) and spin moment ($S = |\sum g_S m_s|$) the g-factor which is $g_L = 1$ for the orbital moment and $g_S = 2$ for the spin moment. $m_s = -1/2$ for \downarrow and $m_s = 1/2$ for \uparrow .

The ground state of a free Fe atom is d^6 and the one of a free Co atom d^7 . By forming dimers, trimers or clusters of a few equal atoms the atomic orbitals hybridize and form narrow energy bands. This leads to a different electron occupation of each shell and a reduced spin moment of the $3d$ shell. The magnetic moments of the ferromagnetic elements Fe, Co, and Ni were determined as a function of cluster size with a Stern-Gerlach apparatus [57, 58, 59]. The clusters, having a size ranging from 20 up to 700 atoms, show atomlike magnetic moments for clusters with fewer than 30 atoms and approach the bulk limit for clusters of a few hundred atoms. Finite magnetic moments were also expected in clusters of elements which are not ferromagnetic in the bulk because of the reduced dimensionality and the consequently very narrow d -band width [60]. Indeed, a magnetic moment was observed in rhodium clusters composed of 12-32 atoms, whereas ruthenium and palladium clusters are nonmagnetic [61, 62].

Studying free atoms and clusters in the gas phase is interesting from a fundamental point of view, but for technological applications these must be deposited on surfaces or in matrices. The extent to which the d orbitals of a transition metal mix with the valence electrons of a nonmagnetic supporting surface determines the electronic and magnetic properties of the adatom. On metallic surfaces the adatoms strongly interact with the valence electrons of the substrate. For example Fe, Co, and Ni on K have a predominant d^7 , d^8 , and d^9 character, respectively, evidencing a charge transfer of +1 electron to the d states [63]. The alkali metal substrate has a simple sp electronic structure which leaves the d states of the magnetic adatom almost unperturbed and reveals atomic like ground states and vanishing magnetic anisotropy. This is completely different on transition metal substrates, whose d electrons strongly hybridize with the ones of the adatom. As a consequence a sizable magnetic moment is induced in the neighboring substrate atoms which in turn contributes to the magnetic anisotropy via the large spin-orbit constant [1, 5, 31]. Motivated by the experimental finding of a large MAE for single Co atoms on Pt(111) [1] and on Pd(111) [64] and by the theoretical prediction of similarly large MAE for Fe atoms on Pt(111) [5, 3], we prepared samples with single Fe atoms on Rh(111), Pd(111), and Pt(111) and single Co atoms on Rh(111) in order to investigate the influence of the supporting transition metal. XAS and XMCD measurements are presented in section 3.1.

Hybridization of the d orbitals of Fe and Co when deposited on a $4d$ or $5d$ metal substrate reduces the orbital and spin moment of the adatom compared with the values of the free atom. To avoid this and restore atomic L and S values, we also deposited Fe and Co atoms on two insulating substrates, namely $\text{Al}_2\text{O}_3/\text{Ni}_3\text{Al}(111)$ and $\text{Cu}_2\text{N}/\text{Cu}(001)$. The band gap is 7-8 eV for the alumina film [65] and 4 eV for the Cu_2N layer [66] which should allow to decouple the magnetic atoms effectively from the conduction electrons of the underlying metal. In addition, symmetry breaking at the surface and directional bonding in the surface lead to a large magnetic anisotropy on Cu_2N of $K = 6.2$ meV/Fe atom and $K = 6.2$ meV/Co atom which was obtained by inelastic electron tunneling

spectroscopy (IETS) measurements [9, 32, 17]. The found MAE values are comparable to molecular magnetic clusters [67]. IETS yields atomic spin moments for Fe and Co, but is not able to infer the orbital magnetic moment which is supposed to play a major role in the anisotropic behavior [33]. We report on XMCD measurements of isolated Fe and Co atoms on $\text{Al}_2\text{O}_3/\text{Ni}_3\text{Al}(111)$ in section 3.2 and of isolated Fe and Co atoms on $\text{Cu}_2\text{N}/\text{Cu}(001)$ in section 3.3.

3.1 Fe and Co single atoms on Rh(111), Pd(111), and Pt(111)

Single atoms on metal surfaces are experimentally obtained when depositing minute amounts of matter by atomic beam epitaxy at low temperature where surface diffusion is inhibited. The impinging atoms irreversibly stick to the surface and stay at their landing site implying very efficient dissipation of their binding energy [68]. Such a statistic growth leads for low coverage to fractions of monomers, dimers, trimers and eventually larger clusters. The following table summarizes the expected abundances and the mean size $\langle s \rangle$ for some low coverages encountered in this section ²:

coverage	monomers	dimers	trimers	$\langle s \rangle$
0.005 ML	97%	3%	-	1.02
0.01 ML	93%	7%	-	1.04
0.015 ML	90%	9%	1%	1.05
0.02 ML	87%	11%	2%	1.07
0.0125 ML	84%	14%	2%	1.09
0.03 ML	81%	15%	3%	1.11

The Rh(111), Pd(111), and Pt(111) substrates were prepared by Ar^+ -ion sputtering (1.3 keV, at $T = 300$ K to remove magnetic material and for 20 minutes at $T = 800$ K once the substrate was clean), followed by annealing at $T = 800$ K at an oxygen partial pressure of $P_{\text{O}_2} = 6 \times 10^{-8}$ mbar for 10 minutes to remove carbon impurities, and final annealing to 1000 – 1100 K. Substrate cleanliness was checked by Auger electron spectroscopy and XAS. Fe and Co were deposited from high-purity rods (99.995%) at $T = 9$ K using a commercial electron beam evaporator. The flux was 5×10^{-4} ML/s and 10^{-3} ML/s for Fe and Co, respectively.

²We use the KMC simulation program developed by M. El Ouali and extended by P. Buluschek [69, 70]. The code treats a hexagonal close packed surface and allows only the occupation of fcc sites. We assume that the dimer is stable ($i = 1$) and neglect reevaporation and edge- or corner-diffusion. We used the adatom migration barrier $E_m = 200$ meV and the attempt frequency $\nu_0 = 10^{13}\text{s}^{-1}$ representative for metal on metal systems [71]. The deposition rate was 10^{-3} ML/s and $T = 10$ K.

The magnetic properties were investigated *in situ* by XAS and XMCD for normal incidence ($\theta = 0^\circ$) and grazing incidence ($\theta = 70^\circ$) at $\mu_0 H = 5$ T and $T = 8$ K. In Fig. 3.1 XAS and resulting XMCD spectra for Fe on Rh(111), Pd(111), and Pt(111) taken at the Fe $L_{2,3}$ edges are shown. The adatom XAS are relative weak absorption features compared with the Rh, Pd, or Pt background due to the extremely low coverage. The small hump of the L_2 edge is hardly visible. The resulting dichroic signal is shown next to the XAS. For all studied systems the L_3 XMCD peak is larger for 0° suggesting an out-of-plane easy axis. The inset in Fig. 3.1 f) shows an example of a magnetization curve for Fe/Pt(111). Those for Fe on Rh(111) and Pd(111) are similar. At both angles we observe an almost straight line with nearly identical slope suggesting a very small anisotropy energy. Obviously, saturation is not reached and we cannot apply the sum rules to infer the orbital and spin magnetic moment independently. However, we calculated L/S_{eff} and report the obtained values along the easy axis in table 3.1.

To complete the series of individual Fe and Co atoms on Rh(111), Pd(111), and Pt(111) we measured 0.02 ML Co/Rh(111). XAS, XMCD and magnetization curves are shown in Fig. 3.2. The larger L_3 XMCD peak for 70° suggests an in-plane easy axis. This is confirmed by the steeper slope of the magnetization curve at $\theta = 70^\circ$ compared to 0° . Note that the in-plane easy axis for Co/Rh(111) is characteristic for the first monolayer as we will discuss later (see for example Fig. 5.9 in chapter 5 and Figs. 4.12 and 4.10 in 4). Again, saturation cannot be reached and we calculated only L/S_{eff} which is reported in table 3.1.

We estimate the MAE from the magnetization loops shown in Fig. 3.2 c). In the anisotropic paramagnetic case, the energy of a particle of size s in an external magnetic field is given by the classical Boltzmann statistics. The energy function $E(\vartheta_0, \vartheta, \varphi)$ is composed of the Zeeman term $-sm\mu_0 H \cos \vartheta$ and, assuming uniaxial anisotropy, the MAE term $-sK(\sin \vartheta_0 \sin \vartheta \cos \varphi + \cos \vartheta_0 \cos \vartheta)^2$. \mathbf{H} is taken as the z axis, ϑ, φ are the polar and azimuthal coordinates of the magnetic moment \mathbf{m} , and ϑ_0 defines the easy magnetization direction. The magnetization then reads [72]

$$M = M_{SAT} \frac{\int_0^{2\pi} d\varphi \int_0^\pi d\vartheta \sin \vartheta \cos \varphi e^{-\frac{E(\vartheta_0, \vartheta, \varphi)}{k_B T}}}{\int_0^{2\pi} d\varphi \int_0^\pi d\vartheta \sin \vartheta e^{-\frac{E(\vartheta_0, \vartheta, \varphi)}{k_B T}}}. \quad (3.1)$$

From experiment we know the temperature $T = 8 \pm 1$ K and the external field \mathbf{H} at each measuring point. Assuming an average cluster size of $s = 1.07$ for statistical growth of 0.02 ML, the magnetic moment m and anisotropy energy K per Fe atom remain as parameters to fit both branches. The best fit is obtained for $K = 0.6 \pm 0.1$ meV and $m = 5 \pm 1 \mu_B$. The error is mainly due to the uncertainty of the sample temperature. The total magnetic moment $m = L + S + m_{Rh}$ includes the magnetic moment induced on the Rh sites per Co atom. To disentangle the contributions from the adatom and the substrate we take S and S_{eff} obtained for the Co monolayer film and make use of the

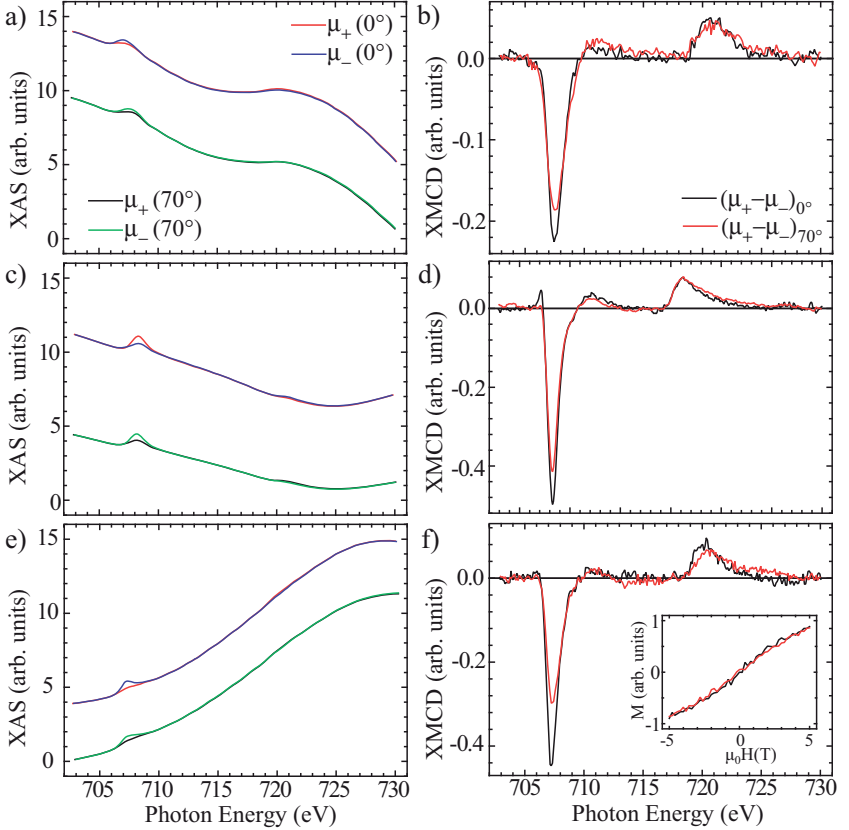


Figure 3.1: XAS and XMCD spectra of Fe on Rh(111), Pd(111), and Pt(111) measured at the Fe $L_{2,3}$ edges at $T = 8$ K and $\mu_0 H = 5$ T. The spectra at 70° have been normalized to the $\int_{L_3} (\mu_+ + \mu_-)$ intensity at 0° to eliminate the dependence of the electron yield on the sample orientation. a) and b) 0.01 ML Fe/Rh(111), c) and d) 0.02 ML Fe/Pd(111), e) and f) 0.01 ML Fe/Pt(111), inset: magnetization curves at $\theta = 0^\circ$ (black line) and 70° (red line) measured by taking the peak of the L_3 XMCD intensity at 707.7 eV divided by the pre-edge intensity at 705.0 eV as a function of the applied magnetic field.

fact that S is largely independent of coordination (see section 4.2.1 and table 3.1). We obtain an orbital moment of $L = 1.2 \mu_B$ for the Co atom and an induced moment of $m_{Rh} = 1.8 \pm 1 \mu_B$.

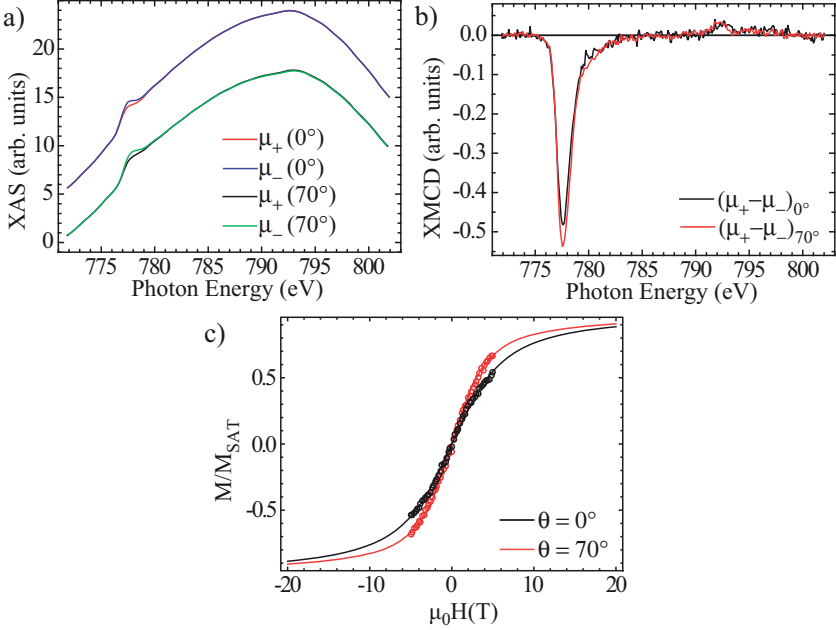


Figure 3.2: 0.02 ML Co/Rh(111) measured at $T = 8$ K. a) XAS taken at the Co $L_{2,3}$ edges at $\mu_0 H = 5$ T. The spectra at 70° have been normalized to the $\int_{L_3}(\mu_+ + \mu_-)$ intensity at 0° to eliminate the dependence of the electron yield on the sample orientation. b) resulting XMCD spectra c) Magnetization curves at $\theta = 0^\circ$ (black open circles) and 70° (red open circles) measured by taking the peak of the L_3 XMCD intensity at 777.0 eV divided by the pre-edge intensity at 773.5 eV as a function of the applied magnetic field. The solid lines are the best fit assuming anisotropic paramagnetic impurities of mean size $s = 1.07$ atoms with $K = 0.6$ meV and $m = 5 \mu_B$.

When comparing Fe on the three different substrates we find a common out-of-plane easy axis and a similar L/S_{eff} ratio. Further, we find that the Fe MAE is significantly smaller than the 0.6 meV inferred for Co/Rh(111). Also for Co on the three substrates we find a similar L/S_{eff} ratio. It is remarkable that L/S_{eff} is more than a factor of three larger for Co compared with Fe. For a free Co atom $L/S = 1$ and a free Fe atom $L/S = 1/2$. Similarly, for bulk hcp Co $L/S_{eff} = 0.09$ is found and for bulk bcc Fe $L/S_{eff} = 0.04$ [15]. Fe and Co overlayers on Rh(111) and Pt(111) are discussed in chapter 4.

	$\Theta(\text{ML})$	L	S_{eff}	L/S_{eff}	m_{sub}	MAE	easy axis
Fe/Rh(111)	0.01			0.15 ± 0.05			\uparrow
Fe/Pd(111)	0.02			0.12 ± 0.05			\uparrow
Fe/Pt(111)	0.01			0.18 ± 0.05			\uparrow
Co/Rh(111)	0.02	(1.2 ± 0.1)	(2.1 ± 0.1)	0.57 ± 0.04	1.8 ± 1	0.6 ± 0.1	\rightarrow
Co/Pd(111)	0.02	1.3 ± 0.1	1.9 ± 0.1	0.70 ± 0.06		~ 3	\uparrow
Co/Pt(111)	0.01	1.1 ± 0.1	1.8 ± 0.1	0.61 ± 0.05	1.8 ± 1	9.3 ± 1.6	\uparrow

Table 3.1: Orbital and spin moments (in units of μ_B/atom) estimated from XAS data acquired along the easy axis (\uparrow stands for out-of-plane and \rightarrow for in-plane) with $\mu_0 H = 5$ T. m_{sub} (in units of μ_B/atom) is the induced magnetic moment per adatom. The MAE is given in meV/atom. For Co/Rh(111) the S_{eff} is taken from table 4.3 and L calculated with this effective spin value. The reported values for Co/Pd(111) are taken from Ref. 64 and those for Co/Pt(111) from Ref. 1.

According to P. Gambardella *et al.* the strength of the MAE in case of Co/Pt(111) can be explained by the strong spin-orbit coupling of the Pt $5d$ electrons resulting in an additional MAE of the induced magnetization [1]. Theoretical investigations on the contrary attribute only a minor role to the MAE contribution of the induced moment and in general underestimate the experimentally found MAE of 9.3 meV. S. Bornemann *et al.* found 4.8 meV for the Co single atom and a few neV for the anisotropy coming from the Pt substrate [3]. C. Etz *et al.* assign 4.4 meV to the Co atom and 0.6 meV to the induced Pt moments [5]. In a recent joint experimental and theoretical study of Co/Pt(111) a MAE of 10.3 meV is inferred from inelastic tunneling spectroscopy performed with a low-temperature STM whereas theory predicts a magnetic anisotropy of only 3.1 meV and 3.8 meV for Co atoms in fcc and hcp positions, respectively [6]. The importance of the substrate with respect to the magnetic anisotropy becomes evident when comparing the MAE for Co on the three different substrates in table 3.1. We find an increasing MAE from Rh over Pd to Pt which can be directly related to the increasing spin-orbit constants for the $4d$ and $5d$ transition metal substrates [46].

For Fe the MAE is small on the three substrates and no trend could be established. Surprisingly, theory predicts very large MAE values for Fe single atoms on Pt(111) of 8.8 meV [3] or 5.3 meV [5], which are in disagreement with our experimental results. Recently, T. Balashov *et al.* showed for the first time that there is a significant difference in the anisotropy for Fe atoms in fcc (3.2 meV) and hcp (0.4 meV) positions on the Pt(111) substrate [6]. The authors suggest to probe with STM Fe atoms mainly in the fcc positions due to the experimentally large anisotropy of 6.5 meV. Equally, we can argue

to probe with XMCD predominantly Fe in hcp positions.

3.2 Fe and Co single atoms on $\text{Al}_2\text{O}_3/\text{Ni}_3\text{Al}(111)$

Oxidation of $\text{Ni}_3\text{Al}(111)$ may lead to different types of oxides: aluminum oxide or *alumina* with the chemical formula Al_2O_3 , nickel oxide (NiO), and NiAl_2O_4 . The formation of aluminum oxide is thermodynamically favored, but due to the low aluminum content of the sample the chemical composition of the surface oxide is determined by the rate of segregation of aluminum to the surface compared with the reaction rate with the dosed oxygen.

Aluminium oxide is an electrical insulator and it is used for its hardness and strength in numerous fields of industry, e.g. cutting tools, polishing, ceramics, health and medical applications. Metallic aluminium is very reactive with atmospheric oxygen, and a thin passivation layer of amorphous alumina quickly forms on any exposed aluminium surface. This layer protects the metal from further oxidation. The thickness and properties of this oxide layer can be enhanced using a process called anodising which is an electrolytic passivation process used to increase the thickness of the natural oxide layer on the surface.

Alumina is known to exist in several crystalline phases or forms, the only thermodynamic stable is the corundum or α -phase which has the rhombohedral hcp crystal structure [73]. It is transparent and colorless and known in its single crystalline form as *sapphire*. Among many other crystalline phases κ -alumina (orthorhombic) just as α -alumina are important for its hardness and thermal stability [74, 75]. The metastable phases γ (cubic spinel) and θ (monoclinic) are found in applications as catalyst supports due to their low surface energy [76].

3.2.1 Oxygen adsorption and oxide formation on $\text{Ni}_3\text{Al}(111)$

Oxidation of $\text{Ni}_3\text{Al}(111)$ in a controlled environment, i.e., low oxygen partial pressure and precise temperature monitoring, leads to a well-ordered surface oxide of 5 Å thickness [77, 78]. The $\text{Ni}_3\text{Al}(111)$ single crystal was prepared by Ar^+ -ion sputtering at room temperature for 30 min ($P = 5 \times 10^{-6}$ mbar, 1 keV) and annealing for 10 min at 960 ± 30 K, reading the temperature with a pyrometer. The alumina thin film is then grown by exposing the clean and ordered $\text{Ni}_3\text{Al}(111)$ surface one hour to oxygen gas ($P_{\text{O}_2} = 1 \times 10^{-7}$ mbar) while keeping the sample at 960 ± 30 K and keeping it for one more hour at this temperature without further exposure to O_2 .

In Fig. 3.3 our LEED pattern and a comparative LEED pattern from Ref. 78 are shown. We find the characteristic 2×2 spots of the chemically ordered alloy substrate and satellites typical for the oxide structure. C. Becker *et al.* interpreted the LEED pattern as two domains of γ' - Al_2O_3 which is supported by high-resolution electron-energy

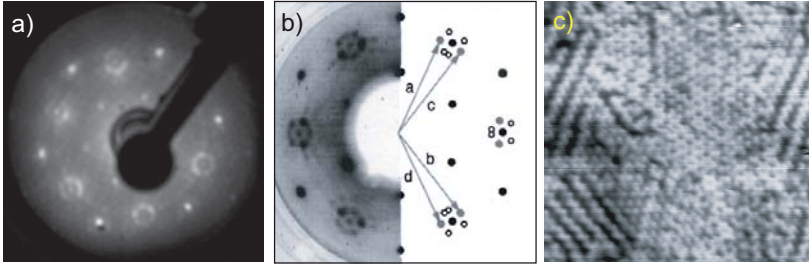


Figure 3.3: Al₂O₃ surface oxide on Ni₃Al(111) prepared at 960 ± 30 K. a) LEED pattern obtained at $E = 62$ eV, b) LEED pattern taken from Ref. 78, c) STM image ($430 \text{ \AA} \times 430 \text{ \AA}$, $V_t = 3.0$ V, $I_t = 200$ pA)

loss spectroscopy. The unit vectors of the two domains, rotated by 36.6° (a,b) and 23.4° (c,d) with respect to the substrate, are shown in Fig. 3.3 b). The STM image of this γ -Al₂O₃-film reveals in addition to the often described network structure (see center of the STM image), different rotational domains of a *stripe* phase [79]. The stipe domains are rotated by $\sim 120^\circ$.

In order to produce a closed, highly ordered, and grain boundary free alumina film post-annealing at 1050 K seems essential [65, 78, 80]. Unfortunately, the resistive heater of the preparation chamber at the ESRF did not allow heating to $T = 1050$ K. M. Schmid *et al.* claim that, besides accurately following the sample preparation protocol, the exact stoichiometry of the crystal may be the origin of different coexisting phases [79]. We exclude the crystal itself from being the reason, because we were able to produce a highly ordered alumina film with the desired $(\sqrt{67} \times \sqrt{67}) R 47.8^\circ$ in our own preparation chamber with the very same Ni₃Al(111) single crystal [81].

3.2.2 Magnetic properties of Al₂O₃ on Ni₃Al(111)

Before depositing Fe or Co we investigated the magnetic properties of the Al₂O₃/Ni₃Al(111) sample. Earlier measurements report of weak itinerant ferromagnetism of Ni₃Al with a Curie temperature of $T_C = 40$ K and a very small magnetic moment of $0.23 \mu_B/\text{cell}$, where one cell equals one Ni₃Al unit [82, 83]. Assuming that only the Ni atoms in the cell carry a magnetic moment, $0.076 \mu_B/\text{Ni atom}$ is obtained.

We measured XAS with circularly polarized light at normal incidence as a function of temperature. In Fig. 3.4 a) the absorption spectra of the saturated sample below T_C are shown. Using the sum rules given in equation (2.18) and (2.19) and the number of *d*-holes of bulk Ni $h_d = 1.66$ we obtain an orbital moment of $0.047 \mu_B/\text{Ni atom}$ and a spin moment of $0.357 \mu_B/\text{Ni atom}$ when neglecting the dipolar term $7D$ [84]. This is

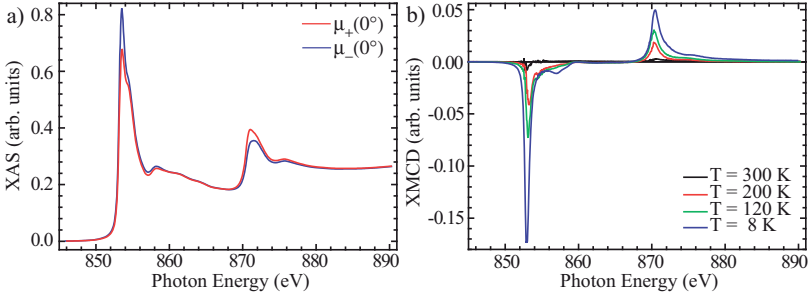


Figure 3.4: Al_2O_3 surface oxide on $\text{Ni}_3\text{Al}(111)$ prepared at 960 ± 30 K. a) XAS with circularly polarized light at the Ni $L_{2,3}$ edges at $\mu_0 H = 2$ T and $T = 8$ K. b) XMCD signal as a function of temperature at $\mu_0 H = 2$ T.

smaller than $0.62\mu_B/\text{atom}$, the magnetic moment of bulk Ni [46], but substantially larger than the magnetic moment of Ni_3Al inferred by magnetometry and can be explained by a compositional change in the substrate due to the formation of the Al_2O_3 layer. The topmost layer of stoichiometric $\text{Ni}_3\text{Al}(111)$ contains only 25% Al which is not sufficient to form a doublelayer of alumina. Part of the Al must therefore migrate to the surface from deeper layers resulting in several Ni-rich layers. This model was confirmed by x-ray photoelectron spectroscopy finding up to 100% Ni in the outermost layer at the interface with the oxide [77]. We recall, that x-ray absorption spectra taken in the total electron yield are sensitive to the near surface layers. An increasing magnetic moment with increasing Ni content was found for bulk samples as well. For an alloy composition of $\text{Ni}_{0.76}\text{Al}_{0.24}$ a magnetic moment almost twice as large as for $\text{Ni}_{0.75}\text{Al}_{0.25}$ was found [82, 83]. Note that the Curie temperature increases at the same time. We did not investigate the magnetic phase transition in more detail.

3.2.3 Isolated Fe and Co atoms

We deposited minute amounts of Fe or Co at the lowest available temperature, $T = 8$ K, with a commercial e-beam evaporator from high purity Fe and Co rods. The Al_2O_3 film is terminated by oxygen atoms, consequently the Fe and Co atoms land on top of O atoms [79]. XAS and XMCD measured at the Fe $L_{2,3}$ edges and Co $L_{2,3}$ edges are shown in Fig. 3.5. For Fe and Co we find a pronounced multiplet structure, which is typical for free atoms and single atoms in ionic and covalent compounds [85]. The XAS and XMCD line shape depend on the sample orientation with respect to the beam which is mainly a linear dichroism effect due to the anisotropic spatial distribution of the d -electrons as we will outline in the following.

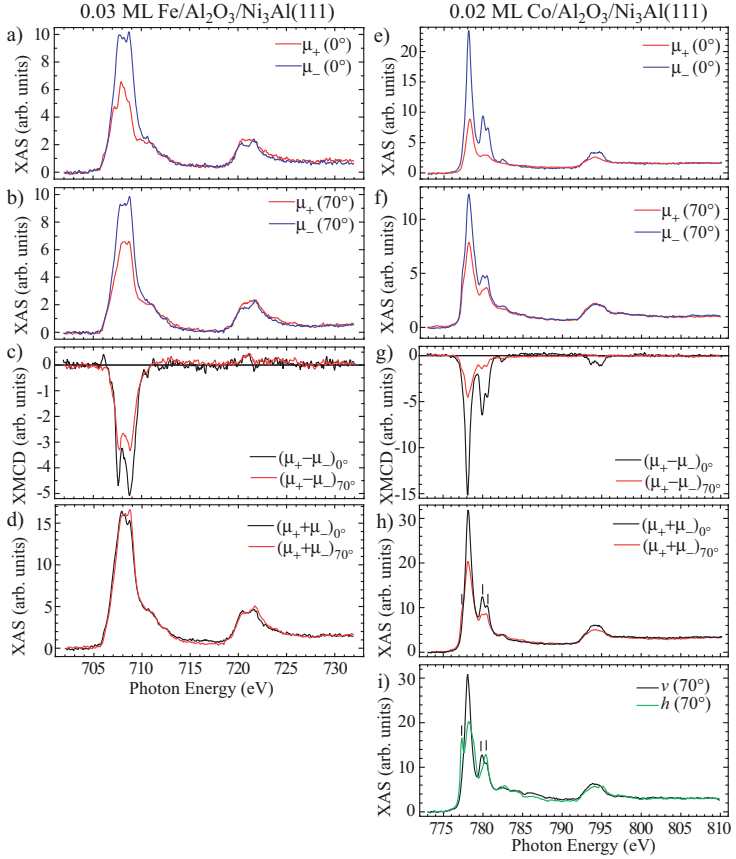


Figure 3.5: a) and b) XAS taken at Fe $L_{2,3}$ edges at $T = 8$ K and $\mu_0 H = 5$ T with right and left circularly polarized light at $\theta = 0^\circ$ and $\theta = 70^\circ$, respectively. The spectra at $\theta = 70^\circ$ have been normalized to the $\int(\mu_+ + \mu_-)L_3$ intensity at $\theta = 0^\circ$ to eliminate the dependence of the electron yield on the sample orientation. The background was subtracted. c) Resulting XMCD spectra. d) Sum of XAS with positive and negative helicity. e) and f) XAS taken at Co $L_{2,3}$ edges at $T = 8$ K and $\mu_0 H = 5$ T with right and left circularly polarized light at $\theta = 0^\circ$ and $\theta = 70^\circ$, respectively. The spectra at $\theta = 70^\circ$ have been normalized to the $\int(\mu_+ + \mu_-)L_3$ intensity at 0° . The background was subtracted. g) Resulting XMCD spectra. h) Sum of XAS with positive and negative helicity. i) XAS with linearly polarized light. v and h designate vertical and horizontal alignment of the electric field vector according to Fig. 2.1.

X-ray absorption spectra with linearly polarized light recorded for 0.02 ML Co on $\text{Al}_2\text{O}_3/\text{Ni}_3\text{Al}(111)$ are shown in Fig. 3.5 i). The electric field vector E_v is in the sample plane independent of the angle θ . In case of isotropic in-plane chemical bonding or electric charge distribution the vertical XAS is expected to have the same shape as the sum of the two circular XAS acquired at $\theta = 0^\circ$ which is a simple consequence of free basis choice [80]. We find a very similar form for v and $(\mu_+ + \mu_-)_{0^\circ}$ (see Fig. 3.5 h) and i)) suggesting the absence of in-plane anisotropic chemical bonding or charge distribution. This is reasonable when considering the finite size of the x-ray beam averaging over different domains and rotations of the Al_2O_3 film. E_h probes the out-of-plane d -orbitals and if in-plane and out-of-plane chemical bonding are not equivalent a difference in h and v linear XAS must be observed. In the h absorption spectrum shown in Fig. 3.5 h), we remark a peak at 777.0 eV which is absent in the v spectrum and a shift of the satellite peak's maximum found at 780.0 eV in the v spectrum to 780.5 eV. In the $(\mu_+ + \mu_-)_{70^\circ}$ spectrum in h), these features appear as a shoulder at 777.0 eV and a change in relative intensity of the peaks at 780.0 eV and 780.5 eV. Note that the linear dichroism is much weaker in case of Fe than in the one of Co.

To discuss the magnetic properties, we evaluate the ratio $r = L/(S + 7D)$ and the branching ratio defined as

$$BR = \frac{I(L_3)}{I(L_2) + I(L_3)} = \frac{\int_{L_3} (\mu_+ + \mu_-) dE}{\int_{L_2+L_3} (\mu_+ + \mu_-) dE}, \quad (3.2)$$

both being good numbers especially for not fully saturated samples. Unfortunately, we could not establish if saturation is reached at 5 T or not, because the spectral shape changes rapidly over time (see section 3.2.4 for more information) and therefore, we did not acquire magnetization curves.

First, we focus on 0.03 ML Fe/ $\text{Al}_2\text{O}_3/\text{Ni}_3\text{Al}(111)$ shown on the left hand side in Fig. 3.5. The XAS and XMCD spectra are substantially different from the line shape of bulk iron oxides [86, 87, 88, 89]. In bulk oxides the environment of the Fe ions is of octahedral (O_h) or tetrahedral (T_d) symmetry, which is further reduced for the surface supported single atom. The reduced symmetry of the Fe atom on the alumina film gives rise to a large r , i.e., a large orbital moment. At $\theta = 0^\circ$ we obtain $r = 0.53 \pm 0.09$, and $r = 0.31 \pm 0.07$ at $\theta = 70^\circ$. For comparison, bulk iron oxide has $r = 0.05$ [89] and Fe spins in a supramolecular network ($\text{O}_2\text{-Fe}(\text{TPA})_4/\text{Cu}(001)$), where the Fe has C_{4v} symmetry, have $r = 0.21$ at 0° and $r = 0.28$ at 70° [11].

From the integrated total XAS we obtain the branching ratio at 0° and 70° , which is 0.82 ± 0.03 at both angles, suggesting a high-spin ground state for Fe [90]. Further, the large values of BR and r , suggest that the crystal field splitting $10Dq$ has to be comparable or smaller with respect to the spin-orbit coupling constant ξ_{3d} of the $3d$ -orbitals. ξ_{3d} is between 50 meV and 100 meV for Fe and Co [46]. The larger XMCD signal at the L_3

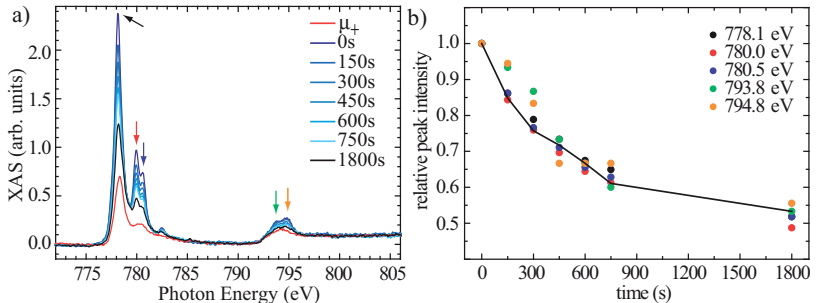


Figure 3.6: 0.02 ML Co/Al₂O₃/Ni₃Al(111) a) XAS taken at Co $L_{2,3}$ edges at $T = 8$ K and $\mu_0 H = 5$ T with positive (red line) and negative (blue lines) x-ray helicity for $\theta = 0^\circ$ as a function of time. b) Evolution of the μ_- spectra’s principal peaks marked with arrows in a). The line represents the time dependence of the integrated μ_- absorption spectrum normalized to the $t = 0$ s integral. The non-resonant transitions were subtracted.

edge for $\theta = 0^\circ$ indicates an easy magnetization axis out-of-plane, which will be confirmed for 0.14 ML Fe coverage in section 3.2.5.

The Co absorption and dichroism spectra are shown on the right hand side in Fig. 3.5. Again, the XAS and XMCD spectra of Co on alumina do not resemble very much the line shape of CoO [27, 91]. At 0° the L_3 dichroism signal has the same sign as the L_2 dichroism signal which leads to a $L/(S + 7D)$ ratio greater than $r = 2/3$ obtained for absent L_2 . We calculate $r = 0.91 \pm 0.06$ for 0° and $r = 0.68 \pm 0.05$ for 70° . The branching ratio is 0.89 ± 0.03 at 0° and 0.86 ± 0.03 at 70° . As already discussed in case of Fe, we can assume a high spin ground state and a crystal field parameter similar to ξ_{3d} . Also for Co, we infer an out-of-plane easy axis by comparing the XMCD signal at 0° and 70° .

3.2.4 Beam induced change of the XAS white line

As earlier mentioned, we observe a quickly changing spectral shape of XAS for single Fe and Co atoms. As an example we show in Fig. 3.6 the XAS of 0.02 ML Co on Al₂O₃/Ni₃Al(111) as a function of exposure time. The absorption spectrum taken with negative x-ray helicity changes significantly. The integrated $L_{2,3}$ intensity follows the solid line in Fig. 3.6 b). On the contrary, the integrated μ_+ absorption intensity decreases by only 1% for two successive spectra. Since the spectra recorded with positive x-ray helicity are much more stable over time we take one μ_+ spectrum, acquired at $t = 900$ s, as reference for comparison with the μ_- spectra. When moving the x-beam over the sample to a new region, not exposed before, the integrated $L_{2,3}$ peak intensity recovers to 96%. The remaining difference may be due to sample inhomogeneity or sample changes over

time	$\frac{L}{S+7D}$	$\frac{I(L_3)}{I(L_2)+I(L_3)}$
0 s	0.92 ± 0.06	0.90 ± 0.03
150 s	0.90 ± 0.06	0.89 ± 0.03
300 s	0.91 ± 0.06	0.90 ± 0.03
450 s	0.95 ± 0.06	0.89 ± 0.03
600 s	0.96 ± 0.06	0.90 ± 0.03
750 s	0.99 ± 0.06	0.91 ± 0.03
1800 s	0.88 ± 0.06	0.91 ± 0.03

Table 3.2: Ratio $L/(S + 7D)$ and branching ratio $I(L_3)/(I(L_2) + I(L_3))$ as a function of recording time calculated for the spectra shown in Fig. 3.6.

time out of the focussed x-beam. Note that the change of the white line intensity is not reversible, as has been verified by temporarily switching off the x-beam and recording again a spectrum after 30 min. The dramatic changes in the absorption and dichroism lineshape are mainly induced by the x-ray beam. To evaluate possible reasons for these changes we discuss different atomistic processes.

Metal atoms on isolating surfaces are only weakly bound to the substrate which often entails smaller migration barriers E_m than the one of metal on metal systems [71]. For Co on h-BN we found $E_m = 23 \pm 3$ meV [70]. With a typical attempt frequency of $\nu_0 = 10^{13} \text{ s}^{-1}$, we obtain at $T = 8$ K a hopping rate of $\nu = \nu_0 e^{-\frac{E_m}{k_B T}} = 0.03 \text{ s}^{-1}$, i.e., a probability of 3% for hopping from one site to the next in one second. Increasing the temperature by 1 K leads to one event per second, and at $T = 10$ K each atom makes 26 random walk steps per second. Au atoms on a thin alumina film on NiAl(110) are still mobile at the deposition temperature of ~ 10 K but immobile at $T = 5$ K [92]. If we assume a migration barrier similar to the one on h-BN, we recognize that already 1 min after the ending of deposition no more monomers are present due to the high adatom mobility. This is in contrast with the experimental observation of monomers on the surface after cooling the system from 10 K to 5 K. Hence, E_m must be higher than 23 meV for Au/Al₂O₃/NiAl(110). For our system Co/Al₂O₃/Ni₃Al(111) active surface diffusion would lead to aggregation and therefore we would expect a constant decrease of the ratio $r = L/(S+7D)$ due to increasing coordination [63,1]. However, r values reported in table 3.2 as a function of exposure time are found to be unchanged within the error bar. Possibly, L and S change simultaneously which means that also S decreases, passing from a high spin to a low spin state. However, the constant and particular high branching ratio (see table 3.2) over time supports a maintained high spin state. This strongly supports a time independent atom coordination and excludes coarsening. We performed KMC

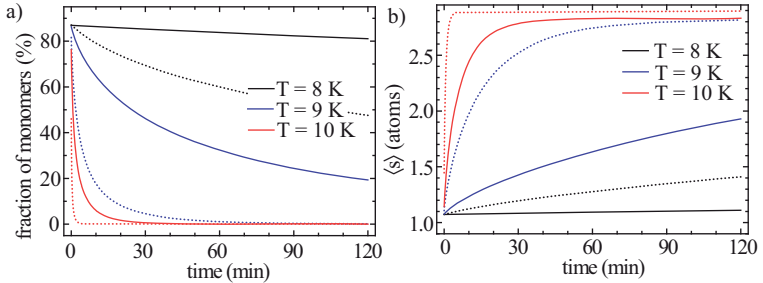


Figure 3.7: KMC simulation of deposition of 0.02 ML with a flux of 10^{-3} ML/s on a hexagonal lattice and subsequent coarsening caused by monomer diffusion with $E_m = 27$ meV (solid line) and $E_m = 25$ meV (dotted line) at different temperatures. a) Fraction of monomers as a function of time. b) Mean island size $\langle s \rangle$ as a function of time. $t = 0$ s corresponds to the moment when deposition is accomplished. Note that during deposition diffusion is also active.

simulations at three different temperatures for $E_m = 25$ meV and $E_m = 27$ meV in order to highlight the effect of the monomer diffusion on the abundance of single atoms at the surface and the mean island size on our experimental timescale of about two hours [93]. The outcome is represented in Fig. 3.7. To explain the observed stability at $T = 8$ K a minimum diffusion barrier of $E_m = 27$ meV is needed.

The fact that $\int_{L_2+L_3}(\mu_+ + \mu_-)$, which is proportional to the d holes and therewith the coverage, decreases with exposure time can be explained by atom desorption. The desorption rate D is given by

$$D = \nu_0 e^{-\frac{E_d}{k_B T}} = \frac{\int_{L_2+L_3}(\mu_+ + \mu_-)}{t}, \quad (3.3)$$

ν_0 being the attempt frequency and E_d the energy barrier for desorption. We find that the total integrated absorption intensity $\int_{L_2+L_3}(\mu_+ + \mu_-)$ decreases under the x-ray beam by 28% in 1800s. This yields a desorption rate of $D = (1.56 \pm 0.16) \times 10^{-4} \text{s}^{-1}$. Remember that the change of the spectral shape is strongly accelerated under the x-ray beam. Possible explanations are *i)* the desorption barrier is lowered while T remains unchanged, *ii)* the sample is locally heated during the absorption process, or *iii)* the absorption process is not thermally activated but induced by the photons.

Considering assumption *i)*, we calculate the desorption barrier at $T = 8$ K with a typical attempt frequency of $\nu_0 = 10^{13} \text{s}^{-1}$ and we obtain $E_d = 27.0$ meV. For comparison, we evaluate equation (3.3) off the x-ray beam, attributing the variation $\Delta \int_{L_2+L_3}(\mu_+ + \mu_-) = -4\%$ in one hour to thermal desorption. This yields $E_d = 28.5$ meV and implies a reduction of the desorption barrier by 10% due to x-ray irradiation. After assumption *ii)* the

	$s = 1$	$s = 2$	$s = 3$	$s = 4$	$s = 5$	$s = 6$	$s = 7$	$s = 8$	$s = 9$	$s = 10$	$\langle s \rangle$
$T = 8 \text{ K}$	36.4%	23.3%	14.9%	9.4%	5.9%	3.7%	2.4%	1.5%	0.9%	0.6%	1.73
$T = 10 \text{ K}$	7.0%	13.4%	16.1%	15.3%	12.9%	10.0%	7.4%	5.2%	3.7%	2.6%	3.33

Table 3.3: KMC simulations for 0.14 ML Fe using $E_m = 27 \text{ meV}$ and $\nu_0 = 10^{13} \text{ s}^{-1}$ deposited with a flux of 10^{-3} ML/s at $T = 8 \text{ K}$ and 10 K .

sample is locally heated during the absorption process. By increasing the sample temperature, diffusion processes become more important (see Fig. 3.7) entailing aggregation. The nucleation rate is [94]

$$J = \sigma_1 \Theta^2 \nu_0 e^{-\frac{E_m}{k_B T}}, \quad (3.4)$$

where σ_1 is the monomer capture number, typically $\sigma_1 = 3$ [95] and Θ the coverage. For $\Theta = 0.02 \text{ ML}$ and $E_m = 27 \text{ meV}$ we calculate J/D at $T = 8.5 \text{ K}$ and obtain $J/D = 0.01$, favoring desorption. Further increases in temperature yield larger J/D meaning that nucleation becomes more important at higher temperature compared with desorption.

For *iii*), a photon induced desorption process, we can express the desorption rate as

$$D = \sigma e \Theta A F_{ph} \quad (3.5)$$

where σ the x-ray absorption probability, e (*efficiency*) the portion of x-ray absorptions leading to desorption, Θ the coverage, A the area of one adsorption site, and F_{ph} the photon flux. For Co the x-ray absorption probability is about $\sigma = 10^{-2} \text{ photons}^{-1}$ at the L_3 peak [46], the photon flux is typically $10^{13} \text{ photons}/(\text{s}\cdot\text{mm}^2)$ [96] and the area of one absorption site is about $A = 6 \times 10^{-14} \text{ mm}^2$. For $\Theta = 0.02 \text{ ML}$ and $D = 1.56 \times 10^{-4} \text{ s}^{-1}$ this yields $e \simeq 1$. Hence, each x-ray absorption leads to desorption.

3.2.5 Larger Fe clusters

For larger coverages where most of the atoms form small clusters of a few atoms the strong multiplet features of XAS and XMCD spectra vanish and they look more like bulk Fe due to hybridization among Fe atoms [15]. The investigated system does not change over the investigation time of two hours, which allows us to take XAS at 0° and 70° as well as magnetization curves at both angles for Fe and at $\theta = 70^\circ$ for Ni. The data are summarized in Fig. 3.8. From the shape of the magnetization curve shown in Fig. 3.8 b) we deduce an out-of-plane easy axis and note that the magnetization is close to saturation at 0° . We can therefore calculate the orbital and spin magnetic moment by means of the sum rules. With a typical value of $h_d = 3.4$ [15] for the number of d -holes we obtain $L = 0.30 \pm 0.04 \mu_B$ and $S + 7D = 2.31 \pm 0.14 \mu_B$. We remark that iron oxides often order ferrimagnetically or antiferromagnetically which is obviously not the case here [89, 97]. The spin moment is large suggesting ferromagnetic alignment of the Fe moments. $S + 7D$

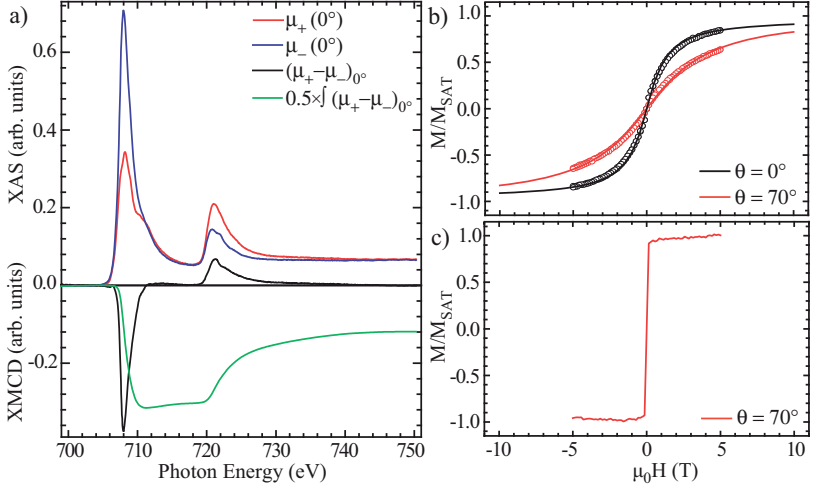


Figure 3.8: 0.14±0.03 ML Fe/Al₂O₃/Ni₃Al(111) measured at $T = 8$ K. a) XAS, resulting XMCD, and corresponding integral taken at Fe $L_{2,3}$ edges at $\mu_0 H = 5$ T with right and left circularly polarized light for $\theta = 0^\circ$. b) Fe magnetization curves (open circles) representing the peak of the L_3 XMCD intensity at 708.0 eV divided by the pre-edge intensity at 704.0 eV as a function of \mathbf{H} . The solid line is the fit for $s = 3.4$ and $K = 0.50$ meV/atom. c) Ni magnetization curves measured representing the peak of the L_3 XMCD intensity at 853.1 eV divided by the pre-edge intensity at 849.8 eV as a function of \mathbf{H} .

agrees very well with the spin moment found for O₂-Fe(TPA)₄ [11] and the Fe monolayer on Rh(111) (see table 4.3).

Further, we determine the MAE from the magnetization loops using equation (3.1). From experiment we know the temperature T , the external field H , and the magnetic moment $m = L + S$ per Fe atom when neglecting the spin dipole moment. The best fit of the hysteresis curves is obtained for $T = 8$ K and $m = 2.6 \pm 0.2 \mu_B$ /atom with $s = 3.4 \pm 0.4$ and $K = 0.50 \pm 0.05$ meV/atom. To test if $s = 3.4$ is reasonable for a coverage of 0.14 ML we used KMC simulations. At $T = 8$ K, our measurement temperature, diffusion is almost frozen and the cluster size distribution equals the statistic result as shown in the first line in table 3.3. To take account for a slightly increased sample temperature in presence of the hot evaporation source during deposition, we report in the second line in table 3.3 the cluster size distribution at $T = 10$ K. At 10 K surface diffusion of isolated Fe adatoms is active and leads to a mean cluster size $\langle s \rangle = 3.33$ which agrees very well with $s = 3.4 \pm 0.4$ inferred from fitting the hysteresis.

We remark that $K = 0.5$ meV/atom is a surprisingly large MAE. For comparison, bulk γ iron oxide has $K = 1.5 \mu\text{eV}/\text{Fe}_2\text{O}_3$ [98] and Co clusters on Pt(111) of the same size have $K = 3.3 \pm 0.2$ meV/Co atom [1]. The magnetization curve measured at the Ni edge has a square shape and substantially differs from the one measured at the Fe edge suggesting that the MAE is an intrinsic property of the Fe clusters and not due to an exchange or dipolar interaction with the magnetic Ni_3Al .

3.3 Cu_2N

The Cu_2N surface corresponds to the (001) face of a Cu_3N bulk crystal. Cu_3N is produced by depositing copper in a nitrogen atmosphere. It is an insulator and decomposes upon heating into N_2 and Cu at around 250°C [99]. In this peculiar structure the fcc sites are vacant and we will refer to this specific site as hollow. Alternatively, a single Cu_2N layer can be stabilized on Cu(001) and has a band gap of 4 eV [66]. A model of the Cu_2N network is shown in the inset in Fig. 3.9 a). On the Cu_2N surface Fe and Co atoms can bind on top of either N atoms which have fourfold in-plane symmetry, or Cu atoms having twofold in-plane symmetry. The stable adsorption site is on top of Cu. As soon as a magnetic field with an in-plane component is applied we have to distinguish two Cu sites. The atom on site A has two N atoms as its horizontal nearest neighbors (N-direction) whereas the atom on site B has no horizontal nearest neighbors (hollow-direction). Using IETS performed with a low-temperature STM it has been demonstrated that $3d$ atoms at Cu binding sites behave as single atomic spins with large MAE [9, 32]. The aim of our study was to compare the spin moments and MAE values obtained by IETS which is a new local probe technique with results from XMCD being a well established spatially averaging technique. XMCD gives information about the orbital and spin magnetic moment, their field dependence and consequently the easy axis and MAE of the system by acquiring hysteresis loops at different angles θ . With the results obtained by IETS we are able to predict the magnetization curves that we expect in our XMCD experiment. Therefore, a short description of the theoretical model used to describe the IETS measurements is given.

Spin excitations for an isolated atom in an anisotropic environment with axial symmetry are described by the spin Hamiltonian [9]

$$H = g\mu_B\mu_0 \mathbf{H} \cdot \mathbf{S} + D S_z^2 + E (S_x^2 - S_y^2), \quad (3.6)$$

where the first term is the Zeemann splitting of the states in the presence of a magnetic field \mathbf{H} with g being the Landé g -factor and $\mathbf{S} = (S_x, S_y, S_z)$ the spin operator. The second and third term are representations of the axial and transverse magnetic anisotropies, characterized by strengths D and E , respectively. By convention, the axes are assigned to maximize $|D|$ and have $E > 0$. Negative D values translate into an easy axis along z

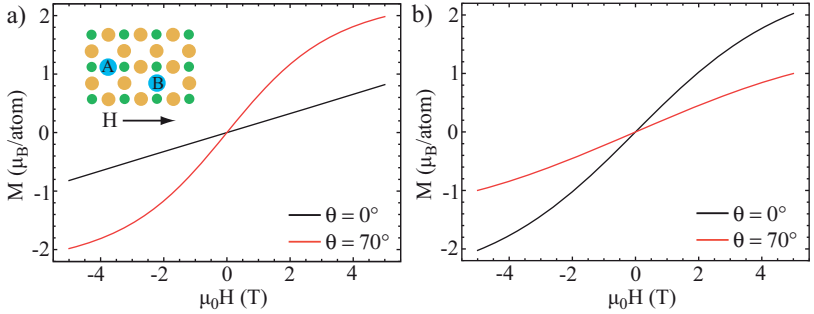


Figure 3.9: Expected magnetization curves for Fe a) and Co b) at $T = 8$ K. Inset: The markers A and B highlight the adsorption sites of non-equivalent in-plane directions on the Cu_2N lattice with respect to the applied magnetic field \mathbf{H} . Cu positions are yellow and N positions green.

and positive D values into a hard axis along z , too. For Fe, $D = -1.55 \pm 0.01$ meV and $E = 0.31 \pm 0.01$ meV was found with the assignment of the axes as follows: z is along the N direction, x along the hollow direction, and y perpendicular to the surface [9]. The quantum anisotropy energies D and E can be converted to the classical MAE by the correspondence principle. The MAE of a system with the same symmetry as described by equation (3.6) is given by $K \cos^2 \vartheta + K_{\parallel} \sin^2 \vartheta \cos 2\varphi$, where K represents the axial anisotropy along z and K_{\parallel} the transverse anisotropy. ϑ and φ are the polar and azimuthal angles of the magnetic moment. Hence, $K = D S^2$ and $K_{\parallel} = E S^2$. For Fe $S^2 = 4$ which yields $K = -6.20 \pm 0.04$ meV/atom and $K_{\parallel} = 1.24 \pm 0.04$ meV/atom. For Co having $S^2 = 9/4$ A. F. Otte *et al.* reported a strong magnetic hard axis along the hollow direction with $D = 2.75 \pm 0.05$ meV and $E = 0$ meV corresponding to classically $K = 6.19 \pm 0.11$ meV/atom and $K_{\parallel} = 0$ meV/atom [32].

By calculating the expectation value of the spin as a function of \mathbf{H} at $T = 8$ K we can plot the awaited magnetization curves. This was done for $\theta = 0^\circ$ and 70° and is shown in Fig. 3.9 a) and b) for Fe and Co, respectively. Note that for Fe as well as for Co saturation is reached at none of both angles in this bulk averaging technique. For Fe the saturated magnetic moment is $4 \mu_B$ and for Co $3 \mu_B$. As previously discussed, when applying the magnetic field at $\theta = 70^\circ$ (close to in-plane), we had to account for atoms sitting on non-equivalent adsorption sites A and B which we assume to be equally populated in our calculation. For Fe and Co, the difference of both branches of the hysteresis loop are large enough to be experimentally distinguished.

3.3.1 Sample Preparation

The Cu(001) single crystal was prepared by Ar⁺-ion sputtering at room temperature for 30 min ($P = 5 \times 10^{-6}$ mbar, 1 keV) and annealing for 10 min at 820 K. The Cu₂N surface was produced by sputtering the clean Cu sample for 4 min at 1 keV backfilling the chamber with 2×10^{-5} mbar N₂ gas, followed by annealing at 600 K for 2 min. The high voltage of the sputter gun dissociates the N₂ molecules, so that N ions are deposited on the Cu surface. The nitrogen atoms adsorb at the fourfold symmetric hollow sites on Cu(001) forming a c(2×2) phase [100]. The growth of the Cu₂N overlayer is self-limited to one atomic layer, i.e., longer sputtering periods do not lead to thicker Cu₂N films. However, we observe an increased surface roughness with sputtering time (compare Fig 3.10 a) and b)).

Lower Cu₂N coverage was obtained by reducing the sputtering time with nitrogen. The STM image in figure 3.10 a) shows a coverage of 35% with Cu₂N islands. These are of similar size and appear as depressions of 1.4 Å compared with the surrounding Cu which is a consequence of the decreased local density of states in the band gap [66]. The fact that compact islands form indicates an attractive interaction between the chemisorbed N atoms. As the islands grow the side length can reach up to 75 Å before they split up in two rectangles which can divide themselves again [101]. The lateral size of the islands is limited because of the incommensurability of the c(2×2)-N structure and the bare Cu(001) surface [100,102]. This results in an ideal island size which is a compromise optimizing strain and edge energy [103]. The self-organized arrangement of the islands is caused by their mutual repulsion mediated by the substrate [104]. A complete film of Cu₂N as shown in Fig. 3.10 b) and c) exhibits trenches running in the ⟨110⟩ directions which can be explained by missing Cu atoms in the surface layer [100]. The trenches are found at 45° with respect to the grid of missing N rows separating the Cu₂N islands. A special STM tip state allows the resolution of the trenches and the grid simultaneously. The LEED pattern of such a complete film (see Fig. 3.10 d)) shows sharp spots of the c(2×2) arrangement of the N atoms.

3.3.2 Single Fe and Co atoms on Cu₂N/Cu(001)

The sample was oriented such that the external field was along the N, respectively, hollow direction. We deposited minute amounts of Fe or Co at the lowest available temperature, $T = 8$ K, with a commercial e-beam evaporator from high purity Fe and Co rods. On the nitride surface, Fe and Co atoms can bind either on top of the Cu atoms or the N atoms. Assuming statistic growth, the adatoms are twice as frequent on Cu in agreement with STM observations. Adatom diffusion or desorption is of no concern for our experiment on the Cu₂N surface, which is strongly corrugated [105]. The adatoms form covalent bonds with the N atoms making them stable up to at least 15 K [32]. Defects within the Cu₂N

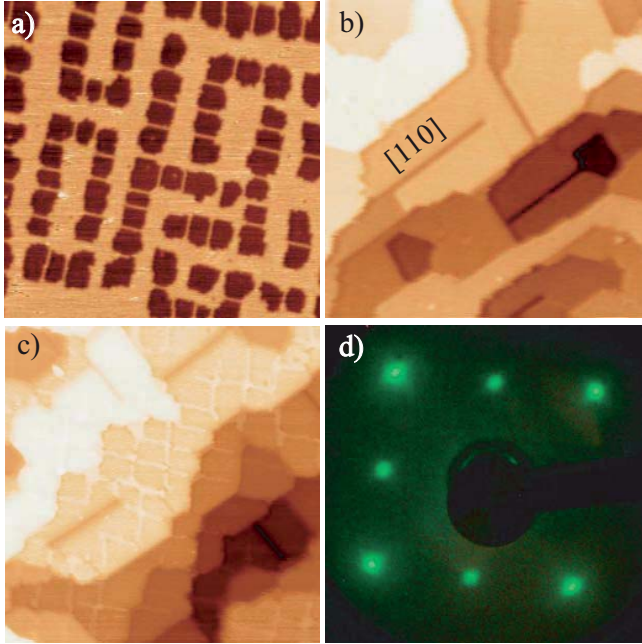


Figure 3.10: $\text{Cu}_2\text{N}/\text{Cu}(001)$ a) STM image of $\text{Cu}(001)$ partially covered with dark imaged $c(2\times 2)$ nitrogen islands ($500 \text{ \AA} \times 500 \text{ \AA}$, $V_T = 2.3 \text{ V}$, $I_T = 2.7 \text{ nA}$). b) STM image of the entirely covered surface evidencing trenches running along the $\langle 110 \rangle$ directions ($500 \text{ \AA} \times 500 \text{ \AA}$, $V_T = -1.0 \text{ V}$, $I_T = 7.4 \text{ nA}$). c) A changed tip contrast reveals the boundaries of the Cu_2N islands ($500 \text{ \AA} \times 500 \text{ \AA}$, $V_T = -0.5 \text{ V}$, $I_T = 2.7 \text{ nA}$) d) LEED pattern evidencing the $c(2\times 2)$ structure of a fully covered surface ($E = 58 \text{ eV}$).

islands are seldom [102]. However, adsorption sites at the island's edge amount to 15% of the total adsorption sites for a $50 \text{ \AA} \times 50 \text{ \AA}$ area. In addition to these, atoms can adsorb next to or on trenches. In an STM study 25% of the deposited atoms are found off the nitride areas.

XAS of 0.02 ML of Fe and Co, respectively, are shown in Fig. 3.11. We remark that the absorption spectra of isolated Fe and Co atoms on Cu_2N have only a faint multiplet structure compared with Fe and Co on Al_2O_3 presented in section 3.2. A closer look nevertheless demonstrates small features which are absent in fully hybridized samples. Taking Fe as an example the μ_- spectrum on Cu_2N shown in Fig. 3.11 a) exhibits two small peaks at 706.6 eV and 710.0 eV which can be distinguished from the main peak

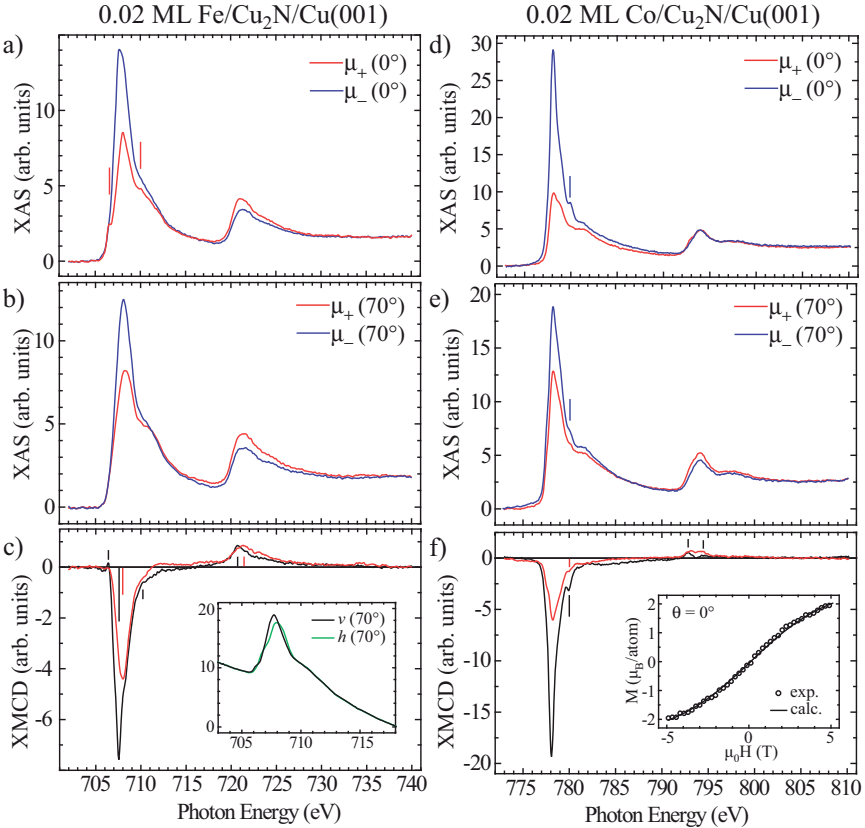


Figure 3.11: a) and b) XAS taken at Fe $L_{2,3}$ edges at $T = 8$ K and $\mu_0 H = 5$ T with right and left circularly polarized light at $\theta = 0^\circ$ and $\theta = 70^\circ$, respectively. The spectra at $\theta = 70^\circ$ have been normalized to the $\int(\mu_+ + \mu_-)L_3$ intensity at $\theta = 0^\circ$ to eliminate the dependence of the electron yield on the sample orientation. The background was subtracted. c) Resulting XMCD spectra. Inset: XAS with linearly polarized light. v and h designate vertical and horizontal alignment of the electric field vector as defined in Fig. 2.1. v compares with the sum of circular spectra at 0° . d) and e) XAS taken at Co $L_{2,3}$ edges at $T = 8$ K and $\mu_0 H = 5$ T with right and left circularly polarized light at $\theta = 0^\circ$ and $\theta = 70^\circ$, respectively. Normalization and background subtraction as in a) and b). f) Resulting XMCD spectra. Inset: Co magnetization curves (open circles) at $\theta = 0^\circ$ and expected magnetization curve as in Fig. 3.9 b).

		L	$S + 7D$	$\frac{L}{S+7D}$	easy axis
Fe/Cu	0°	0.72 ± 0.10	2.04 ± 0.20	0.36 ± 0.04	↑
	70°	0.40 ± 0.05	1.39 ± 0.15	0.29 ± 0.03	
Fe/ Cu_2N	0°	0.50 ± 0.10	2.06 ± 0.10	0.24 ± 0.02	↑
	70°	0.06 ± 0.02	1.75 ± 0.20	0.04 ± 0.02	
Co/ Cu_2N	0°	1.20 ± 0.15	1.95 ± 0.20	0.62 ± 0.02	↑
	70°	0.42 ± 0.10	1.02 ± 0.10	0.41 ± 0.02	

Table 3.4: Sum rule analysis. L and $S + 7D$ are given in μ_B/atom and calculated using $h_d = 4$ for Fe and $h_d = 3$ for Co. Note that L and $S + 7D$ are not saturated. ↑ stands for an out-of-plane easy axis. Compare also with the values given in Ref. 11 for Fe/Cu(001).

at 707.6 eV. The two extra peaks are absent in the spectrum measured for Fe on bare Cu(001) and shown in Fig. 3.12. Comparing the XMCD spectra for Fe/ Cu_2N at 0° and 70° shown in Fig. 3.11 c) we find that the L_3 peak shifts from 707.6 eV at normal incidence by 0.4 eV to higher energy at grazing incidence, and similarly the L_2 peak shifts by approximately 0.6 eV. The peak positions of the XAS shift by the very same amount even though being less evident. Again, this is a linear dichroism effect becoming obvious when looking at the linear XAS displayed in the inset in Fig. 3.11 c). From sum rule analysis, summarized in table 3.4, we obtain a large $r = 0.24 \pm 0.02$ at 0°, nevertheless slightly reduced compared with Fe on bare Cu(001) ($r = 0.36 \pm 0.04$). This is surprising because we would expect that the Fe d orbitals are screened by the Cu_2N layer and that the highly localized d states lead to atomic-like orbital moments. From the magnetic field dependence of the IETS spectra a spin of 2 was deduced equal to the free Fe atom in d^6 configuration [9]. This yields $L/S = 1/2$ neglecting the dipolar term and $L/(S + 7D) = 1$ including the dipolar term. Hybridization with the conduction electrons of the substrate, other than quenching L , tends to transfer charge to the d states of the adatom. The enhanced r for Fe/Cu(001) may reflect a prevalent d^7 configuration having $L/S = 2$ and $L/(S + 7D) = 3/2$, respectively. Note that the number of d holes is 3.5 for Fe impurities in bulk Cu [106]. Further, we observe for Fe/ Cu_2N that L is almost quenched at 70°. According to Bruno’s formula [21] a large anisotropy of the orbital moment is directly linked to the MAE, suggesting a giant MAE with out-of-plane easy axis, contrary to what is expected from the IETS data.

For Fe/Cu(001) r is larger for 0° than for 70° highlighting an out-of-plane easy axis in agreement with the larger XMCD intensity at $\theta = 0^\circ$, the magnetization curves in the inset in Fig. 3.12 c), and Ref. 11. Our $L/(S + 7D)$ ratio is 0.36 at 0° and 0.29 at 70° in good agreement with $r = 0.25 \pm 0.05$ obtained for 0.016 ML Fe/Cu(001) [64].

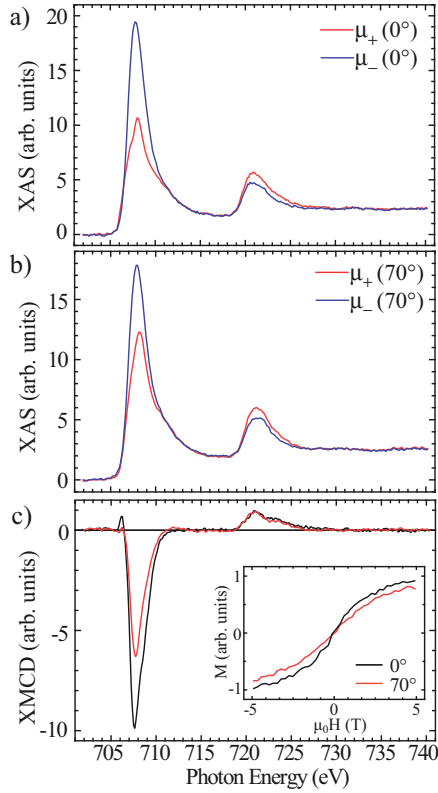


Figure 3.12: 0.015 ML Fe/Cu(001) a) and b) XAS taken at Fe $L_{2,3}$ edges at $T = 8$ K and $\mu_0 H = 5$ T with right and left circularly polarized light at $\theta = 0^\circ$ and $\theta = 70^\circ$, respectively. The spectra at $\theta = 70^\circ$ have been normalized to the $\int(\mu_+ + \mu_-)L_3$ intensity at $\theta = 0^\circ$ to eliminate the dependence of the electron yield on the sample orientation. The background was subtracted. c) Resulting XMCD spectra. Inset: Fe magnetization curves representing the peak of the L_3 XMCD intensity at 707.0 eV divided by the pre-edge intensity at 705.0 eV as a function of \mathbf{H} .

For Co/Cu₂N we observe a satellite peak at 780.0 eV in the XAS and XMCD spectra. Moreover, the XMCD signal evidences a double peak structure of the L_2 edge. These features are common with the Co/Al₂O₃ spectra (see Fig. 3.5). However, the sign of the L_2 XMCD signal is positive which is typical for an increased crystal field [85]. Consequently,

the branching ratio is smaller, 0.84 for Co/Cu₂N whereas it was 0.92 for Co/Al₂O₃ [90,107]. At 0° the small, even though positive, L_2 XMCD area yields a $L/(S+7D)$ ratio of 0.62, which is close to but smaller than the statistic $r = 2/3$. Also for Co we find a perpendicular easy axis, this time in agreement with our expectation. At 70° L , $(S+7D)$, and $L/(S+7D)$ are smaller because of the large MAE impeding the alignment of the magnetic moment along the applied field direction. To investigate the field dependence, we recorded a magnetization curve along the easy axis and scaled it to the spin moment $S+7D = 1.95 \pm 0.20 \mu_B/\text{atom}$ at 5 T (see Fig. 3.11 c). We obtain very good agreement of the expected and measured curves. Along the hard axis we have not acquired $M(H)$, but we remark that $S+7D = 1.02 \pm 0.10 \mu_B/\text{atom}$ as reported in table 3.4, in very good agreement with the expected spin value of 1.0 μ_B as we can read from Fig 3.9 b) for $\theta = 70^\circ$ at 5 T.

3.3.3 XMCD versus IETS results

XMCD and IETS results compare very well for Co, while it is not the case for Fe suggesting that a more careful analysis is needed. XMCD is an averaging technique, and the total XAS respective XMCD signal is a combination of all adatomic species. Remember that half of them sit on top of Cu within the nitride area, 25% on top of N in the nitride area, and 25% elsewhere. Thus, 50% of the adatoms should produce a magnetization curve as shown in Fig. 3.9, whereas the remaining 50% eventually exhibit different magnetic behavior. The 25% sitting on top of N are in-plane symmetrically bound and out-of-plane axial behavior is expected, i.e., $E = 0$ or $K_{\parallel} = 0$. Preliminary IETS measurements of Fe on N binding sites reveal that part of them are isotropic ($D = 0$ meV) [105], while others exhibit a giant MAE of $D \simeq -6$ meV with out-of-plane easy axis [108]. Assuming the remaining 25% to behave like on the bare Cu(001) surface, we have to account for the observed out-of-plane easy axis in the total XMCD signal (see Fig. 3.12 and Ref. 11). For Co on top of N to date only isotropic behavior is known [105,108]. Co/Cu(001) is a Kondo system with a Kondo temperature of $T_K = 88$ K [109]. Below T_K the conduction electrons align their spins to screen the spin of the local moment. A many-body singlet state is thus formed, consisting of the local magnetic impurity surrounded by a spin compensation cloud of conduction electrons, such that no net moment remains at the Kondo site. The absence of magnetic signature of Co impurities on Cu(111) or Ag(001), which are both Kondo systems, was demonstrated in a scanning tunneling spectroscopy experiment with a superconducting tip [110, 111, 17]. No states were observed in the superconducting gap while magnetic Gd trimers on Cu(001) induce gap states in spectra acquired with a Nb tip [112].

In conclusion, STM based measurements distinguish for Fe on top of Cu an easy axis in-plane along the N direction from an intermediate axis out-of-plane and a hard axis

along the hollow direction. Fe/Cu(001) is out-of-plane and Fe on N is either isotropic or strongly out-of-plane. With XMCD an out-of-plane easy-axis is observed which is finally not a contradiction to IETS. For Co a hard axis along the hollow direction is found which translates into an effective out-of-plane easy axis. The good agreement of IETS and XMCD is due to the isotropic contribution of Co on top of N and the absence of magnetism of Co on Cu(001).

Chapter 4

Co and Fe ultra-thin films on highly polarizable substrates

Exploring the ultimate density limits of magnetic information storage requires elaborate tuning of several magnetic properties, such as the easy magnetization axis, the magnetic anisotropy energy K , and the saturation magnetization M_{SAT} of the recording medium [113]. In order to inhibit thermally activated magnetization reversal the MAE has to be 1.2 eV per bit. Reducing the bit size therefore requires a higher MAE per atom. At the same time, the magnetization density of the recording medium must increase in order to stay within technologically available writing fields. Further, the easy axis has to be perpendicular to the plane to reduce dipolar magnetic interactions between adjacent bits, and finally narrow switching and stray field distributions are required.

As the typical size of nanoparticles and the thickness of thin films approach a few atomic lattice distances, electronic interactions between the magnetic medium and the supporting substrate play an increasingly important role and lead to new properties opening up a new degree of freedom. The effect of electronic hybridization with the substrate is well exemplified by the magnetic behavior observed for surface-adsorbed individual atoms as discussed in chapter 3. For example, a giant magnetic anisotropy has been found for single Co atoms on Pt(111) [1], a $5d$ transition metal, while vanishing MAE values have been observed for single Co atoms when deposited on alkali metals, where only $3d - sp$ hybridization is possible [72]. In addition to electronic change via adatom-substrate hybridization, in thin films the lattice mismatch between film and substrate can induce modifications of the crystallographic translational symmetry, which may result in additional modifications of the magnetic properties [114].

In this chapter we focus on Fe and Co ultra-thin films on highly polarizable substrates, namely Pt(111) and Rh(111). Pt and Rh have a very similar lattice constant (3.92 Å for Pt and 3.80 Å for Rh), one s electron in the valence shell, and an almost full $3d$ shell (9 electrons for Pt and 8 electrons for Rh). However, Pt is a $5d$ transition metal whereas Rh

is a $4d$ suggesting from our results obtained for the single atoms (see section 3.1) that the contribution to the MAE is more important in case of Pt than for Rh due to the larger spin-orbit coupling constant of the polarized substrate [46].

Furthermore, regarding the development of new materials having high MAE and M_{SAT} bimetallic alloys represent a viable route to tune the MAE and M_{SAT} , as these quantities are strongly influenced by compositional effects and lattice distortions. While the MAE of ferromagnetic transition metals in their cubic structures is of the order of a few tens of $\mu\text{eV}/\text{atom}$, structurally distorted alloys, such as FePt in the $L1_0$ phase [115, 116, 117] or bct-FeCo [34, 118, 35] may have MAE values close to $1 \text{ meV}/\text{atom}$. Moreover, the total magnetic moment can be tuned by choosing the two elements of the alloy. FePt and FeCo are good examples of alloys with comparable MAE but with respectively lower and higher magnetic moment than the Fe and Co bulk value. In order to maximize the magnetic moment and to shed some light on the mechanism of MAE enhancement, we have investigated the effect of alloying Fe and Co in one atom thick films on Pt(111) and the effect of the substrate by comparing pure Fe and Co films on Pt(111) with such on Rh(111).

The investigation is a combined experimental and theoretical work giving insight to magnetic and electronic properties. Experimentally, we used scanning tunneling microscopy, x-ray absorption spectroscopy, x-ray magnetic circular dichroism, and magneto-optical Kerr effect measurements to characterize the morphology and magnetic properties. Theoretic investigations were carried out in the group of P. Weinberger for $\text{Fe}_x\text{Co}_{1-x}$ on Pt(111) and in the one of J. Hafner for Fe and Co on Rh(111).

In section 4.1 we present the results of 1 ML thick $\text{Fe}_x\text{Co}_{1-x}$ alloy films on Pt(111) with $0 \leq x \leq 1$. Theoretical calculations were performed using first principle electronic structure calculations (for details see Ref. 28). The calculated Fe and Co spin moments are only weakly composition dependent and close to $3 \mu_B/\text{atom}$ and $2 \mu_B/\text{atom}$, respectively. This trend is in agreement with the experimental data, except for pure Fe where an effective spin moment of only $S_{eff} = 1.2 \pm 0.2 \mu_B/\text{atom}$ was measured. The strictly decreasing M_{SAT} from Fe to Co of the alloy film is in contrast to the well-known Slater-Pauling behavior finding a maximum of M_{SAT} at intermediate composition for bulk iron cobalt alloys [119]. However, the orbital moment and the MAE of $\text{Fe}_x\text{Co}_{1-x}/\text{Pt}(111)$ show a strong composition dependence with maxima close to the $\text{Fe}_{0.5}\text{Co}_{0.5}$ stoichiometry. A MAE of $K = 0.5 \text{ meV}/\text{atom}$ was found experimentally and theoretically, which is more than two orders of magnitude larger than the value observed in bulk bcc FeCo [120].

In section 4.2 we focus on Fe and Co films with varying thickness between 1 ML and 6 ML, deposited on Rh(111). Density functional theory (DFT) calculations were carried out using the Vienna ab initio simulation package [121]. The predicted spin moment is for the monolayer $3 \mu_B/\text{Fe}$ atom and $2 \mu_B/\text{Co}$ atom, in excellent agreement with the experimental results. From the experiment we obtain an enhanced orbital moment and

MAE compared with bulk. We found that the easy magnetization axis is out-of-plane for 1 ML Fe/Rh(111) and in-plane for 1 ML Co/Rh(111). For Co/Rh(111) we observe a twofold spin reorientation transition as a function of film thickness. The easy axis is in-plane for 1 ML, out-of-plane for 2 ML and again in-plane for ≥ 3 ML Co/Rh(111). Fe/Rh(111) turns from out-of-plane to in-plane at 4 ML coverage. X-ray absorption spectra measured at the Rh $M_{2,3}$ edges evidence the magnetic polarization of the substrate by the adsorbed Fe and Co layer.

4.1 $\text{Fe}_x\text{Co}_{1-x}$ monolayers on Pt(111)

$\text{Fe}_x\text{Co}_{1-x}$ films were grown by atomic beam epitaxy from thoroughly outgassed high-purity rods (99.995%) using a commercial electron beam evaporator. The Pt(111) substrate was prepared by repeated cycles of Ar^+ -ion sputtering (1.3 keV, $1 \mu\text{A}/\text{cm}^2$, at $T = 300$ K to remove magnetic layers and at $T = 800$ K once the substrate was clean for 20 minutes), followed by annealing at $T = 800$ K at an oxygen partial pressure of $P_{O_2} = 6 \times 10^{-8}$ mbar for 10 minutes to remove carbon impurities, and final annealing to 1100 – 1300 K. This preparation procedure gives chemical defect densities below 2×10^{-3} ML and typical terrace sizes of about 1000 Å. Fe and Co atoms were co-deposited on the surface. The film coverage and chemical composition were adjusted by varying the Fe and Co fluxes, which were previously calibrated by STM and XAS within ± 0.05 ML for a full ML. The evaporation rate for Fe and Co was in the range 0.1 – 0.6 ML/min. During deposition the pressure inside the UHV chamber was below 1×10^{-10} mbar. To investigate the effect of the film morphology on the magnetic properties, two types of monolayer thick films were grown with either a granular or continuous structure.

Granular films for MOKE experiments have been deposited at $T < 50$ K, where surface diffusion of both species is frozen. Their morphology has been investigated in detail by variable temperature scanning tunnelling microscopy (VT-STM). Analog growth conditions were used to deposit and investigate *in situ* the granular films by XAS using synchrotron radiation. All XAS measurements presented here have been performed at $T = 10$ K and in less than 2 hours after deposition. The coverage calibration at the ESRF has been carried out *in situ* by STM after warming up the samples and transferring them from the cryostat to the STM of the ID08 beamline.

Continuous films were investigated by VT-STM and MOKE measurements with an experimental setup described elsewhere [122]. The films were grown at $T = 35$ K and then annealed at $T = 300$ K for 5 min. MOKE measurements were performed in polar and transverse configuration as a function of the stoichiometry in the temperature range from $T = 35$ K to $T = 400$ K. An electromagnet with magnetic poles, respectively, a coil inside the vacuum system were used to produce in-plane and out-of-plane magnetic fields of up to 50 mT at the sample position. The light source was a p -polarized and temperature

stabilized 780 nm laser diode. The angle between the incident beam and the surface normal was 35° . Magnetization curves were acquired by MOKE in temperature intervals of 10 K. A complete characterization of the magnetic properties was always performed in less than 2 hours after growth and at a pressure of 4×10^{-11} mbar. A maximum variation of the coercive field of ± 1.5 mT was measured when the MOKE experiments were repeated after 2 hours. We have taken this value as error bar for the measurements of the coercive field.

4.1.1 Structural results from STM

Figure 4.1 a) shows an STM image of the granular film structure obtained after deposition of 0.6 ML of Co on Pt(111) at 35 K. The observed morphology was independent of the film stoichiometry and of the deposition temperature up to 50 K. Up to this temperature the surface diffusion of Co and Fe is frozen giving rise to statistical growth of islands with density, size, and morphology being independent of composition [123]. From the STM images, we estimated a mean grain diameter of about 20 Å which corresponds to an average grain size of about 50 atoms. The grain thickness is one atomic layer; only 0.02 ML are in the second layer. This value implies a low activation energy for interlayer diffusion which is reasonable for the small island sizes of only 8 atoms in diameter. The lattice misfit between Fe and Pt is -10.3% ¹ and the one between Co and Pt is -9.4% . Despite these large values STM measurements do not reveal surface partial dislocations in the islands for all stoichiometries, suggesting pseudomorphic growth of the $\text{Fe}_x\text{Co}_{1-x}$ alloy islands. This can be rationalized by stress relief at the steps [124], which leads for Co/Pt(111) to an island diameter of 30-40 Å up to which the islands are pseudomorphic and beyond which they have partial dislocations, where the stacking changes from fcc to hcp or vice versa [125]. For Fe on Pt(111) pseudomorphic growth has been observed up to completion of the first monolayer [126], which is surprising when considering the large lattice misfit and implies large tensile stress.

Continuous films were grown by depositing 1 ML of $\text{Fe}_x\text{Co}_{1-x}$ at temperatures lower than $T = 50$ K and subsequent annealing at $T = 300$ K. This procedure presents two advantages in comparison with deposition directly at room temperature. First, the film morphology is composition independent as diffusion is entirely frozen for both elements during deposition, and second the morphology is coming closest to an ideal flat and defect-free single layer. Examples are shown in Fig. 4.1 for monolayers formed of pure Co and of $\text{Fe}_{0.40}\text{Co}_{0.60}$. Second layer coverage represents less than 4% of the total coverage. For comparison, second layer coverage amounts to about 30% for 1 ML of Co [127] and 1 ML of Fe [126] deposited at room temperature. This is due to the large island sizes created at 300 K making it more difficult for second layer atoms to descend before nucleation of a

¹The lattice mismatch is defined as $(d_{\text{Fe}} - d_{\text{Pt}})/d_{\text{Pt}}$, where d_x is the in-plane nearest neighbor distance.

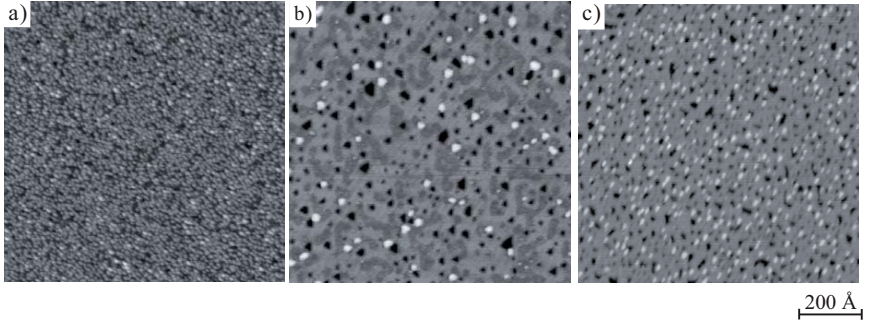


Figure 4.1: a) STM image of 0.60 ± 0.05 ML Co/Pt(111) deposited and imaged at $T = 35$ K. The surface exhibits monolayer-thick grains containing 50 atoms on average. b) STM image of 1.00 ± 0.05 ML Co/Pt(111) grown at $T = 35$ K and annealed at $T = 300$ K for 5 min. c) STM image of 1.00 ± 0.05 ML $\text{Fe}_{0.40}\text{Co}_{0.60}$ /Pt(111) again grown at $T = 35$ K and annealed at $T = 300$ K for 5 min.

second layer island. For low temperature growth, the density of second layer islands and first layer vacancies was only 8×10^{-3} ML and this independent of stoichiometry allowing to minimize the effect of film roughness on the magnetic properties [33, 128]. Randomly distributed partial dislocations are observed for all compositions, except for pure Fe. The partial surface dislocations are the domain walls separating fcc from hcp stacking areas. Depending on the tip conditions, they appear as bright lines as for example in Fig. 4.12, or the two stacking sequences appear with different heights, as in Fig. 4.1. In both cases the apparent height differences amount to 0.25 ± 0.05 Å. Although surface partial dislocations have been observed for pure Co [127], but not for pure Fe [126], a clear correlation between dislocation density and film chemical composition could not be detected. These findings are in agreement with the random chemical order due to the growth by co-deposition at temperatures low enough to suppress surface diffusion.

Experiments carried out above room temperature revealed structural evolutions such as segregation of adatoms on top of the first layer. Previous experimental and theoretical studies were focused on the structural evolutions occurring above room temperature, e.g. insertion of atoms in the substrate [127], intermixing [129, 130, 131] or adatom segregation at the film surface [132]. In order to have monolayers of well-defined composition and structure we restrict ourselves to the temperature range where structural evolution is absent.

	$\Theta(ML)$	L_{Fe}	$(S_{eff})_{Fe}$	$\left(\frac{L}{S_{eff}}\right)_{Fe}$	L_{Co}	$(S_{eff})_{Co}$	$\left(\frac{L}{S_{eff}}\right)_{Co}$	\bar{L}	\bar{S}_{eff}	$\frac{M_{5T}}{M_{SAT}}$
Co	Ref. 1	-	-	-	0.31 ± 0.06	1.8 ± 0.1	0.17 ± 0.02	0.31 ± 0.06	1.8 ± 0.1	1
Fe _{0.35} Co _{0.65}	0.83 ± 0.05	0.30 ± 0.03	3.0 ± 0.3	0.10 ± 0.02	0.50 ± 0.05	2.2 ± 0.2	0.23 ± 0.04	0.43 ± 0.08	2.5 ± 0.5	1
Fe _{0.52} Co _{0.48}	0.73 ± 0.05	0.24 ± 0.02	2.1 ± 0.2	0.11 ± 0.02	0.33 ± 0.04	1.7 ± 0.2	0.19 ± 0.03	0.28 ± 0.06	1.9 ± 0.4	0.85
Fe _{0.55} Co _{0.45}	1.17 ± 0.05	0.29 ± 0.03	2.9 ± 0.3	0.10 ± 0.02	0.38 ± 0.04	2.2 ± 0.2	0.17 ± 0.03	0.33 ± 0.07	2.6 ± 0.5	1
Fe	0.79 ± 0.05	0.16 ± 0.02	1.2 ± 0.2	0.13 ± 0.04	-	-	-	0.16 ± 0.02	1.2 ± 0.2	0.85

Table 4.1: Element resolved orbital and spin moments (in units of μ_B/atom) estimated from XAS data acquired along the easy axis ($\theta = 0^\circ$) with $\mu_0 H = 5$ T at 10 K. \bar{L} and \bar{S}_{eff} are the average orbital and effective spin moments per atom in the alloy (see text). The saturation magnetization M_{SAT} and the total magnetization at 5 T M_{5T} are estimated from the magnetization curves in Fig. 4.2. The values for pure Co correspond to one monolayer high Co islands with an average size of 40 atoms and are taken from Ref. 1.

4.1.2 XAS on granular Fe_xCo_{1-x} films

We investigated four different compositions, all of them showing intense dichroic signals and a common out-of-plane easy axis. XAS spectra were acquired at the $L_{2,3}$ edges of Fe and Co. The out-of-plane magnetic moments obtained from sum rule analysis for Fe and Co are summarized in Table 4.1 for the different stoichiometries. For the evaluation of L and S_{eff} , we assumed $h_d = 2.4$ for Co [1] and $h_d = 3.4$ for Fe [15]. This assumption simplifies the comparison of the magnetic moments with previous literature values. The uncertainty on the number of unoccupied $3d$ states can generally be quite large. Variations of the order of 10% can arise from the h_d dependence on the alloy stoichiometry [133] and from the reduced dimensionality [84]. However, first principles electronic structure calculations using the Screened Korringa-Kohn-Rostoker (SKKR) Green's function method for this system give $h_d = 2.3$ for Co and $h_d = 3.4$ for Fe in excellent agreement with the two previous values from the literature [28]. In addition, these values vary by less than 2% with the alloy composition. Therefore we estimate in the present case the uncertainty on h_d to be small, and the error bars for L and S_{eff} have been derived taking into account only the experimental errors.

The orbital moments of Co and Fe show a strong dependence on the alloy stoichiometry. This dependence is even larger when considering the mean orbital moment per alloy atom, defined as

$$\bar{L} = x \cdot L_{Fe} + (1 - x) \cdot L_{Co}. \quad (4.1)$$

\bar{L} has a minimum of $0.16 \pm 0.02 \mu_B/\text{atom}$ for pure Fe and a maximum of $0.43 \pm 0.08 \mu_B/\text{atom}$ for $x = 0.35$. For pure Co $\bar{L} = 0.31 \pm 0.06 \mu_B/\text{atom}$ (see Table 4.1). In contrast, the mean effective spin moment \bar{S}_{eff} , which is defined analog to \bar{L} tends to increase moving from Co to Fe. The only exception is the pure Fe film for which we measure a strongly reduced effective spin moment of $S_{eff} = 1.2 \pm 0.2 \mu_B/\text{atom}$.

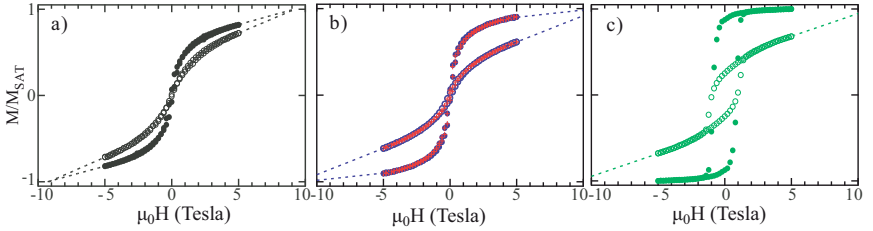


Figure 4.2: Magnetization curves $M_\theta(H)$ of granular films measured at the Fe edge at $T = 10$ K, $\theta = 0^\circ$ (solid circles), and $\theta = 70^\circ$ (open circles), normalized to M_{SAT} (see text). a) $\Theta = 0.79 \pm 0.05$ ML pure Fe; b) $\Theta = 0.73 \pm 0.05$ ML $\text{Fe}_{0.52}\text{Co}_{0.48}$, crosses represent the Co edge data; c) $\Theta = 1.17 \pm 0.05$ ML $\text{Fe}_{0.55}\text{Co}_{0.45}$. Dashed lines are linear extrapolations of the experimental data when saturation is not reached.

The magnetization curves in Fig. 4.2 represent the peak of the Fe (Co) L_3 XMCD intensity at 707.2 (777.3) eV divided by the pre-edge XAS intensity at 704.0 (773.0) eV as a function of the external magnetic field for $\theta = 0^\circ$ and $\theta = 70^\circ$. Normalization to the pre-edge intensity compensates for the angular and field dependence of the total electron yield of the sample, which strongly affect the absolute photocurrent.

The shape of the $M(H)$ curves measured with $\theta = 0^\circ$ and $\theta = 70^\circ$ shows that all the samples exhibit an out-of-plane easy axis. Fig. 4.2 a) and b) show non saturated magnetization curves of pure Fe and $\text{Fe}_{0.52}\text{Co}_{0.48}$ at the maximum available magnetic field of 5 T. In order to estimate the saturated magnetic moment per atom, we linearly extrapolated $M(H)$ above 4 T and defined the intersection point of the magnetization curves measured along the two directions as M_{SAT} . For the non saturated samples we found that the magnetization at $\mu_0H = 5$ T is about 85% of M_{SAT} . Note that the effective spin and orbital moments reported in Table 4.1 are the ones measured at $\mu_0H = 5$ T. In alloy samples we find that the Fe and Co magnetization curves coincide, as expected because of the strong ferromagnetic exchange coupling between the two species (see Fig. 4.2 b)).

It is interesting to compare Fig. 4.2 b) and c), which refer to samples with very similar chemical composition but different coverage. The film with $\Theta = 0.73 \pm 0.05$ ML shows reversible magnetization curves, while the one with $\Theta = 1.17 \pm 0.05$ ML shows hysteresis with a coercive field H_c of about $\mu_0H_c = 1$ T. The origin of this difference resides in the film morphology. As pointed out above, the growth conditions of the granular films are to a good approximation ideal statistical growth with frozen surface diffusion. In this case, island percolation occurs at a coverage of $\Theta \approx 0.9$ ML [134]. In other words, for coverages below this value the film can be considered as an ensemble of monolayer-high magnetically independent particles, while above the film becomes a continuously connected structure.

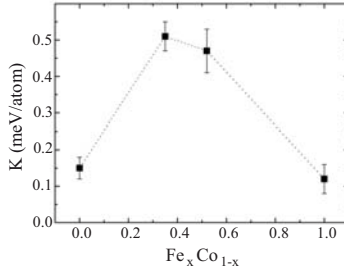


Figure 4.3: MAE *vs.* stoichiometry calculated from Eqs. (4.2) and (4.3). The value for pure Co is taken from Ref. 1 and corresponds to one monolayer thick Co islands with an average size of 40 atoms. The dotted line is a guide to the eye.

Because in ultrathin films with out-of-plane easy axis the critical single-domain diameter is of the order of $1 \mu\text{m}$ [135, 136], one expects that the morphological percolation is accompanied by the onset of irreversible mechanisms of magnetization switching, such as nucleation of reversed domains and domain wall propagation making the interpretation of magnetization curves in terms of anisotropy energies difficult.

The films with coverage below the coalescence threshold have the advantage that the mechanism of magnetization reversal is the rotation of the magnetization vector of each island and therefore one can straightforwardly derive the MAE from the angular dependence of the magnetization curves $M_\theta(H)$ using the following equation:

$$K = \frac{\int_0^{M_{SAT}} \mu_0 H dM_{\theta_1} - \int_0^{M_{SAT}} \mu_0 H dM_{\theta_2}}{\sin^2(\theta_1 - \theta_2)}, \quad (4.2)$$

where $\theta_1 = 0^\circ$ and $\theta_2 = 70^\circ$. M_{SAT} is shown in Table 4.1 as a multiple of M_{5T} , the total magnetic moment estimated at 5 T is

$$M_{5T} = x \cdot (L_{Fe} + (S_{eff})_{Fe}) + (1 - x) \cdot (L_{Co} + (S_{eff})_{Co}) + m_{Pt} \quad (4.3)$$

Equation (4.3) takes into account the orbital and spin moments of Fe and Co, weighted by the film stoichiometry, and the magnetic moment induced in the substrate Pt atoms. Calculations give for the induced moment $m_{Pt} = 0.25 \pm 0.03 \mu_B/\text{atom}$, slightly decreasing when moving from pure Co to pure Fe [28]. These values are consistent with previous studies which found $m_{Pt} \simeq 0.2 \mu_B/\text{atom}$ [129] and $m_{Pt} \simeq 0.27 \mu_B/\text{atom}$ [137] for the induced Pt moment in Co/Pt(111) and Fe/Pt(111), respectively.

A strong dependence of the MAE on the alloy composition is observed in Fig. 4.3. We find a maximum of $K = 0.50 \pm 0.05 \text{ meV}/\text{atom}$ close to the equiatomic stoichiometry. This

value is three to five times the values measured for pure Fe ($K = 0.1 \pm 0.05$ meV/atom) and Co ($K = 0.15 \pm 0.02$ meV/atom) monolayers on Pt(111).

4.1.3 MOKE of continuous $\text{Fe}_x\text{Co}_{1-x}$ films

The magnetization of continuous films deposited at 35 K and annealed at room-temperature was studied by means of *in situ* MOKE. In large islands or continuous films, magnetization reversal does not take place by coherent rotation but by the energetically favored nucleation and growth of reversed domains. Consequently, the measured coercive fields $H_c(T)$ may be orders of magnitude smaller than the values estimated from the MAE assuming coherent magnetization rotation. However, the continuous films investigated here have all similar morphology (see Fig. 4.1). Thus, H_c may be used to monitor relative changes of the MAE as a function of film stoichiometry.

All the measured samples showed square-shaped hysteresis loops for the out-of-plane magnetization measured by polar MOKE (Fig. 4.4 a)). Using transverse MOKE, no in-plane signal was observed within the detection limit. From these observations we deduce an out-of-plane easy axis of magnetization and a single domain remanent state, independent of the film stoichiometry.

The coercive field, measured at $T = 240$ K is shown in Fig. 4.4 b) as a function of stoichiometry of the monolayers. For pure Co ($x = 0$), the coercive field amounts to $\mu_0 H_c = 24.5 \pm 1.5$ mT and for pure Fe ($x = 1$) to 4.5 ± 1.5 mT. Mixing the two elements produces an increase of the switching field up to a maximum of $\mu_0 H_c = 43.5 \pm 1.5$ mT. $H_c(x)$ reaches its the maximum at $x = 0.40$ and its shape as well as the position of maximum H_c are very similar to the one observed for the MAE for granular films.

Magnetization curves at different temperatures for a pure Fe film are shown in Fig. 4.4 c). The coercive field vanishes at 260 K and the loops become s-shaped at 270 K, suggesting the incidence of a magnetic phase transition associated with the Curie temperature, T_C . At T_C the susceptibility $\chi = M/H$ diverges. Therefore T_C can be determined by linearly extrapolating the magnetization curve data represented in an Arrot plot $M^2(H/M)$ to zero [138, 139]. From Fig. 4.4 d) we deduce $T_C = 270 \pm 5$ K for the pure Fe film. For all the other stoichiometries, T_C is above 300 K, but below 400 K which we infer from an extrapolation of the temperature dependence of $H_c(T)$. We already discussed the impossibility to experimentally verify these results because the samples undergo structural changes when annealed to temperatures higher than 320 – 340 K. As expected due to the low dimensionality of the studied films, the measured values of T_C are strongly reduced with respect to the bulk values of 1043 K for Fe and 1388 K for Co [140]. Alloying Fe and Co has been shown to increase T_C [141, 142].

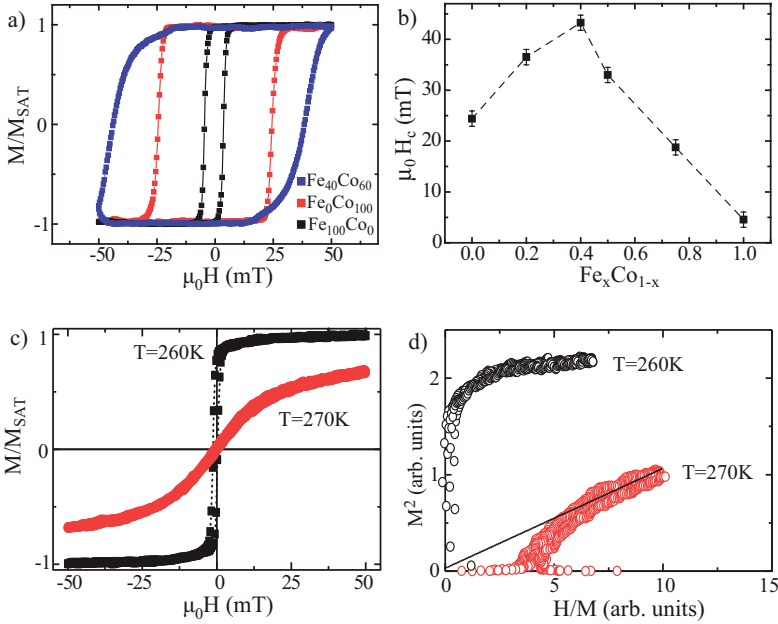


Figure 4.4: a) Polar MOKE magnetization curve recorded at $T = 240$ K for $Fe_{0.40}Co_{0.60}$ -alloy (blue), 1.00 ± 0.05 ML Co (red), and Fe (black). b) Coercive field vs. stoichiometry for 1 ML of Fe_xCo_{1-x} measured along the easy axis at $T = 240$ K. The line is a guide to the eye. c) Polar MOKE magnetization curves recorded at $T = 260$ K and $T = 270$ K for 1.00 ± 0.05 ML Fe deposited at 35 K and annealed at $T = 300$ K. d) Arrot-Kouvel plot for the same sample at $T = 260$ K and $T = 270$ K. The Curie temperature is reached when the linearly extrapolated high-field data intercept the origin (solid line).

4.1.4 Experiment versus theory

In the group of P. Weinberger first principles electronic structure calculations using the Screened Korringa-Kohn-Rostoker (SKKR) Green's function method were performed [143], in order to gain further insight into the magnetic and electronic properties of this system [28]. In this approach a surface is described as a system with two-dimensional translational symmetry which consists in the third direction on one side of a semi-infinite bulk, and of a semi-infinite vacuum region on the other (see Fig. 4.5). The Fe_xCo_{1-x} monolayer has been placed onto positions following the stacking sequence of the Pt(111) surface while using the experimental value of the Pt lattice constant ($a_0 = 3.92$ Å). Due to the

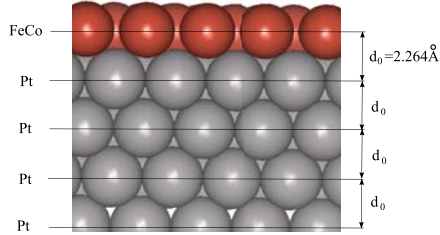


Figure 4.5: Geometry of the system studied by means of SKKR calculations. One monolayer of FeCo with varying composition has been placed on top of an ideal Pt(111) surface. d_0 is the interlayer distance of bulk Pt.

large negative lattice mismatch between the film and the substrate an inward relaxation of the film is expected. For a pseudomorphic Co film on Pt(111) this amounts to -6% assuming that perpendicular stress is absent [144]. For the alloy and Fe films similar or somewhat larger inward relaxation is likely due to the slightly enhanced lattice mismatch. Therefore, the influence of the interlayer spacing between overlayer and substrate on the magnetocrystalline anisotropy energy has been investigated.

Rather good agreement is found for all compositions, apart from clean Fe, between experimental data and theoretical calculations for the magnetic moments. This is surprising when considering that theory treats a perfect monolayer whereas experiment has been performed on granular films. The spin moment (per alloy atom) is predicted by theory to linearly increase from $2.0 \mu_B$ to $3.0 \mu_B$ while moving from pure Co to pure Fe (see Fig. 7 in Ref. 28). XMCD data give an effective spin moment of $S_{eff} = 1.8 \pm 0.1 \mu_B$ for pure Co which increases with increasing Fe content. For $\text{Fe}_{0.55}\text{Co}_{0.45}$ we measure $S_{eff} = 2.6 \pm 0.5 \mu_B$, in coincidence with theory. For comparison we remind the bcc bulk value ($2.3 \mu_B$) [119], the value recently reported for $\text{Fe}_{0.55}\text{Co}_{0.45}/\text{Pt}$ superlattices ($2.5 \mu_B$) [145], and the value for 3D crystalline $\text{Fe}_{0.56}\text{Co}_{0.44}$ nanoparticles ($2.3 \mu_B$) [146] which are all very similar but a significantly smaller one was found for 6 ML thick FeCo films on Rh(100) close to the equiatomic composition ($1.8 \mu_B$) [35]. An evident discrepancy between theory and XMCD data exists in the case of pure Fe for which we measured a strongly reduced effective spin moment of $S_{eff} = 1.2 \pm 0.2 \mu_B$ compared to $S = 3.0 \mu_B$ found by theory. The experimental value is also substantially lower than $S = 2.5 \mu_B/\text{Fe}$ atom reported in FePt nanoparticles [147, 148] and multilayers [149]. Low spin values have been reported for 1 ML of Fe on Cu(111) [150, 151] and on Au(111) [152]. This is probably the consequence of complex magnetic structures, with prevalent antiferromagnetic (AFM) order, characteristic of a thin Fe film with strained fcc structures, as recently observed

for the Fe ML on Ir(111) [153]. Since the lattice constant of Ir and Pt differs by only 2%, and since they are both highly polarizable, it is possible that similar AFM structures also form on the Pt(111) surface. In the calculations ideal flat films pseudomorphic with the Pt(111) surface were assumed and cannot account for such low moment structures. When adding Co atoms, the strong ferromagnetic behavior of Co on Pt(111) and the strong hybridization between Fe and Co restore the ferromagnetic order at the Fe sites.

The orbital moment has in experiment and theory a maximum close to $x = 0.5$. The exact composition where we find this maximum varies slightly between $x = 0.6$ for theory and $x = 0.4$ for experiment. Moreover, theory substantially underestimates L with respect to experiment. This is not surprising because the local density approximation used for the present calculations typically underestimates the orbital magnetic moments of $3d$ metals by about a factor of 2. Arguably, correlation effects may play a prominent role in correctly predicting the magnitude of the orbital polarization [154]. However, the general trend observed as a function of the film stoichiometry should not be affected. Comparing again with the 6 ML thick FeCo films on Rh(100) we note that also in that case a similar behavior for L was observed with a maximum at $x = 0.4$ [35].

The MAE as a function of Fe content has a profile similar to the orbital moment. It shows minima for pure Fe and Co with a maximum value of about $K = 0.5$ meV/atom for a film stoichiometry close to the equiatomic composition. It is worth noting that this value is orders of magnitude enhanced compared with the bcc Fe and hcp Co bulk values of $5 \mu\text{eV/atom}$ and $45 \mu\text{eV/atom}$, respectively [155,156]. The observed bell-shaped behavior as a function of x is very similar to what has recently been predicted and measured in films of a few nanometer thickness [34,118,35]. The experimental and theoretical results demonstrate an out-of-plane MAE for the FeCo films. However, a clear discrepancy exists for the pure Fe film MAE which is found positive (out-of-plane) in the experiments and predicted negative (in-plane) by the calculations. This is predominantly due to the strong in-plane contribution of the Pt substrate found in the calculations and it can be shown that the interlayer relaxation of the Fe film with respect to the Pt(111) substrate is not responsible for the predicted in-plane easy axis [28].

4.1.5 Electronic structure analysis

The bcc FeCo alloy is one of the most studied B2 alloys. Its magnetization as a function of the Co concentration is well described by the Slater-Pauling curve which shows a maximum at about 30% of Co, and then a decrease with further increasing the Co content [119]. This can be understood taking into account that Fe is a weak ferromagnet with the Fermi level intersecting the $3d\uparrow$ and $3d\downarrow$ spin bands, while Co is a strong ferromagnet having holes only in the $3d\downarrow$ band. The strong hybridization of Fe and Co in the alloy produces two concomitant effects. The first is an increase of the Fe exchange

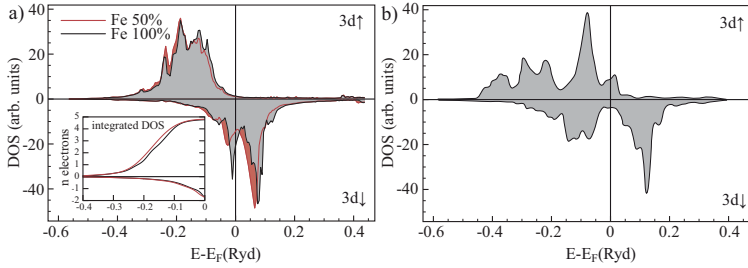


Figure 4.6: a) Calculated Fe DOS for the $\text{Fe}_{0.50}\text{Co}_{0.50}$ and for the pure Fe monolayer films. The inset shows the corresponding integrated DOS (1 Ryd = 13.6 eV). b) DOS for bulk Fe taken from Ref. 159.

splitting relative to pure Fe. The second is that the large Co electron-electron interaction to bandwidth ratio assists and strengthens the weaker Fe electron-electron interaction by saturating the Fe moment. The net result is a redistribution of $3d\downarrow$ electrons to the $3d\uparrow$ states at the Fe sites while adding Co up to a concentration of about 30%. After reaching the maximum magnetization value, the total number of $3d\uparrow$ electrons remains constant, whereas the number of $3d\downarrow$ electrons increases in order to accommodate the additional electrons coming from Co [15, 157, 158, 159].

Our experimental and theoretical data support a different behavior for the $\text{Fe}_x\text{Co}_{1-x}$ monolayer film on Pt(111). Calculations predict a linear decrease of the average spin moment moving from pure Fe to pure Co, as illustrated in Fig. 7 in Ref. 28. The spin-resolved DOS of Fe (Co) demonstrates that the spin-up band is almost completely filled, with 4.8 electrons, while 1.8 (2.9) electrons are localized in the spin-down band, independent of the Co concentration (see inset in Fig. 4.6 a)). Consequently, the spin moment at the Co and Fe sites is composition independent and the alloy magnetization is simply given by the weighted mean of Fe and Co spin moments. This is consistent with the experimental data yielding $S_{eff} = 2.9 \pm 0.3 \mu_B$ for Fe and $S_{eff} = 2.0 \pm 0.2 \mu_B$ for Co with only a slight dependence on the film stoichiometry. The reason of this different behavior with respect to bulk can be easily understood when comparing the d -band of the Fe monolayer with that of bulk Fe shown in Fig. 4.6 b). Two features in the bulk DOS are evident: a small peak at the Fermi energy E_F in the majority states (absent in the film) and a clear peak below the E_F in the minority states (crossing E_F in the film). This strong superposition of minority and majority states is responsible for the reduced spin moment observed in bulk Fe. In the monolayer film, the d -band narrowing due to the reduced symmetry produces a clear splitting of majority and minority states, forcing the Fe to behave as a strong ferromagnet. Adding Co atoms strengthens the d -band narrowing, as shown in

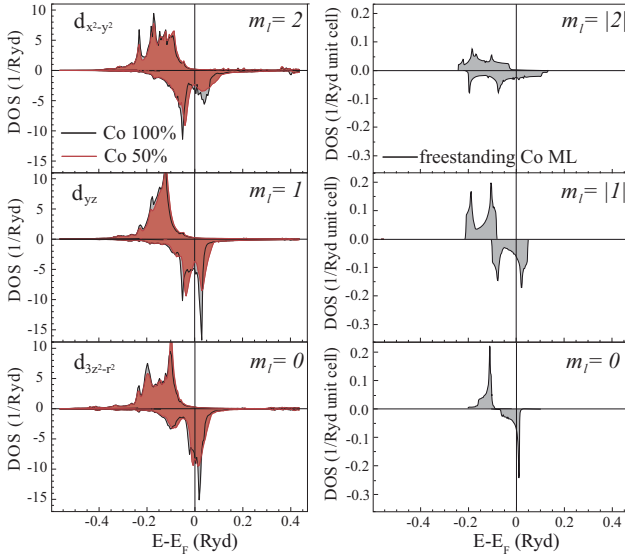


Figure 4.7: Left: Orbital resolved Co DOS calculated for an $\text{Fe}_{0.5}\text{Co}_{0.5}$ and for a pure Co monolayer film. Right: Orbital resolved DOS for the free standing Co monolayer taken from Ref. 162.

Fig. 4.6 a) by comparing the DOS of pure Fe and $\text{Fe}_{0.5}\text{Co}_{0.5}$ films. However, since the Fe spin moment is already close to the maximum value due to a completely filled $3d\uparrow$ shell, adding Co atoms plays only a minor role.

Let us now consider what happens for the orbital moment L and the MAE, related to L via the spin-orbit interaction. In bulk, the high symmetry of the bcc structure strongly quenches L with the consequence that also the MAE is close to zero. Large MAE values can only be observed in highly strained bct structures which destroy the translational symmetry of the bcc structure. The unquenched orbital moment, due to the reduced symmetry, is accompanied by an anisotropy of the orbital moment itself which in turn generates a large value of the MAE via the spin-orbit coupling. In particular for bulk FeCo alloys it has been shown that a tetragonal distortion of the bcc structure produces a reduction of the energy difference between occupied and unoccupied states [34]. Because in second order perturbation theory the MAE is inversely proportional to the energy separation between occupied and unoccupied states [160, 20, 161], a strong MAE is predicted and experimentally observed for the c/a ratio minimizing this energy separation [34, 35].

This picture changes completely when considering a single $\text{Fe}_x\text{Co}_{1-x}$ layer on the

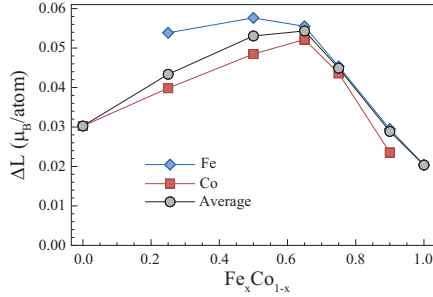


Figure 4.8: Anisotropy of the orbital moment as a function of x . Lines are guides for the eye.

Pt(111) surface. In this case, the c/a ratio is not even defined. The symmetry breaking arises from coordination reduction, strain due to lattice mismatch between monolayer and substrate, and electronic hybridization with the substrate. The effect of the electronic hybridization with the substrate can be qualitatively understood by comparing each of the five orbital resolved DOS calculated for the Co/Pt(111) monolayer film (Fig. 4.7 and Fig. 12 in Ref.28) with the equivalent calculated for the free-standing Co monolayer. The most visible difference concerns the DOS widths of the two systems. For $m_l = \pm 2$ the DOS widths are very similar, while for $m_l = \pm 1$ and $m_l = 0$ the DOS widths are about 0.2 Ryd and 0.3 Ryd, respectively, larger in the Pt(111) supported Co monolayer. In the independent electron ligand field picture a larger DOS width implies stronger electronic hybridization or bonding with the neighboring atoms [161]. Because orbitals with $m_l = 0$ ($d_{3z^2-r^2}$) and $m_l = \pm 1$ (d_{xz}, d_{yz}) describe out-of-plane bonding, while orbitals with $m_l = \pm 2$ ($d_{x^2-y^2}, d_{xy}$) describe in-plane bonding, the previous observation on the DOS widths immediately highlights the formation of a vertical Co-Pt bonding and a substantially unmodified in-plane Co-Co bonding. In the same ligand field picture, the formation of a strong directional bonding generates a reduction of the component of the orbital moment perpendicular to the bonding direction. In our case, this implies a strong reduction of the in-plane component of the orbital moment in the Co/Pt(111) monolayer in comparison with the free-standing monolayer. Coherently, our experimental data show highly unquenched orbital atomic moments of $L = 0.31 \pm 0.06 \mu_B$ and $L = 0.16 \pm 0.02 \mu_B$ for pure Co and Fe, respectively, with larger values for the out-of-plane direction.

A second strong hybridization is found between Fe and Co atoms when they are mixed in the alloy. Because the Co DOS is narrower than the Fe DOS, increasing the Fe percentage in the alloy leads to the spreading of Co and Fe DOS (Fig. 13 in Ref. 28). However, the orbital resolved DOS for Co are always narrower than the corresponding

one for Fe. In the ligand field picture this implies larger L values for Co than for Fe, in agreement with the experiment.

The Fe-Co hybridization is also responsible for the observed composition dependence of the MAE. To highlight this point, the anisotropy of the orbital moment ($\Delta L = L_{M\perp} - L_{M\parallel}$) is computed and presented in Fig. 4.8. $L_{M\perp}$ is the orbital moment calculated for the magnetization oriented out-of-plane and $L_{M\parallel}$ the one for in-plane magnetization. The resulting curves clearly suggest that the maximum of the orbital moment anisotropy occurs at equiatomic composition. According to the Bruno and van der Laan model the MAE is directly linked to ΔL and we can argue that also the maximum MAE has to be observed for the same composition [21, 20]. Orbital resolved DOS show that the ΔL (MAE) behavior is a strict consequence of a fine tuning in the occupation of the minority $3d\downarrow$ orbitals (see Fig. 14 in Ref. 28).

4.2 Fe and Co on Rh(111)

For synchrotron experiments the Rh(111) substrate was prepared by repeated cycles of Ar-ion sputtering (1.3 keV at 300 K), followed by annealing at 800 K in an oxygen atmosphere of $P_{O_2} = 5 \times 10^{-8}$ mbar and final annealing at 1000 K. Surface cleanliness was confirmed by Auger electron spectroscopy and XAS. Co and Fe were deposited by molecular beam epitaxy from high purity rods (99.995%) at a sample temperature of 10 K. Low temperature deposition, where diffusion is inhibited, leads to granular films as discussed in section 4.1.1. During deposition the pressure inside the UHV chamber was below 1×10^{-10} mbar. The deposition rate determined by STM and XAS was 0.10 ± 0.01 ML/min for Co and Fe.

MOKE and STM measurements were carried out, using the experimental setup described in chapter 5. The Rh(111) crystal was prepared for the MOKE and STM experiments in a similar way as for the synchrotron experiments with the only difference of a final annealing up to $T = 1400$ K. Two different types of films were grown for MOKE experiments: granular and continuous films. The deposition rate was the same as in the synchrotron experiments and the pressure during deposition was $P < 2 \times 10^{-10}$ mbar. Granular films were deposited at $T = 60$ K and continuous films were grown in a temperature range between 50 K and 95 K followed by annealing at $T = 300$ K for 5 min. Polar and transverse MOKE were measured at different temperatures and the morphology of the film was determined using STM. Note that in the given deposition temperature range from 50 K to 95 K no difference in final film morphology and magnetic properties was found.

4.2.1 XAS and XMCD study of 1 ML thick granular films

We investigated the magnetic and electronic properties of granular films and the substrate by taking XAS at the $L_{2,3}$ edges of Fe and Co and the $M_{2,3}$ edges of the Rh(111) substrate. The orbital moment L and effective spin magnetic moment $S_{eff} = S + 7D$ of Fe and Co, respectively, were determined along the easy magnetization axis of the saturated sample using the sum rules given in equations (2.18) and (2.19). Out-of-plane *vs.* in-plane magnetic behavior was investigated by recording hysteresis curves at $\theta = 0^\circ$ and 70° .

Magnetic Moments of Fe and Co

The results obtained on the system 0.80 ± 0.08 ML Fe/Rh(111) are reported in Fig. 4.9. From the hysteresis curves shown in b) we infer the easy axis of magnetization along the surface normal and note that saturation is reached at both angles. By applying the sum rules to the XAS and XMCD spectra measured at the Fe $L_{2,3}$ edges along the easy axis we obtain with $h_d = 3.9$, the number of d -holes from our calculation [121], $L = 0.21 \pm 0.04 \mu_B$ and $S + 7D_{0^\circ} = 2.89 \pm 0.12 \mu_B$. In case of uniaxial anisotropy, angle-dependent XMCD measurements allow the separation of the magnetic spin dipole moment D_θ and S for fully magnetized samples [16]. S is angle independent while D_θ varies as

$$D_\theta = D_{0^\circ}(\cos^2 \theta - \frac{1}{2} \sin^2 \theta). \quad (4.4)$$

The measurement at $\theta = 70^\circ$ yields $S + 7D_{70^\circ} = 2.71 \pm 0.12 \mu_B$ resulting in a spin magnetic moment of $S = 2.76 \pm 0.16 \mu_B$ and $7D_{0^\circ}/S = 0.05$, in very good agreement with Ref. 84.

1.25 ± 0.13 ML Co/Rh(111) has its easy axis in-plane according to the magnetization loop shown in Fig. 4.10 b). XAS taken at the Co $L_{2,3}$ edges at $\theta = 70^\circ$, the resulting XMCD spectrum, and the corresponding integral are shown in a). From the sum rules we obtain with $h_d = 2.8$ from our calculation $L = 0.34 \pm 0.06 \mu_B$ and $S + 7D = 2.07 \pm 0.08 \mu_B$. Unfortunately, the spin magnetic moment cannot be separated from the dipole moment in this case because the hard axis magnetization curve is far from saturation. Assuming $7D/S = 0.05$ as in the case of Fe, we obtain with this correction $S = 1.99 \pm 0.08 \mu_B$. Earlier DFT calculations yield a magnetic moment in the Co adlayer of $1.95 \mu_B$ which is in very good agreement with our experimental results [163].

Induced polarization

The Rh surface is known to be very close to the onset of ferromagnetism and hence large induced magnetic Rh moments can be observed by the presence of a magnetic atom [40, 41, 42, 164]. In order to investigate possible substrate magnetization and its effect on the magnetism of the deposited thin film, we compared XAS acquired on the clean and on the covered surface. We measured the $M_{2,3}$ absorption edges at $T = 10$ K

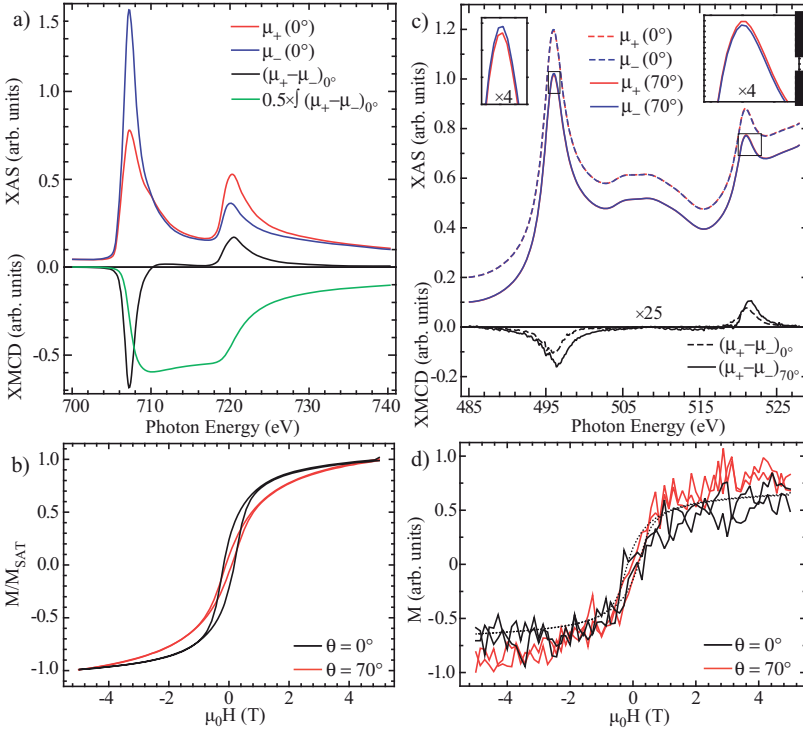


Figure 4.9: 0.80 ± 0.08 ML Fe/Rh(111) measured at $T = 10$ K. a) XAS, resulting XMCD ($\mu_+ - \mu_-$) spectrum, and integrated XMCD spectrum taken at the Fe $L_{2,3}$ edges at $\mu_0 H = 5$ T. b) Magnetization curves at 0° and 70° measured by taking the peak of the L_3 XMCD intensity at 777.1 eV divided by the pre-edge intensity at 704.0 eV as a function of the applied magnetic field. c) XAS and resulting XMCD spectra with a $\times 25$ magnification measured at the Rh $M_{2,3}$ edges for 0.56 ML Fe coverage at $\mu_0 H = 5$ T. The spectra at 70° have been normalized to the pre-edge M_3 intensity and offset for clarity. d) Magnetization curves measured at the Rh edge for 0° and 70° by taking the peak of the M_3 XMCD intensity at 496.2 eV divided by the pre-edge intensity at 491.0 eV as a function of H . The dotted line represents the scaled magnetization curve for the Fe adlayer taken at $\theta = 0^\circ$.

with $\mu_0 H = \pm 5$ T of the clean Rh(111) substrate and observe no magnetic polarization. We took special care to average over a large number of absorption spectra (minimum 10)

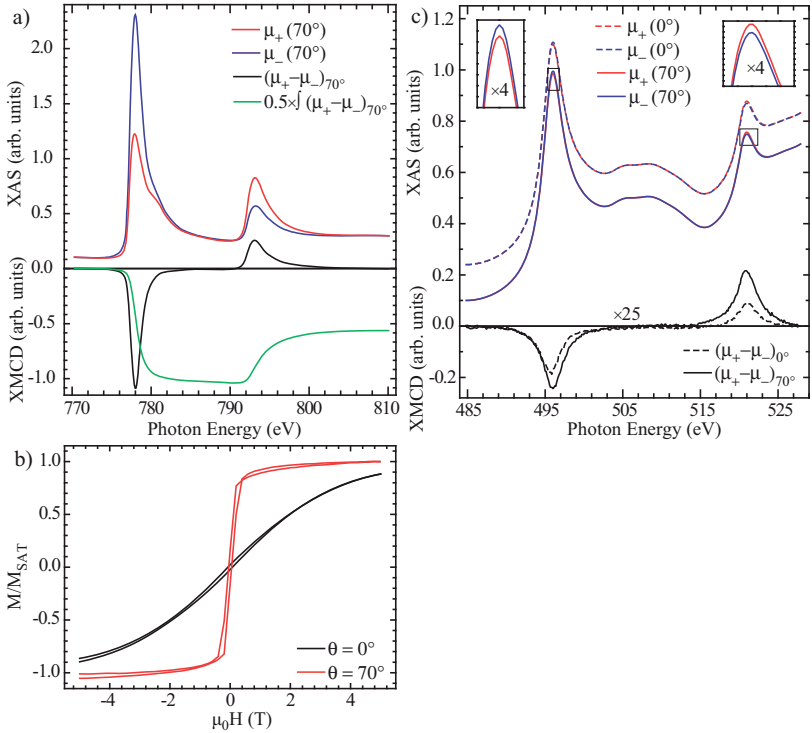


Figure 4.10: 1.25 ± 0.13 ML Co/Rh(111) measured at $T = 10$ K. a) XAS, resulting XMCD spectrum, and the integrated XMCD spectrum taken at Co $L_{2,3}$ edges at $\mu_0 H = 5$ T. b) Magnetization curves for $\theta = 0^\circ$ and 70° measured by taking the peak of the L_3 XMCD intensity at 777.0 eV divided by the pre-edge intensity at 774.5 eV as a function of the external field. c) XAS and resulting XMCD spectra shown with a $\times 25$ magnification measured at the Rh $M_{2,3}$ edges across 1.25 ML Co. The spectra at 70° have been normalized to the pre-edge M_3 intensity and offset for clarity.

to improve the signal to noise ratio. XAS recorded after Fe deposition are displayed in Fig. 4.9 c). A zoom in the absorption intensities (see insets) evidences a small difference for XAS acquired with positive and negative x-ray helicity. The corresponding XMCD signal is shown with a $\times 25$ magnification. By comparing the sign of the L_3 dichroism of Rh and Fe we conclude that the Rh moments are ferromagnetically aligned with the Fe moments. Unfortunately, we cannot apply the sum rules to calculate the Rh moments for

two main reasons: *i*) we have to deal with the difficulty that the x-ray absorption intensity integrates over several Rh layers of which only a part carries a magnetic moment and *ii*) saturation effects which are important for bulk samples [165]. Saturation effects arise when the x-ray penetration depth λ_x becomes comparable to the electron escape depth which is about 20 Å. At the $L_{2,3}$ absorption edges of 3d metals λ_x is only 200 Å which efficiently reduces the incident x-ray intensity at sampling depth contributing to the total electron yield (TEY). Consequently, the TEY does not reflect the true x-ray absorption coefficient. Moreover, the x-ray penetration depth depends on the incidence angle making the XAS taken at grazing incidence ($\theta = 70^\circ$) more sensitive to the surface layers than XAS taken at normal incidence ($\theta = 0^\circ$). Thus, the larger XMCD signal obtained for grazing incidence is due to an increased sensitivity to the induced Rh magnetization being limited to a few Rh layers close to the interface. Despite the small XMCD signal we managed taking magnetization curves of the Rh substrate as shown in Fig. 4.9 d). The dotted line represents the scaled magnetization curve for the Fe adlayer taken at $\theta = 0^\circ$ indicating a coherent switching behavior for film and substrate.

Equally, we measured XAS of the Rh $M_{2,3}$ edges buried under a Co monolayer as shown in Fig. 4.10 c). The small difference of the XAS acquired with μ_+ and μ_- is pointed out in the insets. Consequently, the resulting XMCD spectrum is shown with a $\times 25$ magnification. Again Co and Rh moments are ferromagnetically aligned as we conclude from the sign of the XMCD spectra of Co and Rh. Saturation effects impede an estimation of the Rh magnetic moment as discussed above.

When comparing the magnitude of the M_3 XMCD signal for Rh covered with Fe respectively Co, we remark a larger amplitude for Co. At normal (grazing) incidence the XMCD signal is about 0.4% (0.7%) with respect to the XAS intensity for Fe coverage and 0.8% (1.1%) for Co coverage. This may be due to a difference in coverage (0.56 ML for Fe and 1.25 ML for Co) or a truly larger induced moment in case of the Co adlayer. Assuming that only Rh atoms in direct contact with the Fe respectively Co atoms get polarized and that the induced moment is the same for Fe and Co, we expect a polarization ratio of 0.56 between Fe and Co. This is in good agreement with a polarization ratio of 0.50 at 0° and 0.64 at 70° . However, we did not take magnetization curves at the Rh edge of the Co covered sample and therefore miss the information if we reach saturation or not and if the switching behavior of the magnetic film and substrate are the same. Hence, the induced magnetization may be underestimated. This is supported by the calculations predicting an induced magnetic moment in the topmost Rh layer of $0.17 \mu_B/\text{Fe}$ atom and $0.53 \mu_B/\text{Co}$ atom (see table 4.2).

Magnetic anisotropy

The MAE can be calculated from the saturated magnetization curves using equation (4.2). The total magnetic moment to be reversed is $S + L + m_{Rh}$, where m_{Rh} represents the

magnetic moment induced on Rh sites per Fe or Co atom. Since m_{Rh} is not known experimentally, we will calculate the lower bound of the MAE using $m_{Rh} = 0$.

For Fe we reach saturation for both angles (see Fig. 4.9 b)) we can readily calculate the MAE and we obtain $K \geq 0.08 \pm 0.01$ meV/Fe atom. Using second order perturbation theory Bruno proposed an equation linking the anisotropy energy directly to the anisotropy of the orbital moment $\Delta L = (L_{0^\circ} - L_{90^\circ})$ [21]

$$K = -\frac{G}{H} \frac{\xi}{4\mu_B} \Delta L. \quad (4.5)$$

The factor G/H depends on the band structure and a rough estimate for transition metals is 0.2, due to the usually smaller d bandwidth compared with the exchange splitting [16]. This is in good agreement with $G/H = 0.23 \pm 0.02$ deduced from comparison of the MAE obtained with MOKE and the anisotropy of the orbital moment obtained with XMCD for a superlattice of Co islands on Au(788) [22]. ξ is the spin orbit coupling constant, being about 50 meV [46, 21]. L_{90° can be calculated using $L_\theta = L_{0^\circ} \cos^2 \theta + L_{90^\circ} \sin^2 \theta$. Hence, we deduce $K = 0.15 \pm 0.03$ meV/Fe atom. Note that the Bruno model was derived for fully occupied majority states. However, Fe has some majority d -holes which cause to overestimate the MAE using Bruno's formula [56, 20, 55].

The magnetization curves used to calculate the MAE for Co are shown in Fig. 4.10 b). For $\theta = 70^\circ$ the shape is nearly square suggesting the easy magnetization axis is in-plane. Equation (4.2) yields $K > 0.31$ meV/Co atom after extrapolation of the hard axis magnetization curve to saturation. S. Dennler *et al.* [163] calculate an induced moment of $0.4 \mu_B$ in the topmost Rh layer adding 0.06 meV/Co atom to the MAE which finally results to $K = 0.37 \pm 0.05$ meV/Co atom.

4.2.2 MOKE of granular and continuous films

We investigated granular and continuous films of one atomic layer Fe or Co with MOKE in polar and transverse geometry to probe out-of-plane *vs.* in-plane magnetic behavior as a function of the morphology. The granular films consist of clusters of mostly single atomic height with a large size distribution [28]. For a coverage of 0.90 ± 0.05 ML deposited at $T = 60$ K we infer from STM images for Fe and Co a mean island size of 70 atoms; less than 0.03 ML are found in the second layer (see for example Fig. 4.12). For granular Fe films measured at $T = 45$ K we observe a straight line for polar Kerr and no signal for transverse Kerr (not shown) typical for super-paramagnetic Fe clusters above the blocking temperature. Annealing at $T = 300$ K for 5 min leads to a continuous film with large ferromagnetic domains. We observe an s-shaped hysteresis loop for polar Kerr shown in Fig. 4.11 a) with a coercive field of $\mu_0 H_c = 20 \pm 2$ mT and no transverse Kerr signal as shown in Fig. 4.11 b). Note that the maximum field amplitude of 312 mT is not sufficient to fully saturate the sample in the easy direction. The STM image of

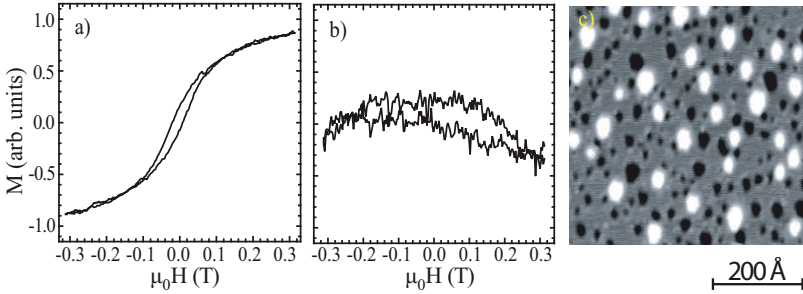


Figure 4.11: 1.00 ± 0.05 ML Fe/Rh(111) deposited at $T = 53$ K and annealed at 300 K for 5 min. a) Polar and b) transverse MOKE measured at $T = 65$ K. c) STM image measured at $T = 65$ K; $V_t = -0.1$ V, $I_t = 5$ nA.

1.00 ± 0.05 ML Fe/Rh(111) is shown in Fig. 4.11 c). For Fe/Rh(111) the lattice mismatch is -7.5% . However, we did not find partial dislocation lines characteristic for surface stress relaxation and thus assume pseudomorphic growth for the Fe monolayer as already observed for Fe/Pt(111).

Granular Co films have a polar and transverse signal similar to the continuous film as shown in Fig. 4.12 a) and b). The square hysteresis loop of 1.00 ± 0.05 ML Co/Rh(111) taken in transverse geometry evidences an in-plane easy magnetization axis. The coercive field is $\mu_0 H_c = 7 \pm 1$ mT. An STM image of the continuous film is shown in Fig. 4.12 b). Differently from Fe, the Co film (lattice mismatch -6.6%) relaxes and the typical partial dislocation lines or domain walls separating hcp and fcc stacking regions can be observed in the topograph. The structural properties of the Fe and Co films on Rh(111) are similar to those of Fe and Co on Pt(111) as discussed earlier. However, the magnetic properties are different. Co/Rh(111) has an in-plane easy axis whereas Co/Pt(111) has an out-of-plane easy axis.

4.2.3 Experimental results of Co and Fe multi-layers

We investigated the evolution of the magnetic properties as a function of the film thickness. Fe films have an out-of-plane easy axis up to 4 ML which turns completely in-plane for 6 ML due to the dipolar term dominating the perpendicular MAE (see Fig. 4.13).

Continuous Co films of 1.8 ± 0.1 ML and 2.7 ± 0.15 ML thickness are presented in Fig. 4.12 c) and d). In the second layer the surface relaxation appears as surface partial dislocation similar to the observation in the first layer. In the third layer a trigonal dislocation network can be observed which remembers 2 ML Cu/Pt(111) [166, 167, 122] or 4 ML Cu/Ru(0001) [168]. Polar and transverse Kerr results evidence a double spin

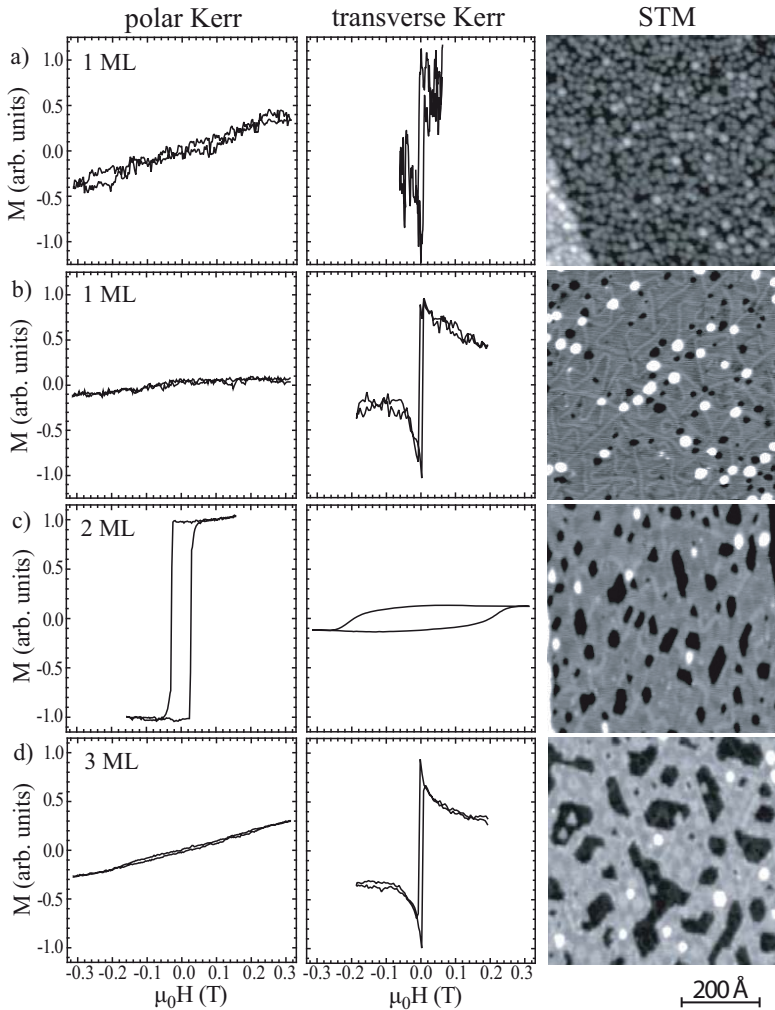


Figure 4.12: Polar Kerr, transverse Kerr, and STM measurements of ultra-thin Co films on Rh(111) of varying thickness. a) 0.90 ± 0.05 ML Co/Rh(111) deposited and measured at $T = 60$ K. STM image: $V_t = -0.05$ V, $I_t = 0.3$ nA. b) - d) successive Co deposition at $T = 60$ K followed by annealing at $T = 300$ K for 5 min in steps of 1 ML. All measurements are performed at $T = 60$ K. b) 1.00 ± 0.05 ML; $V_t = -0.8$ V, $I_t = 5$ nA c) 1.8 ± 0.1 ML; $V_t = -0.01$ V, $I_t = 2$ nA d) 2.7 ± 0.15 ML; $V_t = -0.01$ V, $I_t = 1$ nA.

reorientation transition as a function of film thickness. The easy axis turns from in-plane for 1 ML to out-of-plane for 2 ML and back to in-plane for ≥ 3 ML. The same behavior was reported for Co/Ru(0001) [26, 169]. The authors explain the magnetization reversal from in-plane for 1 ML to out-of-plane for 2 ML by a structural transition from laterally strained, pseudomorphic 1 ML thick films to relaxed 2 ML thick films and a consequent increase in band energy outbalancing the dipolar term. The in-plane lattice constant of the topmost layer is for 1 ML Co/Ru(0001) 2.70 Å and for 2 ML Co/Ru(0001) 2.56 ± 0.08 Å. However, a full monolayer of Co on Rh(111) relaxes as evidenced by surface partial dislocations visible in the STM topograph, invalidating the argument presented in Ref. 26 for our case. For 3 ML El Gabaly *et al.* find that the dipolar term dominates favoring the in-plane orientation of the magnetization. Note that Rh(111) and Ru(0001) have almost the same in-plane lattice constant (2.69 Å for Rh and 2.70 Å for Ru).

4.2.4 MOKE of continuous $\text{Fe}_x\text{Co}_{1-x}$ monolayer films on Rh(111)

Preliminary MOKE measurements of $\text{Fe}_x\text{Co}_{1-x}$ monolayer films on Rh(111) evidence a strong increase in T_C and H_c measured at $T = 65$ K for $x = 0.5$ with respect to pure Fe where $T_C = 90 \pm 10$ K and $H_c = 20 \pm 2$ mT were obtained. For the equiatomic composition we found $T_C = 225 \pm 5$ K and $H_c = 190 \pm 2$ mT. As we already argued in the case of $\text{Fe}_x\text{Co}_{1-x}$ ML films on Pt(111), H_c may be used to monitor relative changes of the MAE at equal film morphology. Consequently, we expect an increased MAE for $\text{Fe}_{0.5}\text{Co}_{0.5}/\text{Rh}(111)$ compared with pure iron. Further, we note a perpendicular easy axis for an Fe content as small as $x = 0.13$ which is astonishing considering that pure Co ($x = 0$) has an in-plane easy axis.

4.2.5 Experiment versus theory

Inspired by our measurements S. Drenner and J. Hafner investigated the magnetic properties of Fe and Co monolayers on Rh(111) using density-functional theory implementing the exchange correlation functional in form of the generalized gradient approximation (GGA). The GGA method yields the lattice constants of Fe, Co, and Rh in very good agreement with experiment [163, 170]. The system is modelled by a (1×1) in-plane periodic slab with a thickness of 11 Rh layers. The 7 bottom layers are fixed in bulklike positions whereas the upper 4 layers are allowed to relax. This relaxation process reduces the interlayer distance of the magnetic adlayer and the topmost Rh layer. Preliminary results for fully relaxed hcp Fe and Co films are summarized in table 4.2. We find the calculated spin magnetic moment of $2.8 \mu_B/\text{Fe}$ atom and $2.0 \mu_B/\text{Co}$ atom identical to the experimental ones. Also the tendency of a larger L respectively L/S for Co is well reproduced. However, the absolute size of L is underestimated by about a factor of 2.5.

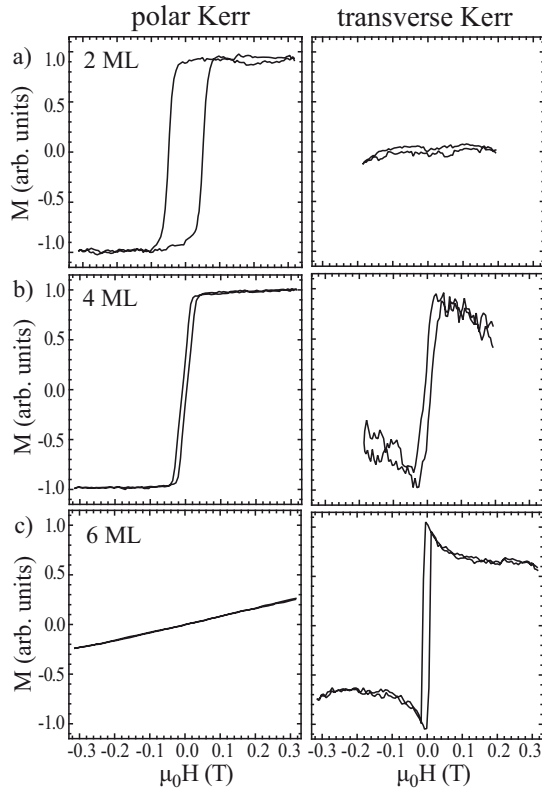


Figure 4.13: Polar Kerr and transverse Kerr measurements of ultra-thin Fe films on Rh(111) of varying thickness at $T = 80$ K. The films were produced by depositing successively 1.00 ± 0.10 ML at $T = 95$ K followed by annealing at $T = 300$ K for 5 min. a) 2.00 ± 0.20 M, b) 4.00 ± 0.40 ML, c) 6.00 ± 0.60 ML.

A clear discrepancy is found for the easy axis in case of Co, which is found in-plane experimentally and predicted out-of-plane theoretically. Note that the dipolar contribution which favors an in-plane orientation was not included.

	L	S	L/S	L_{sub}	S_{sub}	m_{sub}	K	easy axis
hcp Fe/Rh(111)	0.09	2.83	0.03	0.004	0.17	0.17	0.07	↑
hcp Co/Rh(111)	0.12	1.96	0.06	0.021	0.51	0.53	0.22	↑
hcp Fe/Pt(111)	0.10	3.00	0.03	0.066	0.30	0.37	4.32	↑
hcp Co/Pt(111)	0.12	2.02	0.06	0.084	0.36	0.44	0.90	↑

Table 4.2: Calculated magnetic properties. Orbital and spin moments are given in units of μ_B /atom. L_{sub} , S_{sub} , and m_{sub} are the orbital moment, spin moment, and total moment of the topmost substrate layer. The magnetic anisotropy energy is the difference in total energy for out-of-plane and in-plane orientation and given in meV/adatom. ↑ stands for out-of-plane easy axis. The hcp structure was found to be slightly more stable than the fcc structure for Co/Rh(111) [163].

4.3 Conclusions

We characterized the magnetic properties of pure Fe and Co as well as $\text{Fe}_x\text{Co}_{1-x}$ monolayer films on Pt(111) and Rh(111). The orbital and spin magnetic moments as well as the anisotropy energies per magnetic adatom are summarized in table 4.3. For Fe/Pt(111) we found a reduced spin moment of $1.2 \pm 0.2 \mu_B$ /atom which was explained by a probably complex magnetic structure with prevalent antiferromagnetic order as recently observed for one monolayer Fe/Ir(111) [153]. On the contrary, the spin moment for 1 ML Fe/Rh(111) is $S = 2.8 \pm 0.2 \mu_B$ /atom suggesting that the Fe film orders ferromagnetically. Note that in a very recent publication a ferromagnetic ground state was predicted for 1 ML Fe/Pt(111) and a double-row AFM structure for 1 ML Fe/Rh(111) [171]. The orbital and spin moments in the Co adlayer are the same within the error bar for both substrates (see table 4.3). Remember that we used two different values of h_d for Co/Rh(111) ($h_d = 2.3$) and Co/Pt(111) ($h_d = 2.8$) as suggested by the calculations. Further, we observe that L/S_{eff} is smaller for Fe than for Co as predicted by calculations in table 4.2 and previously found for single Fe and Co atoms on Rh(111), Pd(111), and Pt(111) (see section 3.1). However, in case of Fe the L/S_{eff} ratio of single atoms and monolayer films is comparable, while for Co the L/S_{eff} ratio is reduced by a factor of 4 when comparing single atoms and monolayer films. The decrease of L/S_{eff} with an increasing coordination number is a consequence of the quenching of the orbital moment while S_{eff} is almost unaffected [1]. The different behavior of L/S_{eff} as a function of Θ for Fe and Co may be explained by combining structural and electronic information. The calculations find a stronger hybridization of Fe with the underlying Pt than for Co with Pt which comes along with a larger DOS and a smaller orbital moment for Fe. Further we found that Fe tends to grow pseudomorphic while the Co film relaxes. The pseudomorphic growth of

	L	S_{eff}	L/S_{eff}	m_{sub}	K	easy axis
Fe/Rh(111)	0.21 ± 0.04	2.8 ± 0.2	0.07 ± 0.03	0.17^a	0.10 ± 0.05	\uparrow
Fe/Pt(111)	0.14 ± 0.02	1.2 ± 0.2	0.13 ± 0.04	$0.22^b/0.37^a$	0.12 ± 0.03	\uparrow
Fe bcc	0.09 ± 0.01	2.0 ± 0.1	0.04 ± 0.01	-	0.005	[100]
Co/Rh(111)	0.34 ± 0.06	2.1 ± 0.1	0.16 ± 0.02	0.53^a	0.31 ± 0.03	\rightarrow
Co/Pt(111)	0.31 ± 0.06	1.8 ± 0.1	0.17 ± 0.02	$0.28^b/0.44^a$	0.15 ± 0.02	\uparrow
Co hcp	0.15 ± 0.01	1.6 ± 0.1	0.09 ± 0.01	-	0.045	c-axis

Table 4.3: Orbital and spin moments (in units of μ_B/atom) of monolayer films estimated from XAS data acquired along the easy axis (\uparrow stands for out-of-plane and \rightarrow for in-plane) with $\mu_0 H = 5$ T. m_{sub} (in units of μ_B/atom) is the total magnetic moment of the topmost substrate layer from the calculations. a is taken for table 4.2 and b from Ref. [28]. The magnetic anisotropy energy is given in meV/adatom. For Fe and Co bulk L , S_{eff} , and L/S_{eff} are taken from Ref. 15 and the MAE from the Refs. 155, 156.

Fe implies that the distance between Fe atoms is stretched by 11.5% on top of Pt and by 8.1% on Rh resulting in a reduced overlapping of the atomic wave functions compared with bulk Fe. Further, lateral tensile strain usually goes with an inward relaxation of the adlayer leading to a strong hybridization of the Fe 3d orbitals with the d orbitals of the substrate which quenches the orbital moments almost as efficient as in bulk Fe [144, 31]. For Co the lattice mismatch is naturally smaller compared with Fe (9.4% for Co/Pt(111) and 6.6% for Co/Rh(111)), hence the distance between Co atoms is stretched by 10.4% on top of Pt and by 7.1% on Rh. In addition, part of the lateral stress is released, meaning that the Co-Co interaction is strengthened. These findings suggest that the magnetic properties of Fe are mainly governed by the Fe-substrate interactions while those of Co depend on a fine interplay between Co-substrate and Co-Co interactions.

Concerning the MAE we observe that Fe is less anisotropic compared to Co. This is coherent with Fe and Co bulk in their stable crystallographic phases (5 μ eV for bcc Fe respectively 45 μ eV for hcp Co) and surface supported single Fe and Co atoms (see section 3.1). It is interesting to note that the MAE of Fe on Rh(111) and Pt(111) is comparable in value and sign, while Co/Rh(111) has a large in-plane anisotropy and Co/Pt(111) has half as large out-of-plane MAE. The magnitude of the MAE may be correlated with the induced magnetic moment of the topmost Rh(111) respective Pt(111) surface layer. From table 4.3 we clearly see that the MAE is proportional to m_{sub} suggesting that the induced magnetic moment substantially contributes to the MAE. In a recent theoretical investigation of Fe impurities on Pd(001), J. Hafner *et al.* conclude that the large MAE is mainly caused by the anisotropy of the induced spin and orbital Pd moments [31]. We note that the finding of a large anisotropy of the induced moment requires an initially

large induced moment.

For bimetallic $\text{Fe}_x\text{Co}_{1-x}$ alloys on Pt(111) a bell-shaped curve with a maximum MAE of $K = 0.5$ meV/atom was found for the equiatomic composition while the saturation magnetization increases monotonically from $2 \mu_B$ to $3 \mu_B$ going from Co to Fe. We conclude that these systems are good candidates to design new materials with large M_{SAT} and K . For example, regarding applications we find that a single island of only 2400 atoms FeCo/Pt(111) meets the stability criterion of 1.2 eV/bit while the writing field K/M_{SAT} remains in the technological limit [172]. This results in a storage density of about 2.5 Tbits/inch² assuming that half of the surface is occupied with magnetic islands. Further, it has been shown that covering Co islands on Pt(111) with Pd increases the blocking temperature which is linked to the MAE and in turn allows a further size reduction of the islands [30].

Chapter 5

Magneto - Optical Kerr Effect

In this chapter a historical outline of the Faraday and Kerr effect will be given (see section 5.1), followed by a detailed theoretical description of the magneto-optical Kerr effect (MOKE) of magnetic multilayers in section 5.2. In the thin film limit (see section 5.2.1) we give an improved linear approximation of the Fresnel coefficients being in very good agreement with the numerical solution. Section 5.3 is dedicated to our home-built MOKE setup having the optics inside the UHV chamber, and section 5.4 presents the first measurements with this new setup on Co/Rh(111) and Co/Au(11,12,12) demonstrating the versatility and high sensitivity of the UHV-MOKE.

5.1 Historical Introduction

The magneto-optical Kerr effect (MOKE) has been discovered by the Scottish physicist John Kerr in 1876 observing that the state of polarization of linearly polarized light changes upon reflection at a polished pole of an electromagnet [173,174]. Today, MOKE or also called SMOKE (surface magneto-optical Kerr effect) is a common tool to investigate magnetic multilayers, thin films, and nanostructures at surfaces triggered by advances in thin film growth and nanopatterning. A large driving force of this research field is the request of ever-increasing bit density on magnetic hard disks which requires at the same time an increasing sensitivity of experimental techniques giving access to the properties of ultra thin films (sub-monolayer regime) and truly nanometric clusters (a thousand atoms or less). Despite the large use of MOKE, its ability to measure magnetic islands of several hundreds of atoms of a single atomic layer has been proven to be challenging [175, 22]. For our setup a coverage detection limit of 0.5 ML in transverse geometry and better than 0.1 ML in polar geometry is established. These values present a significant step forward.

Before pushing forward a complete description of the Kerr effect by solving the Maxwell equations, a paragraph is dedicated to the Faraday effect. In this context considerable

pioneering work was done. Results and conclusions can be readily applied to the Kerr geometry.

5.1.1 Faraday effect

The Faraday effect was discovered in 1845 by Michael Faraday [176]. He observed a rotation by an angle Θ_F of linearly polarized light passing through a variety of heavy glass, called silicated borate of lead, placed in between two electromagnetic poles. In his setup the propagation direction of the probing light and the magnetic field were collinear. When the light ray is tilted with respect to the magnetic field lines, only the component of the magnetic field parallel to the propagation direction is active. Obviously, a configuration where the magnetic field is perpendicular to the propagation direction does not show Faraday rotation.

Faraday realizes that upon reversing the poles by simply changing the direction of the electric current, the sign of rotation of polarization is reversed while the amplitude of rotation is the same as before. Further, he states that the amount of rotation is proportional to the distance l of the light travelled through the body and to the applied magnetic field H . Hence,

$$\Theta_F = p l H \quad (5.1)$$

p is called Verdet's constant after M. Verdet who has studied the Faraday rotation of different materials in a systematic way [177]. The proportionality stated in equation (5.1) has been verified for many diamagnetic and paramagnetic materials by other researchers. For example, in quartz $\Theta_F = 2^\circ/\text{cm}$ when placed in a field of 1 mT [178]. However, Kundt and Du Bois found a dramatic deviation for magnetic thin films of iron, cobalt, and nickel [179,180,181]. They report that the rotation slowly increases in high magnetic fields reaching asymptotically a limiting value. Already Du Bois guessed that the magnetization M is responsible for the rotation due to the similar behavior of the magnetization and the rotation in an external field. In addition, Kundt and Du Bois found at saturation magnetization exceptionally large Faraday rotations which amount to $210\,000^\circ/\text{cm}$ for iron, $190\,000^\circ/\text{cm}$ for cobalt, and $90\,000^\circ/\text{cm}$ for nickel [182]. The strong Faraday effect was later explained with the Weiss field of about 1000 T, which couples via spin-orbit interaction to the electron motion [183, 184].

Fresnel analyzed the Faraday effect by means of two circularly polarized electromagnetic waves with opposite sense of rotation. The Faraday rotation is,

$$\Theta_F = \frac{\omega l}{2c} (n_+(H) - n_-(H)) \quad (5.2)$$

where c is the speed of light in vacuum, ω the wave's frequency, and $n_+(H), n_-(H)$ the refractive indices of the positive and negative circularly polarized waves. The derivation of (5.2) is given in the appendix B.

5.1.2 Kerr effect

Experimentally, the Kerr effect manifests itself in the change of polarization (polar and longitudinal Kerr effect) or intensity (transverse Kerr effect) of polarized light when reflected from the surface of a magnetized sample. The change of polarization results generally in an elliptically polarized wave whose principal axis is rotated. Microscopically, the task is to calculate the two refractive indices by taking account for the spin-orbit interaction on the energy levels and wave functions. Argyres gave the first order effects of the spin-orbit interaction on the optical properties of a ferromagnet on the basis of the band theory of metals [178]. Macroscopically, the magneto-optic effects are described by a *refractive tensor* which replaces the ordinary index of refraction. It is obtained by calculating classically the interaction between the incident electromagnetic wave and the conduction electrons using the equation of motion of an electron in a time varying electro-magnetic field [185]. The reflection of a electromagnetic wave at the surface is summarized by the Fresnel coefficients [186]

$$\begin{pmatrix} E_s^r \\ E_p^r \end{pmatrix} = \begin{pmatrix} r_{ss} & r_{sp} \\ r_{ps} & r_{pp} \end{pmatrix} \begin{pmatrix} E_s^i \\ E_p^i \end{pmatrix} \quad (5.3)$$

where E_s^i, E_p^i refer to s and p polarized components of the incident wave and E_s^r, E_p^r to the ones of the reflected wave. E_p (p stands for the German word *parallel*) is in the plane of incidence and E_s (s stands for the German word *senkrecht*) is perpendicular to the plane of incidence.

For Kerr measurements three different geometries are distinguished according to the magnetization direction with respect to the plane of incidence and sample plane. In the polar configuration the magnetization is normal to the sample surface, in the longitudinal configuration \mathbf{M} is in the surface plane parallel to the plane of incidence, and in the transversal configuration \mathbf{M} is in the surface plane perpendicular to the plane of incidence. Figure 5.1 represents the polar, longitudinal, and transverse configuration.

In the following, the Fresnel coefficients will be derived for a thick magnetic film and an ultra thin magnetic film by solving the Maxwell equations (5.4a - 5.4d) while taking into account all the boundaries. Certainly, the validity of the macroscopic description of the magneto-optical effects may be questioned in the mono- or sub-monolayer regime. However, the magnetic properties for only a few atomic layers rapidly converge to the bulk limit and we expect the global trend to be reproduced correctly [1, 63].

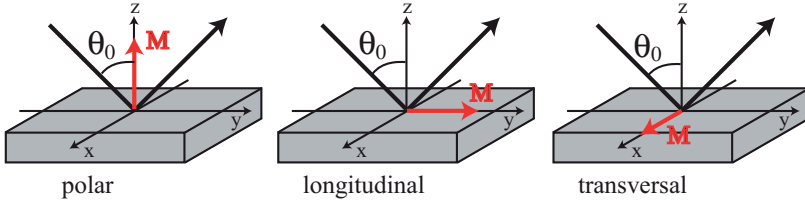


Figure 5.1: Schematic representation of the different Kerr geometries. In our setup the magnetic field can be applied at any angle in the $x - z$ plane with $B_{max} = 312$ mT. The angle θ_0 is 62° .

5.2 Analytical and Numerical Solution of the Maxwell Equations

The Maxwell equations can be found in any general electrodynamics textbook [187]. In SI units they write

$$\nabla \cdot \mathbf{B} = 0 \quad (5.4a)$$

$$\nabla \times \mathbf{E} + \frac{d\mathbf{B}}{dt} = 0 \quad (5.4b)$$

$$\nabla \cdot \mathbf{D} = \rho \quad (5.4c)$$

$$\nabla \times \mathbf{H} - \frac{d\mathbf{D}}{dt} = \mathbf{j} \quad (5.4d)$$

Remember that at the interface, the tangential components of the electric field \mathbf{E} and the magnetic field \mathbf{H} are continuous.

Considering magneto-optical effects, there is neither a current $\mathbf{j} = 0$ nor a space charge $\rho = 0$. Further we suppose $\mathbf{D} = \epsilon \mathbf{E}$ and $\mathbf{B} = \mu \mathbf{H}$ in all media, each being characterized by its own dielectric and magnetic permeability, ϵ and μ , respectively. The dielectric and magnetic permeability are frequency dependent and in general complex tensors of rank two. For optical frequencies $\mu = \mu_0$, where μ_0 is the magnetic permeability of vacuum [188]. The dielectric permeability is in case of vacuum:

the physical constant ϵ_0 .

a nonmagnetic crystal:

a symmetric tensor which represents the crystal symmetry [188]. It can be diagonalized and all principal values ϵ_1 , ϵ_2 , and ϵ_3 are greater than unity. For a cubic crystal $\epsilon_1 = \epsilon_2 = \epsilon_3$ meaning that it behaves like an isotropic body. In a *uniaxial* crystal (tetragonal, hexagonal, or rhombohedral) $\epsilon_1 = \epsilon_2 \neq \epsilon_3$ and in a *biaxial* crystal (triclinic, monoclinic, or orthorhombic) all principal values are different.

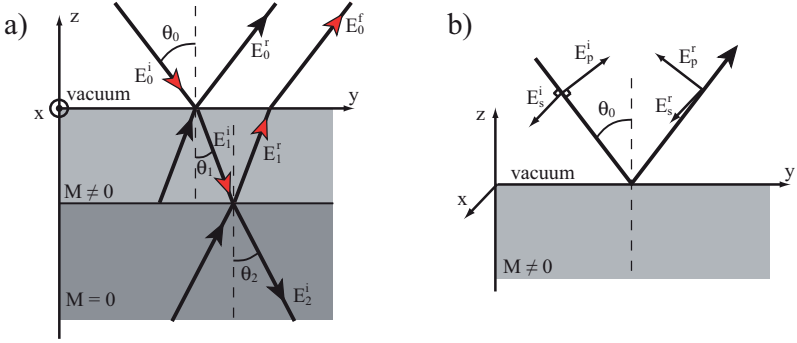


Figure 5.2: a) Sketch of the system under investigation showing the different incoming and reflected electromagnetic waves. The plane of incidence is $y - z$. b) The light polarization in a Kerr measurement is defined with respect to the plane of incidence. p is in the plane of incidence and s is perpendicular to it.

a magnetic crystal:

no longer symmetric, but satisfies the Onsager relation $\epsilon_{ij}(-\mathbf{M}) = \epsilon_{ji}(\mathbf{M})$ [189]. The relation between \mathbf{D} and \mathbf{E} is

$$\mathbf{D} = \epsilon \mathbf{E} = \epsilon_0 \epsilon_r \mathbf{E} + i \epsilon_0 \epsilon_r \mathbf{E} \times \mathbf{g} \quad (5.5)$$

where ϵ_r is the nonmagnetic part of the dielectric tensor and \mathbf{g} is the gyration vector taking account for the sample magnetization.

Note that the optical properties of an isotropic body placed in an external magnetic field and a magnetic crystal of cubic symmetry are both described by equation (5.5). In the former case $\mathbf{g} = p \mathbf{H}$ and in the latter case $\mathbf{g} = Q \mathbf{m}$ where Q is the Voigt constant and \mathbf{m} the direction cosine of the magnetization [182]. For a ferromagnetic sample the direct influence of an external magnetic field is neglected and only its role of magnetizing the sample in a certain direction is considered.

The system under investigation consists of three media and two boundaries as shown in Fig. 5.2 a). Usually we have first vacuum, second a magnetic thin film, and third a nonmagnetic substrate. The plane of incidence is in the $y - z$ plane, the angle θ_0 is 62° in our experimental setup. It is useful to introduce a new coordinate system (E_p, E_s, k) as shown in Fig.5.2 b).

From the Maxwell equations (5.4a - 5.4d) the wave equation is obtained

$$\Delta \mathbf{E} - \mu_0 \epsilon \frac{d^2 \mathbf{E}}{dt^2} = 0. \quad (5.6)$$

A solution is a plane wave $\mathbf{E}(\mathbf{r}, t) = \mathbf{E}_0 e^{\pm i(\mathbf{k}\mathbf{r} - \omega t)}$ where \mathbf{k} is the wave vector. For a wave propagating in the direction of the wave vector we have $\mathbf{E}(\mathbf{r}, t) = \mathbf{E}_0 e^{i(\mathbf{k}\mathbf{r} - \omega t)}$ which leads to the set of equations

$$(k^2 - \mu_0 \epsilon \omega^2) \mathbf{E} = 0. \quad (5.7)$$

The route will be in a first time to find for a given dielectric tensor the eigenvalues (the indices of refraction n_{\pm}) and eigenvectors (electromagnetic wave) of the set of equations given above in order to describe the wave propagation in a given medium.

In vacuum:

$\epsilon = \epsilon_0$. We obtain $k^2 = \mu_0 \epsilon_0 \omega^2 = \omega^2/c^2$, when using $c = 1/\sqrt{\mu_0 \epsilon_0}$ for the speed of light in vacuum. The refractive index n is introduced obeying the relation $\mathbf{k} = \frac{\omega}{c} \mathbf{n}$. In vacuum $n_0 = 1$. The eigenvector is

$$\mathbf{E}(\mathbf{r}, t) = \mathbf{E}_0 e^{i \frac{\omega}{c} (\mathbf{n}\mathbf{r} - ct)}. \quad (5.8)$$

The electromagnetic wave can have any polarization in vacuum. For MOKE measurements we use linearly polarized light. Hence, $\mathbf{E}_0 = \mathbf{E}_p$ or $\mathbf{E}_0 = \mathbf{E}_s$ as well as linear combinations of \mathbf{E}_p and \mathbf{E}_s .

In a nonmagnetic crystal:

The nonmagnetic substrates (Rh, Au, Pd,...) we used are of cubic symmetry reducing the tensor ϵ to the scalar $\epsilon_0 \epsilon_r$. We obtain $k^2 = \epsilon_r \omega^2/c^2$, thus $n = \sqrt{\epsilon_r}$. The electromagnetic wave is the same as in vacuum.

In a magnetic crystal:

The magnetic thin film is modelled by an isotropic nonmagnetic part ϵ_r and the gyration vector which is proportional to the magnetization. From equation (5.5) we can deduce

$$\epsilon = \epsilon_0 \epsilon_r \begin{pmatrix} 1 & iQm_z & -iQm_y \\ -iQm_z & 1 & iQm_x \\ iQm_y & -iQm_x & 1 \end{pmatrix} \quad (5.9)$$

The eigenvalues are $n_{\pm} = \sqrt{\epsilon_r} (1 \pm \frac{1}{2} Q \mathbf{m} \hat{\mathbf{k}})$ and the eigenvectors are right and left circularly polarized waves.

The wave propagation can be expressed in form of a general 4×4 propagation matrix D which is defined in the (E_p, E_s, \mathbf{k}) coordinate system [190]. For a film of thickness d we have

$$D = \begin{pmatrix} U \cos \delta_i & U \sin \delta_i & 0 & 0 \\ -U \sin \delta_i & U \cos \delta_i & 0 & 0 \\ 0 & 0 & \frac{1}{U} \cos \delta_r & -\frac{1}{U} \sin \delta_r \\ 0 & 0 & \frac{1}{U} \sin \delta_r & \frac{1}{U} \cos \delta_r \end{pmatrix} \quad (5.10)$$

where

$$U = \exp\left(-\frac{2\pi ind \cos \theta}{\lambda}\right) \quad (5.11)$$

$$\delta_i = \frac{2\pi ind}{\lambda}(m_y Q \tan \theta + m_z) \quad (5.12)$$

$$\delta_r = \frac{2\pi ind}{\lambda}(m_y Q \tan \theta - m_z) \quad (5.13)$$

where the index i denotes the incident wave and r the reflected wave. The parameters $n, d, Q, \theta, \mathbf{m}$ have to be given for each material j . However, the index j has been omitted in equations (5.10 - 5.13).

At the interface, the tangential components of the electric field \mathbf{E} and the magnetic field \mathbf{H} are continuous. The tangential components may be summarized in a column vector F

$$F = \begin{pmatrix} E_x \\ E_y \\ H_x \\ H_y \end{pmatrix} \quad (5.14)$$

linked to E_p and E_s by the relation

$$F = \begin{pmatrix} E_x \\ E_y \\ H_x \\ H_y \end{pmatrix} = A \begin{pmatrix} E_s^i \\ E_p^i \\ E_s^r \\ E_p^r \end{pmatrix} \quad (5.15)$$

A being the 4×4 medium boundary matrix [190]. It is given by

$$A = \begin{pmatrix} 1 & 0 & 1 & 0 \\ -\frac{iQ \sin^2 \theta}{2} \left(m_y \frac{1 + \cos^2 \theta}{\cos \theta \sin \theta} - m_z \right) & \cos \theta - iQ m_x \sin \theta & \frac{iQ \sin^2 \theta}{2} \left(m_y \frac{1 + \cos^2 \theta}{\cos \theta \sin \theta} + m_z \right) & -\cos \theta - iQ m_x \sin \theta \\ \frac{inQ}{2} (m_y \sin \theta + m_z \cos \theta) & -n & \frac{inQ}{2} (m_y \sin \theta - m_z \cos \theta) & -n \\ n \cos \theta & \frac{inQ}{2} (m_y \tan \theta + m_z) & -n \cos \theta & -\frac{inQ}{2} (m_y \tan \theta - m_z) \end{pmatrix} \quad (5.16)$$

Here also the index j for the parameters $n, d, Q, \theta, \mathbf{m}$ has been omitted. Solving the reflection/transmission problem is now a simple matrix multiplication. We compute for any multilayer system

$$S = A_i^{-1} \left(\prod_j A_j D_j A_j^{-1} \right) A_f \quad (5.17)$$

which can be expressed by blocks of 2×2 submatrices

$$S = \begin{pmatrix} G & H \\ I & J \end{pmatrix} \quad (5.18)$$

being related to the Fresnel coefficients by taking IG^{-1} .

5.2.1 The thin film limit

For a single thin magnetic film of thickness d on any substrate $S = A_0^{-1}A_1D_1A_1^{-1}A_2$. The indices 0, 1, 2 correspond to vacuum, the magnetic thin film, and the substrate, respectively, as defined in Fig. 5.2 a). The Fresnel coefficients obtained from S describe the reflection of a beam running along the path indicated by the red arrows in the same figure. They are calculated in the thin film limit $2\pi|n_1|d/\lambda \ll 1$ and in first order of Q

$$r_{ss} = \frac{n_0 \cos \theta_0 - n_2 \cos \theta_2}{n_0 \cos \theta_0 + n_2 \cos \theta_2} + \frac{4\pi i n_0 d \cos \theta_0 (n_1^2 \cos^2 \theta_1 - n_2^2 \cos^2 \theta_2)}{\lambda (n_0 \cos \theta_0 + n_2 \cos \theta_2)^2} \quad (5.19a)$$

$$r_{ps} = -2\pi n_0 d Q \cos \theta_0 \left[\frac{m_z \cos \theta_1 (-n_1 n_2 \cos^2 \theta_1 + n_1^2 \cos \theta_1 \cos \theta_2 + n_2^2 \cos \theta_1 \cos \theta_2 + n_1 n_2 \cos^2 \theta_2)}{\lambda \cos^2 \theta_1 (n_2 \cos \theta_0 + n_0 \cos \theta_2) (n_0 \cos \theta_0 + n_2 \cos \theta_2)} - \frac{m_y \sin \theta_1 (n_1 n_2 \cos^2 \theta_1 - n_1^2 \cos \theta_1 \cos \theta_2 + n_2^2 \cos \theta_1 \cos \theta_2 + n_1 n_2 \cos^2 \theta_2)}{\lambda \cos^2 \theta_1 (n_2 \cos \theta_0 + n_0 \cos \theta_2) (n_0 \cos \theta_0 + n_2 \cos \theta_2)} \right] \quad (5.19b)$$

$$r_{pp} = \frac{n_2 \cos \theta_0 - n_0 \cos \theta_2}{n_2 \cos \theta_0 + n_0 \cos \theta_2} - \frac{4\pi i n_0 d \cos \theta_0 (n_1^2 \cos^2 \theta_2 - n_2^2 \cos^2 \theta_1)}{\lambda (n_0 \cos \theta_2 + n_2 \cos \theta_0)^2} + \frac{8\pi m_x n_0 n_1 n_2 d Q \cos \theta_0 \sin \theta_1 \cos \theta_2}{\lambda (n_2 \cos \theta_0 + n_0 \cos \theta_2)^2} \quad (5.19c)$$

$$r_{sp} = -2\pi n_0 d Q \cos \theta_0 \left[\frac{m_z \cos \theta_1 (n_1 n_2 \cos^2 \theta_1 + n_1^2 \cos \theta_1 \cos \theta_2 + n_2^2 \cos \theta_1 \cos \theta_2 - n_1 n_2 \cos^2 \theta_2)}{\lambda \cos^2 \theta_1 (n_2 \cos \theta_0 + n_0 \cos \theta_2) (n_0 \cos \theta_0 + n_2 \cos \theta_2)} + \frac{m_y \sin \theta_1 (n_1 n_2 \cos^2 \theta_1 + n_1^2 \cos \theta_1 \cos \theta_2 - n_2^2 \cos \theta_1 \cos \theta_2 + n_1 n_2 \cos^2 \theta_2)}{\lambda \cos^2 \theta_1 (n_2 \cos \theta_0 + n_0 \cos \theta_2) (n_0 \cos \theta_0 + n_2 \cos \theta_2)} \right] \quad (5.19d)$$

In Fig. 5.3 we plot for polar and longitudinal geometry the absolute value of $\Phi = \Phi' + i\Phi''$, the Kerr rotation Φ' , and ellipticity Φ'' ; for p -polarized $\Phi_p = \frac{r_{sp}}{r_{pp}}$ and s -polarized $\Phi_s = \frac{r_{ps}}{r_{ss}}$ light. For transverse geometry the Kerr asymmetry A_K is plotted which is defined as [191]

$$A_K = \frac{|r_{pp}(+m)|^2 - |r_{pp}(-m)|^2}{|r_{pp}(+m)|^2 + |r_{pp}(-m)|^2} \quad (5.20)$$

for p -polarized light. Note that s -polarized light does not give rise to a transverse magneto-optic effect, i.e. the asymmetry is zero. $|\Phi|$, Φ' , Φ'' , and A_K are represented as a function of θ_0 for a 0.2 nm thick Co film on Au. We used the refractive index $n_0 = 1$ for vacuum and the bulk refractive index for Co and Au found in literature at the laser wave length $\lambda = 782$ nm: $n_{\text{Co}} = 2.45 + 4.74 i$ [192] and $n_{\text{Au}} = 0.16 + 4.69 i$ [193, 194]. The Voigt constant for Co bulk at the given wave length is $Q = 0.04 - 0.02 i$ [185]. The solid line is the numerical solution of S , the dashed line is the thin film approximation to the first order of Q given in equations (5.19a - 5.19d), and the dotted line is the thin film approximation to the first order of Q given in Ref. 195. It is obvious that the dashed line follows much better the numerical solution than the dotted line. In two cases (longitudinal Φ' and Φ'') the sign is even inverted. Further, the Kerr asymmetry is zero, because the equations lack of the transverse term m_x . The transverse term is already missing in the medium boundary matrix A_j in Ref. 195. Is not clear if this is a transcription error or if it has been changed in the view to treat only polar and longitudinal Kerr geometry.

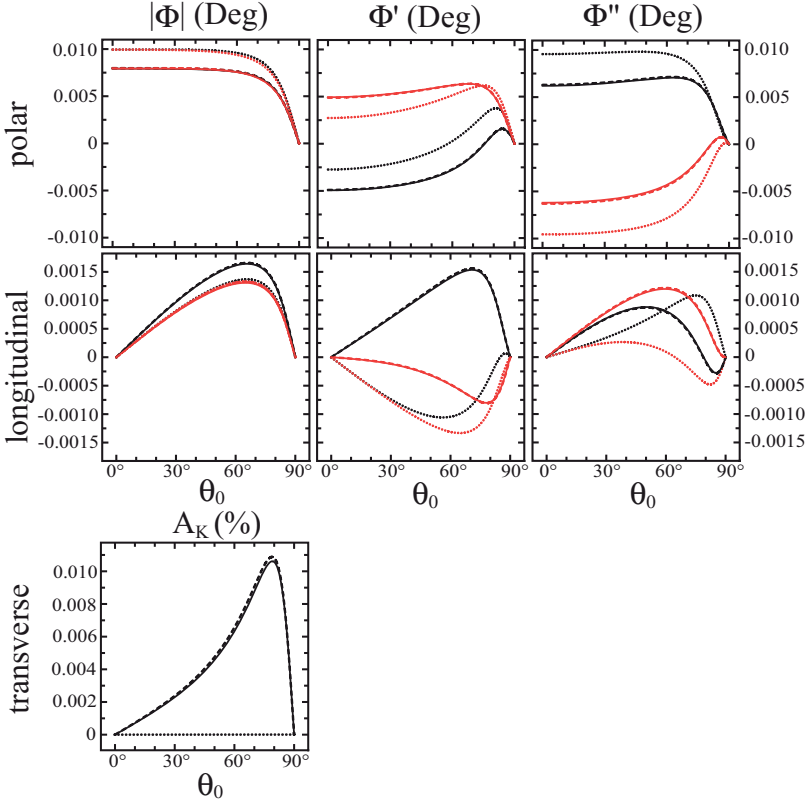


Figure 5.3: 0.2 nm thick Co film on Au. In polar and longitudinal geometry the absolute value of $\Phi = \Phi' + i\Phi''$, the Kerr rotation Φ' , and Kerr ellipticity Φ'' are presented as a function of θ_0 ; in transverse geometry $A_K(\theta_0)$ is represented. For p -polarized light we plot $\Phi_p = \frac{r_{sp}}{r_{pp}}$ (black line) and for s -polarized light $\Phi_s = \frac{r_{ps}}{r_{ss}}$ (red line). The solid line is the numeric solution for Φ_p and Φ_s , the dashed line is the thin film approximation in the first order of Q given in equation (5.19a - 5.19d), and the dotted line is the thin film approximation in the first order of Q given in Ref. 195.

In order to question the validity of the thin film approximation $2\pi|n_1|d/\lambda \ll 1$ we can replace the parameters by the numerical values given above. The condition $d \ll 23$ nm is obtained. To visualize the different thin film approximations compared to the numerical solution, we show in Fig. 5.4 $|\Phi|$, Φ' , and Φ'' as a function of Co film thickness in polar and

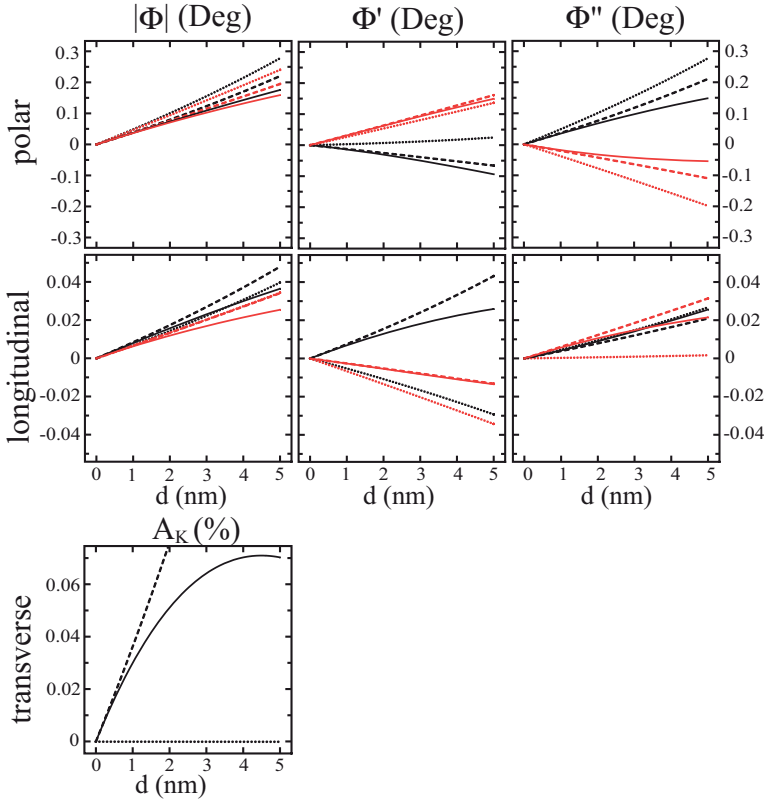


Figure 5.4: Co on Au at $\theta_0 = 62^\circ$. In polar and longitudinal geometry $|\Phi|$, Φ' , and Φ'' are presented as a function of the film thickness d ; in transverse geometry $A_K(d)$ is represented. For p -polarized light we plot $\Phi_p = \frac{r_{sp}}{r_{pp}}$ (black line) and for s -polarized light $\Phi_s = \frac{r_{ps}}{r_{ss}}$ (red line). The solid line is the numeric solution for Φ_p and Φ_s , the dashed line is the thin film approximation in the first order of Q given in equation (5.19a - 5.19d), and the dotted line is the thin film approximation in the first order of Q given in Ref. 195.

longitudinal geometry for a fixed angle of incidence of 62° . For transverse geometry A_K is represented as a function of d at $\theta_0 = 62^\circ$. It can be seen that the thin film approximation holds only up to a few nm. For transverse geometry the validity is even restricted to the sub-nm regime. Following the exact solution to higher coverages we stress that the sign changes for some configurations.

The new findings have to be taken into account when optimizing an experimental Kerr setup to study ultra thin films. The Kerr signal of all geometries depends critically on the angle of incidence θ_0 , as presented in Fig. 5.3, suggesting that the choice of θ_0 has to be well considered.

5.2.2 The thick film limit

For $d > 100$ nm the film is thick enough to be well described by the Fresnel coefficients derived in Ref. 186 for bulk. This is due to the limited penetration depth of visible light in metals. For Co at $\lambda = 782$ nm we obtain with equation (B.9) 26 nm. The Fresnel coefficients for a thick magnetic layer or bulk can equally be obtained from equation (5.17). We just need to compute $S = A_0^{-1}A_1$ in the first order of Q

$$r_{ss} = \frac{n_0 \cos \theta_0 - n_1 \cos \theta_1}{n_0 \cos \theta_0 + n_1 \cos \theta_1} \quad (5.21a)$$

$$r_{ps} = -i \frac{n_0 n_1 Q \cos \theta_0 (m_z \cos \theta_1 - m_y \sin \theta_1)}{\cos \theta_1 (n_1 \cos \theta_0 + n_0 \cos \theta_1) (n_0 \cos \theta_0 + n_1 \cos \theta_1)} \quad (5.21b)$$

$$r_{pp} = \frac{n_1 \cos \theta_0 - n_0 \cos \theta_1}{n_1 \cos \theta_0 + n_0 \cos \theta_1} + i \frac{2n_0 n_1 \cos \theta_0 \sin \theta_1 m_x Q}{n_1 \cos \theta_0 + n_0 \cos \theta_1} \quad (5.21c)$$

$$r_{sp} = -i \frac{n_0 n_1 Q \cos \theta_0 (m_z \cos \theta_1 + m_y \sin \theta_1)}{\cos \theta_1 (n_1 \cos \theta_0 + n_0 \cos \theta_1) (n_0 \cos \theta_0 + n_1 \cos \theta_1)} \quad (5.21d)$$

In Fig. 5.5 we plot Φ , Φ' , and Φ'' as a function of θ_0 for polar and longitudinal geometry as well as the Kerr asymmetry A_K as a function of θ_0 for transverse geometry.

5.3 UHV compatible MOKE setup

A photograph of the sample stage with the MOKE optics is shown in Fig. 5.6 a). It is integrated into a UHV chamber which has been designed to prepare and characterize the sample in the very same position. In addition, samples can be transferred to a manipulator for Auger electron spectroscopy, to a sample storage, and in and out via a fast entry-lock. The sample is mounted as a sandwich in between sapphire rings on a molybdenum sample holder which is inserted in the sample stage. One wire for the sample potential and a W5%Rh-W26%Rh (C-type) thermocouple are directly attached to the sample. Spring loaded contacts are mounted for these three wires onto the sample stage. The sample stage is connected with a silver plated copper braid to a liquid helium flux cryostat. A minimum sample temperature of $T = 60$ K can be reached during normal operation allowing sample exchange. This value may be lowered to $T \simeq 40$ K when screwing the sample holder tightly to the sample stage, thus improving the thermal contact. The sample can be heated up to $T = 2000$ K via radiation and electron bombardment using a filament

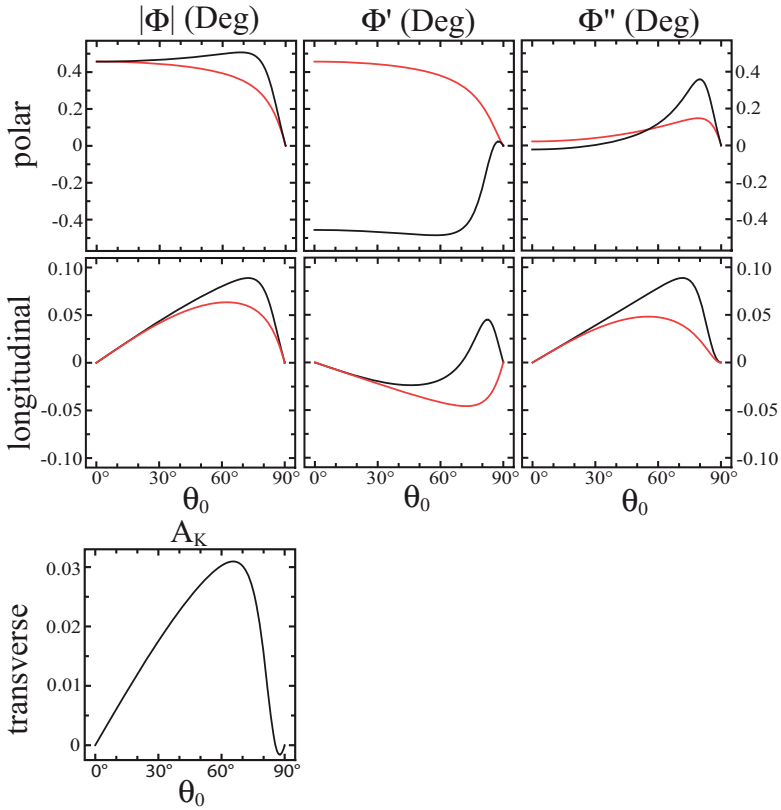


Figure 5.5: Co bulk. In polar and longitudinal geometry the absolute value of $\Phi = \Phi' + i\Phi''$, the Kerr rotation Φ' , and Kerr ellipticity Φ'' are presented as a function of θ_0 ; in transverse geometry $A_K(\theta_0)$ is represented. For p -polarized light we plot $\Phi_p = \frac{r_{sp}}{r_{pp}}$ (black line) and for s -polarized light $\Phi_s = \frac{r_{ps}}{r_{ss}}$ (red line).

from a 50 W halogen light bulb placed close to the sample backside. The UHV chamber is further equipped with standard tools for surface preparation and characterization, such as an ion gun and molecular beam evaporators pointing to the sample stage. A home-built beetle type STM allows the characterization of the sample morphology [196].

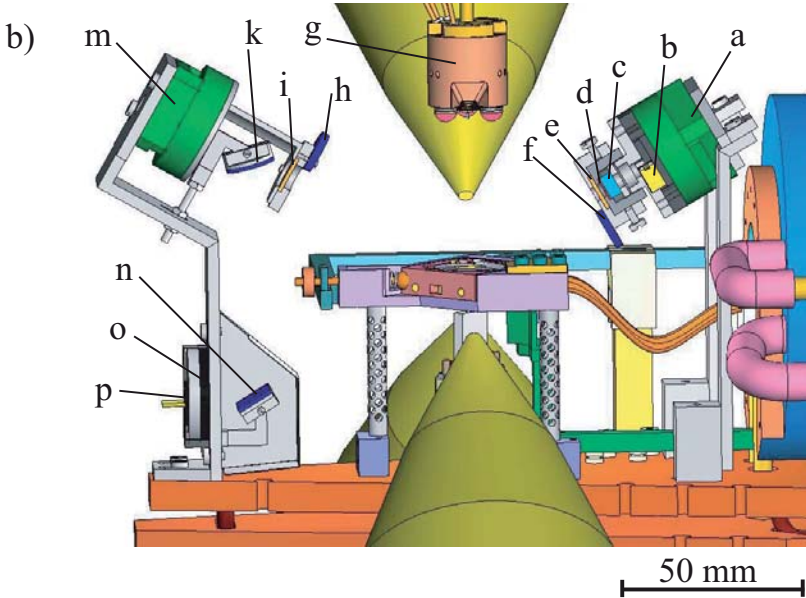
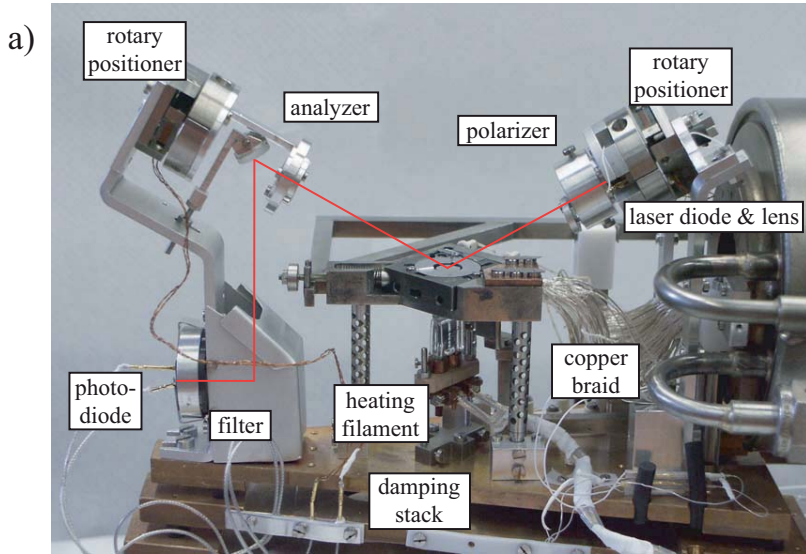
The technical drawing shown in Fig. 5.6 b) displays the components of the MOKE. We opted for the plane of incidence perpendicular to the magnetic field leaving the largest

room to fit the optical setup and to adjust θ_0 . The light source is a laser diode (Axcel Photonics, CL-785-0050-S90) emitting at 782 nm. It is operated with a constant forward current of $I_{\text{laser}} = 50$ mA corresponding to an output power of 11 mW in air. The emitted beam is collimated by a plano-convex sapphire lens (Oriel, 74303) and passes an aperture creating a parallel beam with a diameter of about 1 mm along the entire optical path. The light is linearly polarized by two stacked dichroic sheets (codixx, VIS 700 BC4), each of them having an extinction ratio of 1:80 000. They will be called polarizer in the following. Ideally, prism polarizers should be used having an extinction ratio better than 1:100 000. However, these prisms are held together by a refractive index matching glue which is neither UHV compatible nor bakeable. Laser diode, lens, aperture, and polarizer are rigidly mounted on a piezo driven rotary positioner with 360° travel and a minimum step size of 0.001° (attocube, ANR100). This allows continuous adjustment of the polarization direction from s to p , as well as opening/closing a front-end shutter. The shutter protects the sheet polarizers against Ar^+ ion bombardment and metallization when the sample is sputtered or metallic films are deposited, respectively, both having the long term drawback of deteriorating the performance of the polarizer.

The laser beam is reflected by the sample and hits another pair of dichroic sheets which we call analyzer. The analyzer is mounted on an identical rotary positioner as the polarizer allowing to freely adjust the relative angle and to open/close a protective shutter during sample preparation, as well. Two high quality mirrors (WZWOPTICAG, S18x12x2.5-M01 and SD10x2-M01) deflect the beam onto a photodiode (Hamamatsu, S1337-1010BQ) measuring the intensity. To retain parasitic light the photodiode is screened by a filter (Oriel, 780FS10-25) with its maximum transmission centered around 783 ± 5 nm. With this setup we obtain extinction ratios better than 1:40 000 on metal samples, depending on the quality of the polishing of the single crystal surface. The extinction ratio is defined as the ratio between the minimum light intensity I_{min} measured by the photo detector when polarizer and analyzer are oriented perpendicular, and the maximum light intensity I_{max} when polarizer and analyzer are oriented parallel to each other. The definitions of I_{min} and I_{max} will be used further below.

The mechanical supports of both rotary positioners and the sample stage are fixed on top of the uppermost plate of a passive damping stack reducing mechanical vibrations for Kerr and STM measurements. The incident angle θ_0 with respect to the surface normal can be adjusted to $60^\circ \pm 10^\circ$ by *ex situ* positioning of the laser with respect to the sample. The laser beam is in the $y - z$ plane.

Special care was taken to use only nonmagnetic materials for all parts seen in Fig. 5.6 a). Mechanical parts were made in aluminium and copper while titanium was used for screws and bolts. This is of prime importance in order to avoid artifacts in the measured intensity when single parts move with respect to each other driven by the applied magnetic field. Equally, a good thermal anchoring of all components is necessary in order to reach a good



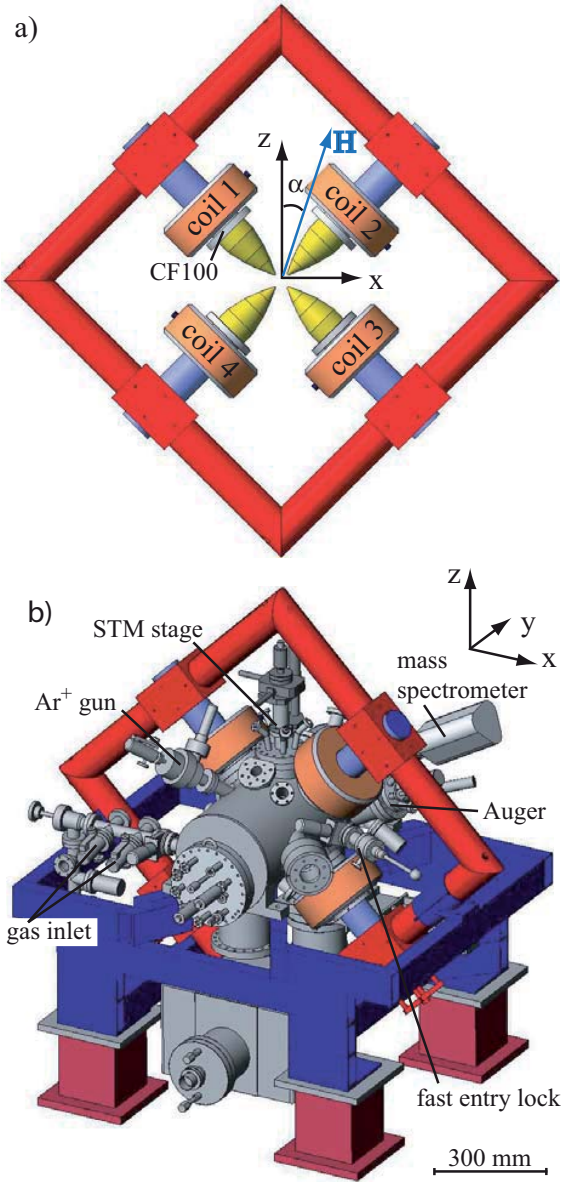
Laser	axcel photonics	CL-785-0050-S90 6	www.axcelphotonics.com
current source	ILX Lightwave	LDX-3412	www.ilxlightwave.com
sheet polarizer	codixx	VIS 700 BC4	www.codixx.de
mirror 1	WZWOPTICAG	S18x12x2.5-M01	www.wxw.ch
mirror 2	WZWOPTICAG	SD10x2-M01	www.wxw.ch
lens	Oriel	74303	www.newport.com
filter	Oriel	780FS10-25	www.lot-oriel.com
photodiode	hamamatsu	S1337-1010BQ	www.hamamatsu.com
rotational stage	attocube	ANR100	www.attocube.com
electronics	attocube	ANC150	www.attocube.com

Table 5.1: Summary of all commercially available parts used to built the UHV compatible MOKE setup.

detection limit which depends on the laser beam stability, the extinction ratio and the performance of the photodiode. In UHV the exchange gas is missing, thus thermalization by convection is not anymore possible and consequently the laser and all objects interacting with the laser beam heat up compared to ambient conditions. Therefore, the laser chip is mounted on a Au plated Cu submount guaranteeing a good heat conduction. We note that standard laser diodes are usually mounted onto a base plate containing magnetic elements which is not acceptable for the present setup. With this solution we obtain a stable light source operating under UHV conditions. In UHV the threshold current is increased by 5% and the output power is decreased by 30% at $I_{\text{laser}} = 50$ mA.

All components along the optical path absorb some of the intensity of the laser beam which is transformed in heat and partially re-emitted about the same wavelength. The re-emitted light joins with the laser beam in the deterioration of the extinction ratio since it is unpolarized. Considering the sheet polarizer as a point source suggests to place the photo detector as far as possible from the analyzer. Measuring the extinction ratio as a function of distance between the photo detector and analyzer results in a $1/\text{distance}^2$ law strengthening the

Figure 5.6: a) Photograph of the MOKE setup with all optical components in UHV. The red line indicates the laser beam. All parts are mounted on a stack of copper plates separated by viton spacers for vibrational damping. (b) Technical drawing. Only three of the four poles (yellow cones) generating the magnetic field are shown. The STM is indicated in its rest position. It is lowered onto the sample for STM imaging. a) rotational stage, b) laser diode, c) lens, d) aperture, e) polarizer, f) shutter, g) STM, h) shutter, i) analyzer, k) mirror, m) rotary positioner, n) mirror, o) filter, and p) photodiode.



hypothesis. For this reason two mirrors extending the optical path are installed.

The photodiode heats up upon light absorption. This change in temperature of the photodiode affects the population of the atomic levels given by the partition function. Generally, this gives rise to an additional linear slope of positive or negative sign corresponding to heating and cooling, respectively. Assuming that the change in intensity is proportional to the total intensity, the best measuring configuration would be at I_{\min} which has been confirmed in tests.

Based on our experience, all components are UHV compatible and bakeable at 120°C even though for some optical parts only storage temperatures up to 80°C are guaranteed by the manufacturer. We routinely achieve a base pressure $< 1 \times 10^{-10}$ mbar. All commercially available parts used to built the UHV compatible MOKE setup are summarized in table 5.1.

Figure 5.7 a) shows the four pole electromagnet with the sample being located in the center (see Fig. 5.6). It creates a magnetic field at any angle α in the $x - z$ plane, α being the angle included in between the applied field vector \mathbf{H} and the surface normal z . We used four water cooled coils (GMW Inc.) situated outside the UHV chamber as shown in Fig. 5.7. Each of them produces a field of 120 mT at a maximum applied current of 40 A. Tapered soft iron cores (yellow cones in Figs. 5.6 and 5.7) are welded into bored CF 100 flanges which bring the magnetic field to the sample. The cores are continued outside the vacuum chamber by cylinders (blue in Fig. 5.7) which can be removed for disassembly. The soft iron yoke (red parts in Fig. 5.7) closes the magnetic field lines, thus reducing stray fields. Poles, cylinders, and yoke are made of ARMCO iron. In order to prevent oxidation, the parts exposed to air are painted while the vacuum side poles were coated with a 12 μm thick nickel-phosphor layer.

The shape, dimensions, and arrangement of the poles were optimized by finite element calculations to obtain maximum field homogeneity and amplitude at the sample location while leaving enough room for the STM. The horizontal distance between the poles is 30 mm allowing to pass with the STM, having a diameter of 21 mm. The maximum magnetic field in the sample region measured with a Hall sensor amounts to $B_{\max} =$

Figure 5.7: a) Drawing of the four pole electromagnet. The poles (yellow) are welded into CF100 flanges and screwed on the UHV chamber. The poles having a diameter of 96 mm are continued by a cylinder (light blue) entering a square shaped yoke (red colored) surrounding the UHV chamber. Yoke, cylinders, and coils can easily be unmounted during chamber bakeout. The sample sits in the center of the four poles (see Fig. 5.6 for details). α is the angle between the applied field vector \mathbf{H} and the surface normal z . (b) Drawing of the UHV chamber showing how the poles, coils, and yoke are mounted on the chamber. The positions of STM, Auger, Ar^+ ion gun, and fast entry lock are indicated.

312 mT along z or x directions. The measured value is 10% larger than the one predicted from finite element calculations. For $\alpha = 45^\circ$ the maximum field amounts to 222 mT. B_{\max} changes by 2% when moving from the sample center ($x = 0$ mm) to its edge ($x = 4$ mm). In the region probed with the laser beam, having a spot diameter of 1 mm, the field variation is less than 0.5%. Thus, the magnetic field can be considered homogeneous, within the area of the laser spot.

The soft iron poles have the intrinsic property of a remanent magnetization which depends on the amplitude and sweep rate of the magnetic field. This remanence creates a residual field varying from 2 mT to 7 mT for typical sweep rates field ranging from 0.2 T/min to 1 T/min and going up to the maximum field, which has to be corrected for in the M(H) curves.

5.4 First Measurements

The sensitivity of the MOKE setup was tested on two different systems: *i*) a continuous Co film on Rh(111) having an in-plane easy axis and *ii*) an array of bilayer Co islands on Au(11,12,12) having an out-of-plane easy axis. Numerical calculations of the Kerr signal of the measured systems were used to optimize the incident angle θ_0 in such a way that polar and transverse measurements are feasible at the same time. Hence, we calculate the Kerr rotation for polar geometry and the Kerr asymmetry for transverse geometry of a thin Co film on Au or Rh, respectively. In fig. 5.8 the angular and thickness dependence of Φ' and A_K are displayed. Φ' has a large and almost constant signal up to about $\theta_0 = 60^\circ$ diminishing rapidly for larger angles whereas the transverse Kerr asymmetry has a clear maximum around $\theta_0 = 80^\circ$. Choosing an angle of incidence of $\sim 60^\circ$ results in a still very good polar Kerr signal, while being able to detect a reasonable transverse Kerr signal. The measurements presented below are carried out with $\theta_0 = 62^\circ$. However, the MOKE setup can be optimized for polar or transverse Kerr configuration by changing θ_0 in order to improve the Kerr signal and therewith the detection limit for a given system.

5.4.1 Co/Rh(111)

To determine the detection limit for transverse MOKE we deposited 0.9 ML Co from a high purity rod (99.995%) on Rh(111) at room temperature after having prepared the Rh(111) single crystal surface by repeated cycles of Ar^+ ion sputtering (1.3 keV, 300 K, $3 \mu\text{A}/\text{cm}^2$), oxygen dosing ($3 \cdot 10^{-8}$ mbar, 800 K) and flash annealing at 1500 K. Magnetization loops were taken of the as deposited film in the transverse and polar Kerr geometry. For the transverse configuration 10 loops were recorded in order to obtain a better signal-to-noise ratio. The average and the standard error are displayed at each field in Fig. 5.9 a) evidencing a square loop with a sharp jump of the magnetization at the

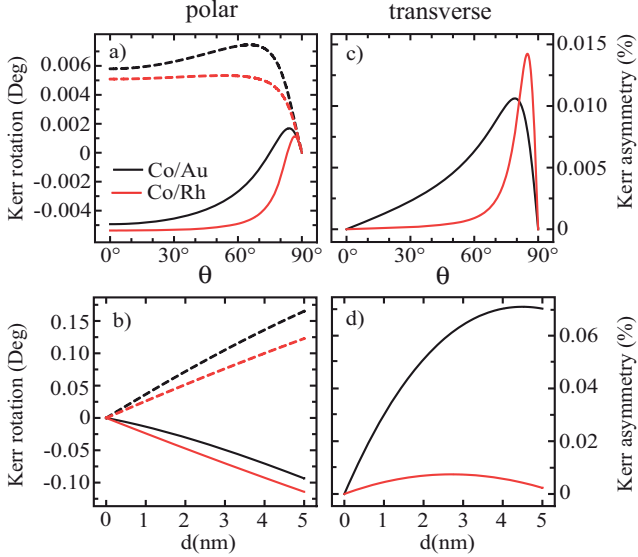


Figure 5.8: Calculated Kerr rotation (a,b) and asymmetry (c,d) as a function of the angle of incidence θ_0 for a film thickness of $d = 0.2$ nm (a,c) and as a function of film thickness at fixed angle of incidence $\theta_0 = 62^\circ$ (b,d) for a Co film on Au (black lines) and Rh (red lines) at $\lambda = 782$ nm laser wave length. a) and b) polar Kerr: $\text{Re}(r_{sp}/r_{pp})$ is shown for p -polarized light (full line) and $\text{Re}(r_{ps}/r_{ss})$ for s -polarized light (dashed line) c) and d) transverse Kerr: Kerr asymmetry for p -polarized light.

switching field. This shape is indicative of an in-plane easy magnetization axis. Assuming as a sensitivity criterium that the Kerr signal has to be at least as large as the noise level, we derive 0.5 ML as the detection limit for the transverse geometry.

In polar geometry, the curve is more s-shaped and the magnetization does not reach saturation at the maximum available field (see Fig. 5.9 b)). Here, we took 3 hysteresis loops for averaging. For comparison with the calculations in the former section we represented the Kerr rotation Φ' for polar geometry. Φ' is obtained from

$$\Phi' = \frac{\Delta I}{I_0(\delta)} \frac{\delta}{2} \quad (5.22)$$

where ΔI is the measured intensity variation as a function of the applied field, $I_0(\delta)$ is the intensity in absence of an applied field, and δ is a small angle of the analyzer off total extinction [190]. $\delta = 0.5^\circ$ was estimated assuming $I_0(\delta) = I_{\min} + I_{\max} \sin^2 \delta$

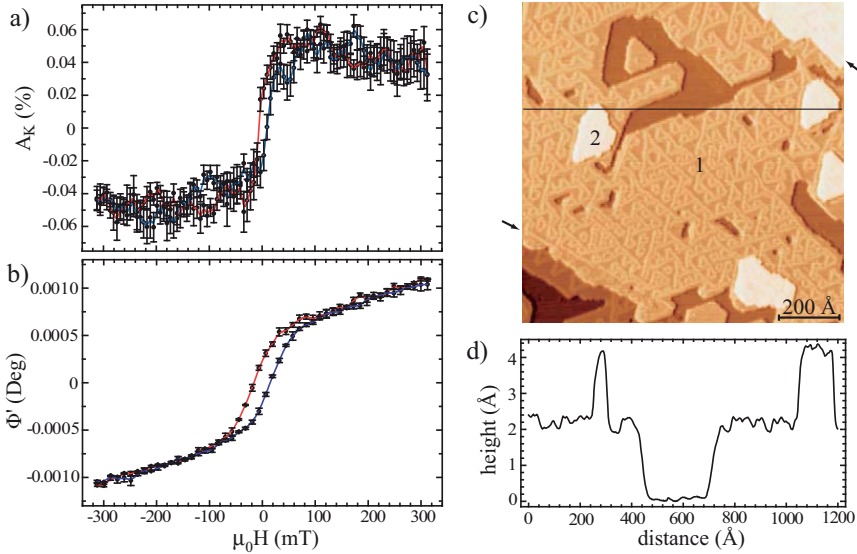


Figure 5.9: 0.9 ML Co/Rh(111) deposited and measured at $T = 300$ K. a) transverse Kerr asymmetry using p-polarized light (average of 10 hysteresis loops; forward sweep blue, backward sweep red). The error bar is the standard error (standard deviation/ \sqrt{N} , where N is the number of hysteresis loops) b) polar Kerr using p-polarized light (average of 3 hysteresis loops; forward sweep blue, backward sweep red) c) STM image of the deposited film ($U_T = -1.5$ V, $I_T = 2.7$ nA, $T = 300$ K). In order to increase the contrast the image is represented as if the surface was illuminated from the left. The Rh(111) surface remains partially uncovered, most is covered by one atomic layer of Co (label 1) and a few islands grow in the second layer (label 2). Two steps running through the image are indicated by the arrows. d) Representation of the linecut indicated in c) evidencing the surface reconstruction of the first and second layer which is seen with an apparent height of 0.4 Å and the peak to peak STM noise which is about 0.05 Å.

(For this sample we measured an extinction ratio of $I_{\min}/I_{\max} = 1:47000$). The polar Kerr has a larger signal ($\Phi' = 0.001^\circ$ corresponds to $\Delta I/I_0(\delta) = 0.4\%$) and consequently a much better signal-to-noise ratio compared to the transverse one as we expect from the calculated curves. For an angle of incidence of 62° and a 0.2 nm thick saturated Co film the calculated polar Kerr signal is almost 10 times the transverse signal. From the signal-to-noise ratio in Fig. 5.9 b) we derive a detection limit of 0.05 ML for out-of-plane magnetized films.

An STM image of the Co film is shown in Fig. 5.9 c). Room temperature growth results in interconnected large Co patches, one atomic layer high, leaving about 15% of the substrate uncovered. 0.05 ML of Co grows in the second layer in form of small compact islands. Both Co layers show partial surface dislocations imaged as protrusions, separating fcc from hcp stacking areas. This way part of the stress resulting from the lattice mismatch between Co and Rh of $(d_{\text{Co}} - d_{\text{Rh}})/d_{\text{Rh}} = -6.6\%$, where d is the in plane nearest neighbor distance, is released.

5.4.2 Co/Au(11 12 12)

Co/Au(11,12,12) forms an array of nanometric islands and therefore is an ideal model system for testing the performance of the UHV MOKE [22, 197, 198]. The islands are monodomain magnets since for an island diameter of about 30 \AA a domain wall is energetically unfavorable [135, 136]. Further, they have a very narrow size distribution and their easy axis is out-of-plane.

Au(11,12,12) is a stable Au(111) vicinal surface with a terrace width of 58 \AA [197]. The (111) oriented terraces exhibit a reconstruction relieving part of the tensile surface stress by the insertion of additional Au atoms into the topmost layer. On Au(111), 23 Au surface atoms per unit cell sit on 22 bulk lattice sites leading to fcc and hcp stacked areas [199]. On the vicinal surface partial surface dislocations between these areas run perpendicular to the steps. Upon Co deposition, two atomic layer high Co islands nucleate at the crossing of a surface dislocation and the step edge, thus leading in an array of Co islands with a $58 \text{ \AA} \times 72 \text{ \AA}$ periodicity with good long range order as shown in Fig. 5.10 d) [197, 198]. To avoid coalescence, the sample was prepared by successively depositing 0.28 ML Co at $T = 130 \text{ K}$ followed by annealing at $T = 300 \text{ K}$ until a total coverage of 1.1 ML was reached [22]. The island size distribution obtained from STM images has a Gaussian shape with a mean size of $\langle s \rangle = 600$ atoms and a half width at half maximum of 27% of the mean size.

Our experimental setup allows to determine the island magnetic anisotropy energy (MAE) by two independent methods, namely by evaluating hysteresis loops acquired at different field angles α below the blocking temperature, and by measuring the temperature dependence of the zero-field susceptibility $\chi(T) = dM(T)/dH|_{H=0}$. We first focus on the first method. Fig. 5.10 a) shows a hysteresis loop for $\alpha = 0^\circ$ measured at $T = 75 \text{ K}$ with a sweep rate of 1.0 T/min . Fig. 5.10 b) represents the angular dependence of the magnetization at $B = 222 \text{ mT}$ (M_{222}) and of the remanent magnetization M_R taken from hysteresis loops recorded with a sweep rate of 1.0 T/min and a maximum field of $B = 222 \text{ mT}$ at 75 K . The M_R/M_{sat} versus α data clearly show that the easy axis is out-of-plane in agreement with earlier publications [200, 198, 22].

The magnetization can be modelled by taking into account non-equilibrium effects of a

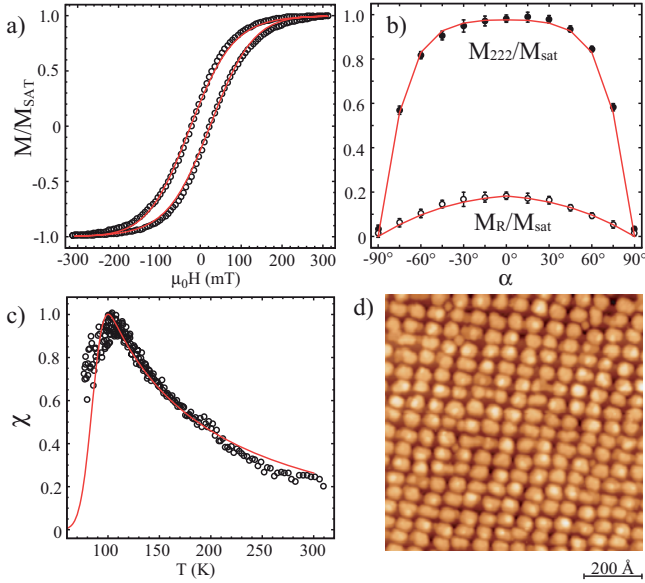


Figure 5.10: 1.1 ML Co/Au(11,12,12). a) Hysteresis loop measured at $T = 75$ K in polar geometry (average of 2 hysteresis loops). The error bar is smaller than the symbol size and therefore not shown. Hysteresis loops were simulated assuming the island MAE proportional to the island perimeter length (solid line). b) Magnetization at $B = 222$ mT (full circles) and remnant magnetization (empty circles) measured at $T = 75$ K. The solid curve represents M_{222} and M_R from simulated hysteresis curves assuming the island MAE proportional to the island perimeter length. c) $\chi(T)$ was measured applying a triangular field sweep with a sweep rate of 2 T/min and ± 5 mT amplitude (empty circles). The solid line represents the fit calculated assuming the island MAE proportional to the island perimeter length as in Ref. 22. d) STM image of the nano-island array ($V_t = -1.8$ V, $I_t = 0.2$ nA, $T = 200$ K).

thermally excited bi-stable system subjected to a time varying magnetic field [201]. Any hysteresis loop for an ensemble of non-interacting monodomain particles with uniaxial anisotropy represents mainly the asymmetry in the number of particles pointing up n_\uparrow and down n_\downarrow changing over time with the applied field. The time evolution of n_\uparrow can be expressed by the following master equation

$$\frac{dn_\uparrow}{dt} = -\kappa_{\uparrow\downarrow}n_\uparrow + \kappa_{\downarrow\uparrow}n_\downarrow, \quad (5.23)$$

were $\kappa_{\uparrow\downarrow}$ is the transition rate from n_{\uparrow} to n_{\downarrow} given by

$$\kappa_{\uparrow\downarrow} = \nu_0 e^{-\frac{E_{\uparrow\downarrow}}{k_B T}}. \quad (5.24)$$

ν_0 is the attempt frequency, $E_{\uparrow\downarrow}$ the barrier height, and k_B the Boltzman constant. The energy landscape of a single Co island of size s , magnetic moment per atom m , and anisotropy energy K is given by

$$E = K \sin^2 \alpha_0 - s m \mu_0 H \cos(\alpha_0 - \alpha) \quad (5.25)$$

where α_0 denotes the angle between \mathbf{m} and the easy axis, and α the angle of the magnetic field with respect to the easy axis which is in this case the surface normal. The master equation (5.23) has been integrated numerically using $\nu_0 = 10^{10}$ Hz and $m = 2.0 \mu_B/\text{Co}$ atom [29, 22], while taking into account the island size and perimeter length distribution experimentally determined from STM images. Assuming the magnetic anisotropy to be energy proportional to the perimeter length $K = p \cdot K_p$, where p is the number of perimeter atoms in the first and second layer [29, 22], produces the best fit of the experimental curves shown in Figs. 5.10 a) and b) with $K_p = 0.87 \pm 0.01$ meV/perimeter atom. This MAE value is compared with the one deduced from the second method using the temperature dependent susceptibility. $\chi(T)$, displayed in Fig. 5.10 c), was measured while cooling by applying a triangular field sweep with a sweep rate of 13 Hz and ± 5 mT amplitude. The solid line is calculated using equations (1) and (2) of Ref. 29 with $\nu_0 = 10^{10}$ Hz, $m = 2.0 \mu_B/\text{Co}$ atom, $K_p = 0.95 \pm 0.01$ meV/perimeter atom, and the experimental island size and perimeter length distributions.

The fact that both methods give very similar anisotropy energies is showing that the barrier for thermal magnetization reversal is identical to the one obtained by tilting the magnetization vector away from the easy axis by a torque. Therefore the transition state in thermal magnetization reversal is monodomain for the presented system. The K values compare very well to each other and with the ones found in earlier publications [22, 202, 198]. We also note that the curve in Fig. 5.10 c) is entirely reversible; the same curve is obtained when heating. In addition, the perfect agreement between fit and data for $T > T_b$ shows that the islands are non-interacting since the fit is based on the superposition principle, and interactions would give rise to a more shallow decay of χ [203]. As a final comment we note that we are far above the detection limit for 1.1 ML Co on Au. Taking into account that for small coverages the Kerr signal is proportional to the thickness (see Fig. 5.8 b) we estimate a detection limit for polar Kerr of about 0.1 ML. This corresponds to a mean island size of 50 atoms for the same island density as in the present experiment, provided that saturation magnetization is reached.

Chapter 6

Conclusions and Perspectives

The aim of this thesis was to contribute to the fundamental understanding of the magnetic properties of surface supported 3d transition metal atoms and one atomic layer thick epitaxial 3d transition metal films by quantifying the magneto-crystalline anisotropy energy, orbital and spin magnetic moments. For single Fe and Co atoms on 4d and 5d transition metal substrates we could establish a correlation between the spin-orbit coupling constant of the substrate and the strength of the MAE. For the monolayer films, a slightly different picture arises where the MAE is directly proportional to the size of the induced magnetic moment in the topmost substrate layer. These two facts raise the question whether it is the anisotropy of the orbital magnetic moment or rather the magnetic moment itself deciding about the strength of the MAE. This is reflected by the equation [160]

$$K = -\frac{1}{2}\xi \hat{\mathbf{S}} \cdot \Delta\mathbf{L} + \frac{7}{4}\frac{\xi^2}{E_{ex}}\hat{\mathbf{S}} \cdot \mathbf{D} \quad (6.1)$$

where $\hat{\mathbf{S}} = \mathbf{S}/|\mathbf{S}|$ is the spin quantization axis, $\Delta\mathbf{L}$ the anisotropy of the orbital moment (see equation (4.2.1)), \mathbf{D} the magnetic spin dipole moment which is linked to \mathbf{S} , and E_{ex} the effective exchange splitting between the majority and minority bands. For isolated adatoms an extended magnetization cloud in the substrate around the impurity is observed. As an example, for Fe/Pd(001) the cumulated induced spin moment is $4.5 \mu_B$ and the total induced orbital moment is as large as $0.57 \mu_B$ [31]. The orbital anisotropy of the induced moment is $\Delta L = 0.42$ which in turn yields an important contribution to the MAE/adatom via the spin-orbit coupling constant. For one atomic layer thick films the induced spin and orbital moment per adatom are smaller and consequently the contribution to the MAE is reduced. Moreover, the induced orbital moment is only $\sim 3\%$ of the induced spin moment in case of the adlayer (see table 4.2 and Ref. [28]) whereas it was 13% for the Fe single atom on Pd(001) meaning that the second term becomes more important. Due to the ξ dependence of equation (6.1), the use of a substrate with a high spin-orbit coupling, such as the 5d transition metals, is suitable in order to maximize the MAE.

Therefore, we investigated Fe and Co monolayers on Pt(111) as well as one atom thick bimetallic alloys of the two $3d$ transition metal elements on Pt(111). We found that all compositions have an easy axis out-of-plane, high M_{SAT} , and a large MAE with a maximum of 0.5 meV/atom at the equiatomic stoichiometry. This makes FeCo/Pt(111) a good candidates for magnetic storage. A single island of only 2400 atoms meets the stability criterion of 1.2 eV/bit while the writing field K/M_{SAT} remains in the technological limit [172]. The next step consists in implementing this knowledge in the fabrication of regular arrays of equally sized islands (monodisperse) with large MAE. A challenge for nanotechnology is the fabrication of such arrays providing islands with an identical environment (e.g. distances from their neighbors) and well-defined location. A promising way is self-assembly on template substrates. Examples are Co on vicinal Au(111), whose surface orientation allows to tune the cluster density (see Ref. [22] and chapter 5), Fe islands grown on a dislocation network of 2 ML Cu/Pt(111) [204], Ir islands on a graphene Moiré on Ir(111) [205], or FePd islands on $\text{Al}_2\text{O}_3/\text{Ni}_3\text{Al}(111)$ [79, 206].

Fe and Co single atoms on Al_2O_3 and Cu_2N reveal high magnetic anisotropy and atomic spin values making both systems playgrounds to study adatom-adatom interactions in homogeneous or heterogeneous structures of several atoms. It has been shown that Mn, Fe, and Co atoms can be arranged on the Cu_2N surface in dimers or longer chains leading to antiferromagnetic coupling of different strength for separations smaller than 10 Å between the adatoms [8, 105]. The square lattice of Cu_2N was found to be ideal for magnetic anisotropy measurements and to study coupling along easy and hard direction, but prevents building circular spin chains. On the Al_2O_3 surface, however, one could achieve to build rings with antiferromagnetic coupling which are prototypes for quantum computation [207]. In this sense structures of a few magnetic atoms on Cu_2N and Al_2O_3 can be compared with molecular magnets, early proposed for quantum computing [208, 209, 210]. Yet, the advantage is the way of arranging them in an atom by atom fashion and the possibility to address all atoms independently with an STM tip. Another interesting substrate may be the boron nitride (h-BN) nanomesh which has threefold symmetry. Grown on Rh(111) by chemical vapor deposition of borazine ($\text{B}_3\text{N}_3\text{H}_6$) at high temperature, a single atomic thick layer of h-BN is obtained which is isostructural to graphene [211, 212]. However, boron nitride is an insulator with a band gap of ~ 5 eV [213, 214] whereas graphene is metallic [215]. In addition, h-BN/Rh(111) forms a Moiré pattern with a lattice constant of 32.2 Å. The corrugation may allow to grow a regular array of clusters of a few atoms or larger islands as previously observed for Ir on graphene/Ir(111) [205]. First attempts with Co and Au failed on h-BH [70, 216], but other elements or deposition conditions may be successful. A regular array of monodisperse islands on insulating ultra-thin films may be also useful, when thinking of a prototype for magnetic random access memories where every spin valve has a size of only a few tens of Å² [217].

Appendix A

Spherical harmonics for s , p , and d orbitals

Spherical harmonics $Y_{l,m_l}(\vartheta, \varphi) = |l, m_l\rangle$ are eigenfunctions of the non-relativistic hamiltonian describing an electron in a scalar potential, i.e. the hydrogen atom. In table A.1 the explicit representation of the spherical harmonics is given. They are a basis set to represent the atomic orbitals (see table A.2). Including spin-orbit coupling in the hamiltonian leads to new relativistic basis states as shown in table A.3.

Y_{l,m_l}	$l = 0$	$l = 1$	$l = 2$
$m_l = 2$			$\sqrt{\frac{15}{32\pi}} \sin^2 \vartheta e^{2i\varphi}$
$m_l = 1$		$-\sqrt{\frac{3}{8\pi}} \sin \vartheta e^{i\varphi}$	$-\sqrt{\frac{15}{8\pi}} \sin \vartheta \cos \vartheta e^{i\varphi}$
$m_l = 0$	$\sqrt{\frac{1}{4\pi}}$	$\sqrt{\frac{3}{4\pi}} \cos \vartheta$	$\sqrt{\frac{5}{16\pi}} (\cos^2 \vartheta - 1)$
$m_l = -1$		$\sqrt{\frac{3}{8\pi}} \sin \vartheta e^{-i\varphi}$	$\sqrt{\frac{15}{8\pi}} \sin \vartheta \cos \vartheta e^{-i\varphi}$
$m_l = -2$			$\sqrt{\frac{15}{32\pi}} \sin^2 \vartheta e^{-2i\varphi}$

Table A.1: Spherical harmonics.




















s	$\sqrt{\frac{3}{4\pi}}$	$= Y_{0,0}$	
p_x	$\sqrt{\frac{3}{4\pi}} \frac{x}{r}$	$= \frac{1}{\sqrt{2}}(Y_{1,-1} - Y_{1,1})$	
p_y	$\sqrt{\frac{3}{4\pi}} \frac{y}{r}$	$= \frac{i}{\sqrt{2}}(Y_{1,-1} + Y_{1,1})$	
p_z	$\sqrt{\frac{3}{4\pi}} \frac{z}{r}$	$= Y_{1,0}$	
d_{xy}	$\sqrt{\frac{15}{4\pi}} \frac{xy}{r^2}$	$= \frac{i}{\sqrt{2}}(Y_{2,-2} - Y_{2,2})$	
d_{xz}	$\sqrt{\frac{15}{4\pi}} \frac{xz}{r^2}$	$= \frac{1}{\sqrt{2}}(Y_{2,-1} - Y_{2,1})$	
d_{yz}	$\sqrt{\frac{15}{4\pi}} \frac{yz}{r^2}$	$= \frac{i}{\sqrt{2}}(Y_{2,-1} + Y_{2,1})$	
$d_{x^2-y^2}$	$\sqrt{\frac{15}{16\pi}} \frac{(x^2-y^2)}{r^2}$	$= \frac{1}{\sqrt{2}}(Y_{2,-2} + Y_{2,2})$	
$d_{3z^2-r^2}$	$\sqrt{\frac{15}{16\pi}} \frac{(3z^2-r^2)}{r^2}$	$= Y_{2,0}$	

Table A.2: s , p , and d orbitals in terms of linear combinations of the spherical harmonics. In the last column the charge density, given by the angular wave functions, is plotted. The positive (negative) sign of the wavefunction is represented by the red (green) color.

j, m_j bases	m_l, m_s bases		
$P_{1/2}$	$m_j = +\frac{1}{2}$	$\frac{\sqrt{2}}{\sqrt{3}}Y_{1,1} \downarrow\rangle - \frac{1}{\sqrt{3}}Y_{1,0} \uparrow\rangle$	
	$m_j = -\frac{1}{2}$	$\frac{1}{\sqrt{3}}Y_{1,0} \downarrow\rangle - \frac{\sqrt{2}}{\sqrt{3}}Y_{1,-1} \uparrow\rangle$	
$P_{3/2}$	$m_j = +\frac{3}{2}$	$Y_{1,1} \uparrow\rangle$	
	$m_j = +\frac{1}{2}$	$\frac{1}{\sqrt{3}}Y_{1,1} \downarrow\rangle + \frac{\sqrt{2}}{\sqrt{3}}Y_{1,0} \uparrow\rangle$	
	$m_j = -\frac{1}{2}$	$\frac{1}{\sqrt{3}}Y_{1,-1} \uparrow\rangle + \frac{\sqrt{2}}{\sqrt{3}}Y_{1,0} \downarrow\rangle$	
	$m_j = -\frac{3}{2}$	$Y_{1,-1} \downarrow\rangle$	
$D_{3/2}$	$m_j = +\frac{3}{2}$	$\frac{2\sqrt{5}}{5}Y_{2,2} \downarrow\rangle - \frac{\sqrt{5}}{5}Y_{2,1} \uparrow\rangle$	
	$m_j = +\frac{1}{2}$	$\frac{\sqrt{15}}{5}Y_{2,1} \downarrow\rangle - \frac{\sqrt{10}}{5}Y_{2,0} \uparrow\rangle$	
	$m_j = -\frac{1}{2}$	$\frac{\sqrt{10}}{5}Y_{2,0} \downarrow\rangle - \frac{\sqrt{15}}{5}Y_{2,-1} \uparrow\rangle$	
	$m_j = -\frac{3}{2}$	$\frac{\sqrt{5}}{5}Y_{2,-1} \downarrow\rangle - \frac{2\sqrt{5}}{5}Y_{2,-2} \uparrow\rangle$	

Continued on next page







j, m_j bases	m_l, m_s bases	
$m_j = +\frac{5}{2}$	$Y_{2,2} \uparrow \rangle$	
$m_j = +\frac{3}{2}$	$\frac{\sqrt{5}}{5} Y_{2,2} \downarrow \rangle + \frac{2\sqrt{5}}{5} Y_{2,1} \uparrow \rangle$	
$m_j = +\frac{1}{2}$	$\frac{\sqrt{10}}{5} Y_{2,1} \downarrow \rangle + \frac{\sqrt{15}}{5} Y_{2,0} \uparrow \rangle$	
$m_j = -\frac{1}{2}$	$\frac{\sqrt{15}}{5} Y_{2,0} \downarrow \rangle + \frac{\sqrt{10}}{5} Y_{2,-1} \uparrow \rangle$	
$m_j = -\frac{3}{2}$	$\frac{\sqrt{5}}{5} Y_{2,-2} \downarrow \rangle + \frac{2\sqrt{5}}{5} Y_{2,-1} \uparrow \rangle$	
$m_j = -\frac{5}{2}$	$Y_{2,-2} \downarrow \rangle$	

Table A.3: Relativistic basis states $|j, m_j\rangle$ expressed in terms of spherical harmonics for $l = 1$ and $l = 2$. The spin direction is indicated by \uparrow ($m_s = 1/2$) and \downarrow ($m_s = -1/2$). In the last column the charge density, given by the angular wave functions, is plotted. The sign of the complex wavefunction is not represented.

Appendix B

Faraday Rotation

The Faraday effect of an isotropic transparent nonmagnetic body placed in an external magnetic field will be considered with the aim to derive (5.2). The propagation direction \mathbf{k} and the magnetic field \mathbf{H} are chosen along z . The electromagnetic wave is given by $\mathbf{E}(\mathbf{r}, t) = \mathbf{E}_0 e^{i(\mathbf{k}\mathbf{r} - \omega t)}$, the electric field vector \mathbf{E}_0 being along x . The dielectric permeability is

$$\epsilon = \epsilon_0 \epsilon_r \begin{pmatrix} 1 & ipH & 0 \\ -ipH & 1 & 0 \\ 0 & 0 & 1 \end{pmatrix}. \quad (\text{B.1})$$

Introducing $\mathbf{E}(\mathbf{r}, t)$ and ϵ in (5.6), while making use of $\mathbf{k} = \frac{\omega}{c} \mathbf{n}$ we obtain

$$\frac{\omega^2}{c^2} n^2 \mathbf{E}(\mathbf{r}, t) - \mu_0 \epsilon_0 \epsilon_r \omega^2 \begin{pmatrix} 1 & ipH & 0 \\ -ipH & 1 & 0 \\ 0 & 0 & 1 \end{pmatrix} \mathbf{E}(\mathbf{r}, t) = 0 \quad (\text{B.2})$$

We can rewrite the equation to find the eigenvalues and corresponding eigenvectors.

$$\begin{pmatrix} n^2 - \epsilon_r & -ipH\epsilon_r & 0 \\ ipH\epsilon_r & n^2 - \epsilon_r & 0 \\ 0 & 0 & n^2 - \epsilon_r \end{pmatrix} \mathbf{E}_0 = 0 \quad (\text{B.3})$$

The eigenvalues are

1. $n_+(H) = \frac{\sqrt{\epsilon_r}}{2}(1 + pH)$
2. $n_-(H) = \frac{\sqrt{\epsilon_r}}{2}(1 - pH)$

and the corresponding eigenvectors

$$1. \mathbf{E}_+ = \frac{1}{\sqrt{2}}(1, i, 0)$$

$$2. \mathbf{E}_- = \frac{1}{\sqrt{2}}(1, -i, 0)$$

showing that the propagation can be understood as a right circularly polarized wave \mathbf{E}_+ and left circularly polarized wave \mathbf{E}_- with different refractive indices. To derive the Faraday rotation the phase shift in between the right and left circularly polarized wave has to be calculated. The calculation can be accomplished at any x, y, t , for convenience $x = y = t = 0$. At $z = 0$ where the light ray enters the body we have

$$\mathbf{E}_+(0, 0, 0, 0) = \frac{E_0}{2}(1, i, 0) \quad (\text{B.4})$$

$$\mathbf{E}_-(0, 0, 0, 0) = \frac{E_0}{2}(1, -i, 0) \quad (\text{B.5})$$

such that $\mathbf{E}_+ + \mathbf{E}_-$ is along x . At $z = l$ where the light ray leaves the body we have

$$\mathbf{E}_+(0, 0, l, 0) = \frac{E_0}{2}(1, i, 0)e^{i\frac{\omega}{c}n_+(H)l} \quad (\text{B.6})$$

$$\mathbf{E}_-(0, 0, l, 0) = \frac{E_0}{2}(1, -i, 0)e^{i\frac{\omega}{c}n_-(H)l} \quad (\text{B.7})$$

Taking the sum of both

$$\mathbf{E}(0, 0, l, 0) = \frac{E_0}{2} \begin{pmatrix} (e^{i\frac{\omega}{c}n_+(H)l} + e^{i\frac{\omega}{c}n_-(H)l}) \\ i(e^{i\frac{\omega}{c}n_+(H)l} - e^{i\frac{\omega}{c}n_-(H)l}) \\ 0 \end{pmatrix} = E_0 e^{i\frac{\omega}{c}\sqrt{\epsilon_r}l} \begin{pmatrix} \cos \Theta_F \\ \sin \Theta_F \\ 0 \end{pmatrix} \quad (\text{B.8})$$

where $\Theta_F = \frac{\omega l}{2c}(n_+(H) - n_-(H))$. The proportionality constant $e^{i\frac{\omega}{c}\sqrt{\epsilon_r}l}$ describes the extinction of the amplitude via the imaginary part of the complex index of refraction n . The penetration depth Δl is defined as the depth at which the intensity of the radiation inside the material falls to $1/e$ of the original value at the surface. We obtain

$$\Delta l = \frac{\lambda}{2\pi \text{Im}(n)}. \quad (\text{B.9})$$

Bibliography

- [1] P. Gambardella, S. Rusponi, M. Veronese, S. S. Dhesi, C. Grazioli, A. Dallmeyer, I. Cabria, R. Zeller, P. H. Dederichs, K. Kern, C. Carbone, and H. Brune, *Giant Magnetic Anisotropy of Single Cobalt Atoms and Nanoparticles*, *Science* **300**, 1130 (2003).
- [2] B. Lazarovits, L. Szunyogh, and P. Weinberger, *Magnetic properties of finite Co chains on Pt(111)*, *Phys. Rev. B* **67**, 024415 (2003).
- [3] S. Bornemann, J. Minár, J. B. Staunton, J. Honolka, A. Enders, K. Kern, and H. Ebert, *Magnetic anisotropy of deposited transition metal clusters*, *Eur. Phys. J. D* **45**, 529 (2007).
- [4] A. Mosca Conte, S. Fabris, and S. Baroni, *Properties of Pt-supported Co nanomagnets from relativistic density functional theory calculations*, *Phys. Rev. B* **78**, 014416 (2008).
- [5] C. Etz, J. Zabloudil, P. Weinberger, and E. Y. Vedmedenko, *Magnetic properties of single atoms of Fe and Co on Ir(111) and Pt(111)*, *Phys. Rev. B* **77**, 184425 (2008).
- [6] T. Balashov, T. Schuh, A. F. Takacs, A. Ernst, S. Ostanin, J. Henk, I. Mertig, P. Bruno, T. Miyamachi, S. Suga, and W. Wulfhekel, *Magnetic Anisotropy and Magnetization Dynamics of Individual Atoms and Clusters of Fe and Co on Pt(111)*, arXiv/0903.3337 (2009).
- [7] A. J. Heinrich, J. A. Gupta, C. P. Lutz, and D. M. Eigler, *Single-Atom Spin-Flip Spectroscopy*, *Science* **306**, 466 (2004).
- [8] C. F. Hirjibehedin, C. P. Lutz, and A. J. Heinrich, *Spin Coupling in Engineered Atomic Structures*, *Science* **312**, 1021 (2006).
- [9] C.F. Hirjibehedin, C.-Y. Lin, A.F. Otte, M. Ternes, C.P. Lutz, B.A. Jones, and A.J. Heinrich, *Large Magnetic Anisotropy of a Single Atomic Spin Embedded in a Surface Molecular Network*, *Science* **317**, 1199 (2007).

- [10] F. Meier, L. Zhou, J. Wiebe, and R. Wiesendanger, *Revealing Magnetic Interactions from Single-Atom Magnetization Curves*, *Science* **320**, 82 (2008).
- [11] P. Gambardella, S. Stepanow, A. Dmitriev, J. Honolka, F. M. F. de Groot, M. Lin-genfelder, S. S. Guptaand, D. D. Sarma, P. Bencok, S. Stanescu, S. Clair, S. Pons, A. P. Seitsonen, H. Brune, J. V. Barth, and K. Kern, *Supramolecular control of the magnetic anisotropy in two-dimensional high-spin Fe arrays at a metal interface*, *Nat. Mater.* **9**, 189 (2009).
- [12] G. Schütz, W. Wagner, W. Wilhelm, P. Kienle, R. Zeller, R. Frahm, and G. Materlik, *Absorption of circularly polarized x rays in iron*, *Phys. Rev. Lett.* **58**, 737 (1987).
- [13] C. T. Chen, N. V. Smith, and F. Sette, *Exchange, spin-orbit, and correlation effects in the soft-x-ray magnetic-circular-dichroism spectrum of nickel*, *Phys. Rev. B* **43**, 6785 (1991).
- [14] Y. Wu, J. Stöhr, B. D. Hermsmeier, M. G. Samant, and D. Weller, *Enhanced orbital magnetic moment on Co atoms in Co/Pd multilayers: A magnetic circular x-ray dichroism study*, *Phys. Rev. Lett.* **69**, 2307 (1992).
- [15] C. T. Chen, Y. U. Idzerda, H.-J. Lin, N. V. Smith, G. Meigs, E. Chaban, G. H. Ho, E. Pellegrin, and F. Sette, *Experimental Confirmation of the X-Ray Magnetic Circular Dichroism Sum Rules for Iron and Cobalt*, *Phys. Rev. Lett.* **75**, 152 (1995).
- [16] D. Weller, J. Stöhr, R. Nakajima, A. Carl, M. G. Samant, C. Chappert, R. Mégy, P. Beauvillain, P. Veillet, and G. A. Held, *Microscopic Origin of Magnetic Anisotropy in Au/Co/Au Probed with X-Ray Magnetic Circular Dichroism*, *Phys. Rev. Lett.* **75**, 3752 (1995).
- [17] H. Brune and P. Gambardella, *Magnetism of individual atoms adsorbed on surfaces*, *Surf. Sci.* **603**, 1812 – 1830 (2009).
- [18] B. T. Thole, P. Carra, F. Sette, and G. van der Laan, *X-ray circular dichroism as a probe of orbital magnetization*, *Phys. Rev. Lett.* **68**, 1943 (1992).
- [19] P. Carra, B. T. Thole, M. Altarelli, and X. Wang, *X-ray circular dichroism and local magnetic fields*, *Phys. Rev. Lett.* **70**, 694 (1993).
- [20] G. van der Laan, *Microscopic origin of magnetocrystalline anisotropy in transition metal thin films*, *J. Phys.- Condens. Matter* **10**, 3239 (1998).
- [21] P. Bruno, *Tight-binding approach to the orbital magnetic moment and magnetocrystalline anisotropy of transition-metal monolayers*, *Phys. Rev. B* **39**, 865 (1989).

- [22] N. Weiss, T. Cren, M. Epple, S. Rusponi, G. Baudot, S. Rohart, A. Tejada, V. Repain, S. Rousset, P. Ohresser, F. Scheurer, P. Bencok, and H. Brune, *Uniform Magnetic Properties for an Ultrahigh-Density Lattice of Noninteracting Co Nanostructures*, Phys. Rev. Lett. **95**, 157204 (2005).
- [23] M. Bode, O. Pietzsch, A. Kubetzka, and R. Wiesendanger, *Shape-Dependent Thermal Switching Behavior of Superparamagnetic Nanoislands*, Phys. Rev. Lett. **92**, 067201 (2004).
- [24] Y. Yayon, V. W. Brar, L. Senapati, S. C. Erwin, and M. F. Crommie, *Observing Spin Polarization of Individual Magnetic Adatoms*, Phys. Rev. Lett. **99**, 067202 (2007).
- [25] D. Spišák and J. Hafner, *Structural, magnetic, and chemical properties of thin Fe films grown on Rh(100) surfaces investigated with density functional theory*, Phys. Rev. B **73**, 155428 (2006).
- [26] F. El Gabaly, S. Gallego, C. Muñoz, L. Szunyogh, P. Weinberger, C. Klein, A. K. Schmid, K. F. McCarty, and J. de la Figuera, *Imaging Spin-Reorientation Transitions in Consecutive Atomic Co Layers on Ru(0001)*, Phys. Rev. Lett. **96**, 147202 (2006).
- [27] S. I. Csiszar, M. W. Haverkort, Z. Hu, A. Tanaka, H. H. Hsieh, H.-J. Lin, C. T. Chen, T. Hibma, and L. H. Tjeng, *Controlling Orbital Moment and Spin Orientation in CoO Layers by Strain*, Phys. Rev. Lett. **95**, 187205 (2005).
- [28] G. Moulas, A. Lehnert, S. Rusponi, J. Zabloudil, C. Etz, S. Ouazi, M. Etzkorn, P. Bencok, P. Gambardella, P. Weinberger, and H. Brune, *High magnetic moments and anisotropies for Fe_xCo_{1-x} monolayers on Pt(111)*, Phys. Rev. B **78**, 214424 (2008).
- [29] S. Rusponi, T. Cren, N. Weiss, M. Epple, P. Buluscek, L. Claude, and H. Brune, *The remarkable difference between surface and step atoms in the magnetic anisotropy of two-dimensional nanostructures*, Nat. Mater. **3**, 546 (2003).
- [30] G. Moulas, Ph.D. thesis, no. 4231, Ecole Polytechnique Fédérale de Lausanne, 2008.
- [31] J. Hafner and D. Spišák, *Morphology and magnetism of Fe_n clusters ($n = 1-9$) supported on a Pd(001) substrate*, Phys. Rev. B **76**, 094420 (2007).
- [32] A. F. Otte, M. Ternes, K. von Bergmann, S. Loth, H. Brune, C. P. Lutz, C. F. Hirjibehedin, and A. J. Heinrich, *The role of magnetic anisotropy in the Kondo effect*, Nat. Phys. **4**, 847 (2008).

- [33] P. Bruno, G. Bayreuther, P. Beauvillain, C. Chappert, G. Lugert, D. Renard, J. P. Renard, and J. Seiden, *Hysteresis properties of ultrathin ferromagnetic films*, J. Appl. Phys. **68**, 5759 (1990).
- [34] T. Burkert, L. Nordström, O. Eriksson, and O. Heinonen, *Giant Magnetic Anisotropy in Tetragonal FeCo Alloys*, Phys. Rev. Lett. **93**, 027203 (2004).
- [35] F. Yildiz, F. Luo, C. Tieg, R. M. Abrudan, X. L. Fu, A. Winkelmann, M. Przybylski, and J. Kirschner, *Strongly Enhanced Orbital Moment by Reduced Lattice Symmetry and Varying Composition of $Fe_{1-x}Co_x$ Alloy Films*, Phys. Rev. Lett. **100**, 037205 (2008).
- [36] C. Cohen-Tannoudji, B. Diu, and F. Laloë, *Mécanique quantique*, Hermann Éditeurs des Sciences et des Arts, Paris, France, 1986.
- [37] C. Brouder, *Angular dependence of X-ray absorption spectra*, J. Phys.- Condens. Matter **2**, 701 (1990).
- [38] J. J. Sakurai, *Modern Quantum Mechanics*, Addison-Wesley Publishing Company, 1995.
- [39] J. L. Erskine and E. A. Stern, *Calculation of the M_{23} magneto-optical absorption spectrum of ferromagnetic nickel*, Phys. Rev. B **12**, 5016 (1975).
- [40] M. M. Sigalas and D. A. Papaconstantopoulos, *Calculations of the total energy, electron-phonon interaction, and Stoner parameter for metals*, Phys. Rev. B **50**, 7255 (1994).
- [41] A. Goldoni, A. Baraldi, G. Comelli, S. Lizzit, and G. Paolucci, *Experimental Evidence of Magnetic Ordering at the Rh(100) Surface*, Phys. Rev. Lett. **82**, 3156 (1999).
- [42] T. Lin, M. A. Tomaz, M. M. Schwickert, and G. R. Harp, *Structure and magnetic properties of Ru/Fe(001) multilayers*, Phys. Rev. B **58**, 862 (1998).
- [43] H. Ebert, *Magneto-optical effects in transition metal systems*, Rep. Prog. Phys. **59**, 1665 (1996).
- [44] N. V. Smith, C. T. Chen, F. Sette, and L. F. Mattheiss, *Relativistic tight-binding calculations of x-ray absorption and magnetic circular dichroism at the L_2 and L_3 edges of nickel and iron*, Phys. Rev. B **46**, 1023 (1992).
- [45] N. Ashcroft and D. Mermin, *Solid State Physics*, London, 2001.

- [46] J. Stöhr and H.C. Siegmann, *Magnetism, From Fundamentals to Nanoscale Dynamics*, Solid-State Sciences, vol. 152, Springer, Heidelberg, 2006.
- [47] F. M. F. de Groot, *X-ray absorption and dichroism of transition metals and their compounds*, J. Electron Spectrosc. **67**, 529 (1994).
- [48] V. N. Antonov, A. P. Shpak, and A. N. Yaresko, *X-ray magnetic circular dichroism in d and f ferromagnetic materials: recent theoretical progress. Part I (Review Article)*, Low Temp. Phys. **34**, 1 (2008).
- [49] V. N. Antonov, A. P. Shpak, and A. N. Yaresko, *X-ray magnetic circular dichroism in d and f ferromagnetic materials: recent theoretical progress. Part II (Review Article)*, Low Temp. Phys. **34**, 79 (2008).
- [50] T. Jo and G. A. Sawatzky, *Ground state of ferromagnetic nickel and magnetic circular dichroism in Ni 2p core x-ray-absorption spectroscopy*, Phys. Rev. B **43**, 8771 (1991).
- [51] F. de Groot, *Multiplet effects in X-ray spectroscopy*, Coordin. Chem. Rev. **249**, 31 (2005).
- [52] J. Stöhr and H. König, *Determination of Spin- and Orbital-Moment Anisotropies in Transition Metals by Angle-Dependent X-Ray Magnetic Circular Dichroism*, Phys. Rev. Lett. **75**, 3748 (1995).
- [53] G. van der Laan, *Line shape of 2p magnetic-x-ray-dichroism spectra in 3d metallic systems*, Phys. Rev. B **55**, 8086 (1997).
- [54] M. M. Schwickert, G. Y. Guo, M. A. Tomaz, W. L. O'Brien, and G. R. Harp, *X-ray magnetic linear dichroism in absorption at the L edge of metallic Co, Fe, Cr, and V*, Phys. Rev. B **58**, R4289 (1998).
- [55] G. van der Laan, *Magnetic Linear X-Ray Dichroism as a Probe of the Magnetocrystalline Anisotropy*, Phys. Rev. Lett. **82**, 640 (1999).
- [56] S. S. Dhesi, G. van der Laan, E. Dudzik, and A. B. Shick, *Anisotropic Spin-Orbit Coupling and Magnetocrystalline Anisotropy in Vicinal Co Films*, Phys. Rev. Lett. **87**, 067201 (2001).
- [57] I. M. L. Billas, A. Châtelain, and W. A. de Heer, *Magnetism from the Atom to the Bulk in Iron, Cobalt, and Nickel Clusters*, Science **265**, 1682 (1994).
- [58] S. E. Apsel, J. W. Emmert, J. Deng, and L. A. Bloomfield, *Surface-Enhanced Magnetism in Nickel Clusters*, Phys. Rev. Lett. **76**, 1441 (1996).

- [59] F. W. Payne, Wei Jiang, J. W. Emmert, Jun Deng, and L. A. Bloomfield, *Magnetic structure of free cobalt clusters studied with Stern-Gerlach deflection experiments*, Physical Review B (Condensed Matter and Materials Physics) **75**, 094431 (2007).
- [60] B. V. Reddy, S. N. Khanna, and B. I. Dunlap, *Giant magnetic moments in 4d clusters*, Phys. Rev. Lett. **70**, 3323 (1993).
- [61] A. J. Cox, J. G. Louderback, and L. A. Bloomfield, *Experimental observation of magnetism in rhodium clusters*, Phys. Rev. Lett. **71**, 923 (1993).
- [62] A. J. Cox, J. G. Louderback, S. E. Apsel, and L. A. Bloomfield, *Magnetism in 4d-transition metal clusters*, Phys. Rev. B **49**, 12295 (1994).
- [63] P. Gambardella, S. S. Dhesi, S. Gardonio, C. Grazioli, P. Ohresser, and C. Carbone, *Localized Magnetic States of Fe, Co, and Ni Impurities on Alkali Metal Films*, Phys. Rev. Lett. **88**, 047202 (2002).
- [64] L. Claude, Ph.D. thesis, no. 3276, Ecole Polytechnique Fédérale de Lausanne, 2005.
- [65] A. Rosenhahn, J. Schneider, J. Kandler, C. Becker, and K. Wandelt, *Interaction of oxygen with Ni₃Al(111) at 300 K and 1000 K*, Surf. Sci. **433-435**, 705 (1999).
- [66] C. D. Ruggiero, T. Choi, and J. A. Gupta, *Tunneling spectroscopy of ultrathin insulating films: CuN on Cu(100)*, Appl. Phys. Lett. **91**, 253106 (2007).
- [67] R. Sessoli, D. Gatteschi, A. Caneschi, and M. A. Novak, *Magnetic bistability in a metal-ion cluster*, Nature **365**, 141 (1993).
- [68] H. Brune, *Handbook of Surface Science*, vol. 3, ch. 15, p. 761, Elsevier, Amsterdam, 2008.
- [69] M. El Ouali, *Kinetic Monte-Carlo Simulation of Diffusion and Nucleation Phenomena of the (111) Surface of an fcc Crystal*, 2003.
- [70] P. Bulushek, Ph.D. thesis, no. 3944, Ecole Polytechnique Fédérale de Lausanne, 2007.
- [71] H. Brune, G. S. Bales, J. Jacobsen, C. Boragno, and K. Kern, *Measuring surface diffusion from nucleation island densities*, Phys. Rev. B **60**, 5991 (1999).
- [72] P. Gambardella, A. Dallmeyer, K. Maiti, M. C. Malagoli, W. Eberhardt, K. Kern, and C. Carbone, *Ferromagnetism in one-dimensional monatomic metal chains*, Nature **416**, 301 (2002).

- [73] I. Levin and D. Brandon, *Metastable Alumina Polymorphs: Crystal Structures and Transition Sequences*, J. Am. Ceram. Soc. **81**, 1995 (1998).
- [74] Ch. Täschner, B. Ljungberg, I. Endler, and A. Leonhardt, *Deposition of hard crystalline Al_2O_3 coatings by pulsed d.c. PACVD*, Surf. Coat. Tech. **116-119**, 891 – 897 (1999).
- [75] G. Alcala, P. Skeldon, G. E. Thompson, A. B. Mann, H. Habazaki, and K. Shimizu, *Mechanical properties of amorphous anodic alumina and tantalum films using nanoindentation*, Nanotechnology **13**, 451 (2002).
- [76] Z. R. Ismagilov, R. A. Shkrabina, and N. A. Koryabkina, *New technology for production of spherical alumina supports for fluidized bed combustion*, Catal. Today **47**, 51 (1999).
- [77] U. Bardi, A. Atrei, and G. Rovida, *Initial stages of oxidation of the Ni_3Al alloy: structure and composition of the aluminum oxide overlayer studied by XPS, LEIS and LEED*, Surf. Sci. **268**, 87 (1992).
- [78] C. Becker, J. Kandler, H. Raaf, R. Linke, T. Pelster, M. Dräger, M. Tanemura, and K. Wandelt, *Oxygen adsorption and oxide formation on $Ni_3Al(111)$* , J. Vac. Sci. Technol. A **16**, 1000 (1998).
- [79] M. Schmid, G. Kresse, A. Buchsbaum, E. Napetschnig, S. Gritschneider, M. Reichling, and P. Varga, *Nanotemplate with Holes: Ultrathin Alumina on $Ni_3Al(111)$* , Phys. Rev. Lett. **99**, 196104 (2007).
- [80] T. Maroutian, S. Degen, C. Becker, K. Wandelt, and R. Berndt, *Superstructures and coincidences of a thin oxide film on a metallic substrate: A STM study*, Phys. Rev. B **68**, 155414 (2003).
- [81] A. Lehnert, A. Krupski, S. Degen, K. Franke, R. Decker, S. Rusponi, M. Kralj, C. Becker, H. Brune, and K. Wandelt, *Nucleation of ordered Fe islands on $Al_2O_3/Ni_3Al(111)$* , Surf. Sci. **600**, 1804 (2006).
- [82] F. R. de Boer, C. J. Schinkel, J. Biesterbos, and S. Proost, *Exchange-Enhanced Paramagnetism and Weak Ferromagnetism in the Ni_3Al and Ni_3Ga Phases; Giant Moment Inducement in Fe-Doped Ni_3Ga* , J. Appl. Phys. **40**, 1049 (1969).
- [83] S. K. Dhar, K. A. Gschneidner, L. L. Miller, and D. C. Johnston, *Low-temperature behavior of Ni_3Al alloys near the spin-fluctuator-ferromagnet phase boundary*, Phys. Rev. B **40**, 11488 (1989).

- [84] R. Wu and A. J. Freeman, *Limitation of the Magnetic-Circular-Dichroism Spin Sum Rule for Transition Metals and Importance of the Magnetic Dipole Term*, Phys. Rev. Lett. **73**, 1994 (1994).
- [85] G. van der Laan and B. T. Thole, *Strong magnetic x-ray dichroism in 2p absorption spectra of 3d transition-metal ions*, Phys. Rev. B **43**, 13401 (1991).
- [86] H.-J. Kim, J.-H. Park, and E. Vescovo, *Oxidation of the Fe(110) surface: An Fe₃O₄(111)/Fe(110) bilayer*, Phys. Rev. B **61**, 15284 (2000).
- [87] J. Chen, D. J. Huang, A. Tanaka, C. F. Chang, S. C. Chung, W. B. Wu, and C. T. Chen, *Magnetic circular dichroism in Fe 2p resonant photoemission of magnetite*, Phys. Rev. B **69**, 085107 (2004).
- [88] C. I. Pearce, C. M. B. Henderson, R. A. D. Patrick, G. van der Laan, and D. J. Vaughan, *Direct determination of cation site occupancies in natural ferrite spinels by L_{2,3} X-ray absorption spectroscopy and X-ray magnetic circular dichroism*, Am. Mineral. **91**, 880 (2006).
- [89] J.-Y. Kim, T. Y. Koo, and J.-H. Park, *Orbital and Bonding Anisotropy in a Half-Filled GaFeO₃ Magnetolectric Ferrimagnet*, Phys. Rev. Lett. **96**, 047205 (2006).
- [90] B. T. Thole and G. van der Laan, *Branching ratio in x-ray absorption spectroscopy*, Phys. Rev. B **38**, 3158 (1988).
- [91] F. M. F. de Groot, M. Abbate, J. van Elp, G. A. Sawatzky, Y. J. Ma, C. T. Chen, and F. Sette, *Oxygen 1s and cobalt 2p X-ray absorption of cobalt oxides*, J. Phys.: Condens. Matter **5**, 2277 (1993).
- [92] M. Kulawik, N. Nilius, and H.-J. Freund, *Influence of the Metal Substrate on the Adsorption Properties of Thin Oxide Layers: Au Atoms on a Thin Alumina Film on NiAl(001)*, Phys. Rev. Lett. **96**, 036103 (2006).
- [93] We use the KMC simulation program developed by M. El Ouali and extended by P. Bulschenk. The code treats a hexagonal close packed surface and allows only the occupation of fcc sites. We assume that the dimer is stable and neglect desorption and edge- or corner-diffusion.
- [94] J. A. Venables, G. D. T. Spiller, and M. Hanbücken, *Nucleation and growth of thin films*, Rep. Prog. Phys. **47**, 399 (1984).
- [95] H. Brune, H. Röder, C. Boragno, and K. Kern, *Microscopic View of Nucleation on Surfaces*, Phys. Rev. Lett. **73**, 1998 (1994).

- [96] O. Renault, N. Barrett, A. Bailly, L.F. Zagonel, D. Mariolle, J.C. Cezar, N.B. Brookes, K. Winkler, B. Krömker, and D. Funnemann, *Energy-filtered XPEEM with NanoESCA using synchrotron and laboratory X-ray sources: Principles and first demonstrated results*, Surf. Sci. **601**, 4727 (2007).
- [97] H. Shiroishi, T. Oda, I. Hamada, and N. Fujima, *Structure and magnetism on iron oxide clusters Fe_nO_m ($n = 1-5$): Calculation from first principles*, Eur. Phys. J. D **24**, 85 (2003).
- [98] J. B. Birks, *The Properties of Ferromagnetic Compounds at Centimetre Wavelengths*, Proc. Phys. Soc. **63**, 65 (1950).
- [99] D. M. Borsa and D. O. Boerma, *Growth, structural and optical properties of Cu_3N films*, Surf. Sci. **548**, 95 (2004).
- [100] F.M. Leibsle, S.S. Dhesi, S.D. Barrett, and A.W. Robinson, *STM observations of $Cu(100)$ - $c(2 \times 2)N$ surfaces: evidence for attractive interactions and an incommensurate $c(2 \times 2)$ structure*, Surf. Sci. **317**, 309 (1994).
- [101] H. Ellmer, V. Repain, S. Rousset, B. Croset, M. Sotto, and P. Zeppenfeld, Surf. Sci. **476**, 95 (2001).
- [102] T. Choi, C. D. Ruggiero, and J. A. Gupta, *Incommensurability and atomic structure of $c(2 \times 2)N/Cu(100)$: A scanning tunneling microscopy study*, Phys. Rev. B **78**, 035430 (2008).
- [103] H. Brune, *Superlattices of Atoms, Molecules, and Islands*, Single Molecules at Surfaces (F. Rosei, P. Grütter, and W. Hofer, eds.), Springer, New York, 2006.
- [104] B. Croset, Y. Girard, G. Prévot, M. Sotto, Y. Garreau, R. Pinchaux, and M. Sauvage-Simkin, *Measuring Surface Stress Discontinuities in Self-Organized Systems with X Rays*, Phys. Rev. Lett. **88**, 056103 (2002).
- [105] A. F. Otte, *Magnetism of a Single Atom*, Ph.D. thesis, Universiteit Leiden, 2008.
- [106] S. Frota-Pessôa, *Magnetic behavior of 3d impurities in Cu, Ag, and Au: First-principles calculations of orbital moments*, Phys. Rev. B **69**, 104401 (2004).
- [107] J. T. Lau, J. Rittmann, V. Zamudio-Bayer, M. Vogel, K. Hirsch, Ph. Klar, F. Lofink, T. Möller, and B. v. Issendorff, *Size Dependence of $L_{2,3}$ Branching Ratio and $2p$ Core-Hole Screening in X-Ray Absorption of Metal Clusters*, Phys. Rev. Lett. **101**, 153401 (2008).
- [108] A. Heinrich, private communication.

- [109] N. Knorr, M. A. Schneider, L. Diekhöner, P. Wahl, and K. Kern, *Kondo Effect of Single Co Adatoms on Cu Surfaces*, Phys. Rev. Lett. **88**, 096804 (2002).
- [110] M. Ternes, Ph.D. thesis, no. 3465, Ecole Polytechnique Fédérale de Lausanne, 2006.
- [111] M. Ternes, A. J. Heinrich, and W.-D. Schneider, *Spectroscopic manifestations of the Kondo effect on single adatoms*, J. Phys.: Condens. Matter **21**, 053001 (2009).
- [112] L. Bürgi, Ph.D. thesis, no. 2033, Ecole Polytechnique Fédérale de Lausanne, 1999.
- [113] M. L. Plumer, J. van Ek, and D. Weller, *The Physics of Ultra-High-Density Magnetic Recording*, Series in Surface Science, vol. 41, Springer, Berlin, 2001.
- [114] D. Sander, S. Ouazi, A. Enders, Th. Gutjahr-Loser, V. S. Stepanyuk, D. I. Bazhanov, and J. Kirschner, *Stress, strain and magnetostriction in epitaxial films*, J. Phys.- Condens. Matter **14**, 4165 (2002).
- [115] B. M. Lairson and B. M. Clemens, *Enhanced magneto-optic Kerr rotation in epitaxial PtFe(001) and PtCo(001) thin films*, Appl. Phys. Lett. **63**, 1438–1440 (1993).
- [116] S. Sun, C. B. Murray, D. Weller, L. Folks, and A. Moser, *Monodisperse FePt Nanoparticles and Ferromagnetic FePt Nanocrystal Superlattices*, Science **287**, 1989 (2000).
- [117] C. Antoniak, J. Lindner, M. Spasova, D. Sudfeld, M. Acet, M. Farle, K. Fauth, U. Wiedwald, H.-G. Boyen, P. Ziemann, F. Wilhelm, A. Rogalev, and S. Sun, *Enhanced Orbital Magnetism in Fe₅₀Pt₅₀ Nanoparticles*, Phys. Rev. Lett. **97**, 117201 (2006).
- [118] A. Winkelmann, M. Przybylski, F. Luo, Y. Shi, and J. Barthel, *Perpendicular Magnetic Anisotropy Induced by Tetragonal Distortion of FeCo Alloy Films Grown on Pd(001)*, Phys. Rev. Lett. **96**, 257205 (2006).
- [119] L. Pauling, *The Nature of the Interatomic Forces in Metals*, Phys. Rev. **54**, 899 (1938).
- [120] R. C. Hall, *Magnetic Anisotropy and Magnetostriction of Ordered and Disordered Cobalt-Iron Alloys*, J. Appl. Phys. **31**, S157–S158 (1960).
- [121] *Opposite Magnetization Axis for Fe and Co Overlayers on Rh(111)*, in preparation for PRB, Experiment: A. Lehnert, S. Rusponi, G. Moulas, M. Etzkorn, P. Bencok, P. Gambardella, and H. Brune, Theory: S. Denmler and J. Hafner.
- [122] M. Giovannini, Ph.D. thesis, no. 2169, Ecole Polytechnique Fédérale de Lausanne, 2000.

- [123] H. Brune, *Microscopic view of epitaxial metal growth: Nucleation and aggregation*, Surf. Sci. Rep. **31**, 125 (1998).
- [124] K. Bromann, H. Brune, M. Giovannini, and K. Kern, *Pseudomorphic growth induced by chemical adatom potential*, Surf. Sci. **388**, L1107 (1997).
- [125] T. Cren, S. Rusponi, N. Weiss, M. Epple, and H. Brune, *Oxidation Induced Enhanced Magnetic Susceptibility of Co Islands on Pt(111)*, J. Phys. Chem. B **108**, 14685 (2004).
- [126] D. Repetto, T. Y. Lee, S. Rusponi, J. Honolka, K. Kuhnke, V. Sessi, U. Starke, H. Brune, P. Gambardella, C. Carbone, A. Enders, and K. Kern, *Structure and magnetism of atomically thin Fe layers on flat and vicinal Pt surfaces*, Phys. Rev. B **74**, 054408 (2006).
- [127] E. Lundgren, B. Stanka, M. Schmid, and P. Varga, *Thin films of Co on Pt(111): Strain relaxation and growth*, Phys. Rev. B **62**, 2843 (2000).
- [128] M. Przybylski, L. Yan, J. Żukrowski, M. Nyvlt, Y. Shi, A. Winkelmann, J. Barthel, M. Waśniowska, and J. Kirschner, *Topology-dependent interface contribution to magneto-optical response from ultrathin Co films grown on the (001), (110), and (111) surfaces of Pd*, Phys. Rev. B **73**, 085413 (2006).
- [129] S. Ferrer, J. Alvarez, E. Lundgren, X. Torrelles, P. Fajardo, and F. Boscherini, *Surface x-ray diffraction from Co/Pt(111) ultrathin films and alloys: Structure and magnetism*, Phys. Rev. B **56**, 9848–9857 (1997).
- [130] O. Robach, C. Quiros, P. Steadman, K. F. Peters, E. Lundgren, J. Alvarez, H. Isern, and S. Ferrer, *Magnetic anisotropy of ultrathin cobalt films on Pt(111) investigated with x-ray diffraction: Effect of atomic mixing at the interface*, Phys. Rev. B **65**, 054423 (2002).
- [131] H. Bulou and C. Massobrio, *Mechanisms of exchange diffusion on fcc(111) transition metal surfaces*, Phys. Rev. B **72**, 205427 (2005).
- [132] Y. Xie and J. A. Blackman, *Theory of enhanced magnetic anisotropy induced by Pt adatoms on two-dimensional Co clusters supported on a Pt(111) substrate*, Phys. Rev. B **74**, 054401 (2006).
- [133] H. H. Hamdeh, B. Fultz, and D. H. Pearson, *Mössbauer spectrometry study of the hyperfine fields and electronic structure of Fe-Co alloys*, Phys. Rev. B **39**, 11233 (1989).

- [134] J. G. Amar, F. Family, and P.-M. Lam, *Dynamic scaling of the island-size distribution and percolation in a model of submonolayer molecular-beam epitaxy*, Phys. Rev. B **50**, 8781 (1994).
- [135] R. Skomski, H.-P. Oepen, and J. Kirschner, *Micromagnetics of ultrathin films with perpendicular magnetic anisotropy*, Phys. Rev. B **58**, 3223 (1998).
- [136] A. Vaterlaus, O. Portmann, C. Stamm, and D. Pescia, *Domain configuration in perpendicularly magnetized atomically thin iron particles*, J. Magn. Magn. Mater. **272-276**, 1137 (2004).
- [137] R. Wu, L. Chen, and N. Kioussis, *Structural and magnetic properties of fcc Pt/Fe(111) multilayers*, J. Appl. Phys. **79**, 4783 (1996).
- [138] A. Arrott, *Criterion for Ferromagnetism from Observations of Magnetic Isotherms*, Phys. Rev. **108**, 1394 (1957).
- [139] P. Pouloupoulos, M. Farle, U. Bovensiepen, and K. Baberschke, *Evidence for domain formation near the Curie temperature in ultrathin Ni/Cu (001) films with perpendicular anisotropy*, Phys. Rev. B **55**, R11961 (1997).
- [140] R. Skomski, *Nanomagnetics*, J. Phys.- Condens. Matter **15**, R841 (2003).
- [141] C. Takahashi, M. Ogura, and H. Akai, *First-principles calculation of the Curie temperature Slater-Pauling curve*, J. Phys.- Condens. Matter **19**, 365233 (2007).
- [142] M. Ležaić, Ph. Mavropoulos, and S. Blügel, *First-principles prediction of high Curie temperature for ferromagnetic bcc-Co and bcc-FeCo alloys and its relevance to tunneling magnetoresistance*, Appl. Phys. Lett. **90**, 082504 (2007).
- [143] L. Szunyogh, B. Újfalussy, P. Weinberger, and J. Kollár, *Self-consistent localized KKR scheme for surfaces and interfaces*, Phys. Rev. B **49**, 2721 (1994).
- [144] D. Sander, *The correlation between mechanical stress and magnetic anisotropy in ultrathin films*, Rep. Prog. Phys. **62**, 809 (1999).
- [145] G. Andersson, T. Burkert, P. Warnicke, M. Björck, B. Sanyal, C. Chacon, C. Zlotea, L. Nordström, P. Nordblad, and O. Eriksson, *Perpendicular Magnetocrystalline Anisotropy in Tetragonally Distorted Fe-Co Alloys*, Phys. Rev. Lett. **96**, 037205 (2006).
- [146] A. Kleibert, J. Passig, K.-H. Meiwes-Broer, M. Getzlaff, and J. Bansmann, *Structure and magnetic moments of mass-filtered deposited nanoparticles*, J. Appl. Phys. **101**, 114318 (2007).

- [147] S. Imada, A. Yamasaki, S. Suga, T. Shima, and K. Takanashi, *Perpendicular magnetization of $L1_0$ -ordered FePt films in the thinnest limit*, Appl. Phys. Lett. **90**, 132507 (2007).
- [148] O. Dmitrieva, M. Spasova, C. Antoniak, M. Acet, G. Dumpich, J. Kästner, M. Farle, K. Fauth, U. Wiedwald, H.-G. Boyen, and P. Ziemann, *Magnetic moment of Fe in oxide-free FePt nanoparticles*, Phys. Rev. B **76**, 064414 (2007).
- [149] W. J. Antel, M. M. Schwickert, T. Lin, W. L. O'Brien, and G. R. Harp, *Induced ferromagnetism and anisotropy of Pt layers in Fe/Pt(001) multilayers*, Phys. Rev. B **60**, 12933 (1999).
- [150] P. Ohresser, G. Ghiringhelli, O. Tjernberg, N. B. Brookes, and M. Finazzi, *Magnetism of nanostructures studied by x-ray magnetic circular dichroism: Fe on Cu(111)*, Phys. Rev. B **62**, 5803 (2000).
- [151] M. A. Torija, Z. Gai, N. Myoung, E. W. Plummer, and J. Shen, *Frozen Low-Spin Interface in Ultrathin Fe Films on Cu(111)*, Phys. Rev. Lett. **95**, 027201 (2005).
- [152] P. Ohresser, N. B. Brookes, S. Padovani, F. Scheurer, and H. Bulou, *Magnetism of small Fe clusters on Au(111) studied by x-ray magnetic circular dichroism*, Phys. Rev. B **64**, 104429 (2001).
- [153] K. von Bergmann, S. Heinze, M. Bode, E. Y. Vedmedenko, G. Bihlmayer, S. Blügel, and R. Wiesendanger, *Observation of a Complex Nanoscale Magnetic Structure in a Hexagonal Fe Monolayer*, Phys. Rev. Lett. **96**, 167203 (2006).
- [154] I. Yang, S. Y. Savrasov, and G. Kotliar, *Importance of Correlation Effects on Magnetic Anisotropy in Fe and Ni*, Phys. Rev. Lett. **87**, 216405 (2001).
- [155] D. Weller and A. Moser, *Thermal effect limits in ultrahigh-density magnetic recording*, IEEE Trans. Magn. **35**, 4423 (1999).
- [156] S. Chikazumi, *Physics of ferromagnetism*, Clarendon Press, Oxford, 1997.
- [157] R. Richter and H. Eschrig, *Spin-polarised electronic structure of disordered BCC FeCo alloys from LCAO-CPA*, J. Phys F: Met. Phys. **18**, 1813 (1988).
- [158] R. H. Victora and L. M. Falicov, *Calculated magnetization of iron-cobalt disordered alloys*, Phys. Rev. B **30**, 259 (1984).
- [159] R. H. Victora, L. M. Falicov, and Shoji Ishida, *Calculated surface electronic structure of ferromagnetic iron and the ferromagnetic ordered iron-cobalt alloy*, Phys. Rev. B **30**, 3896 (1984).

- [160] H. A. Dürr and G. van der Laan, *Magnetic circular x-ray dichroism in transverse geometry: Importance of noncollinear ground state moments*, Phys. Rev. B **54**, R760 (1996).
- [161] J. Stöhr, *Exploring the microscopic origin of magnetic anisotropies with X-ray magnetic circular dichroism (XMCD) spectroscopy*, J. Magn. Magn. Mater. **200**, 470 (1999).
- [162] G. H. O. Daalderop, P. J. Kelly, and M. F. H. Schuurmans, *Magnetic anisotropy of a free-standing Co monolayer and of multilayers which contain Co monolayers*, Phys. Rev. B **50**, 9989 (1994).
- [163] S. Demmler, J. Hafner, M. Marsman, and J. Morillo, *Magnetic doping of 4d transition-metal surfaces: A first-principles study*, Phys. Rev. B **71**, 094433 (2005).
- [164] M. A. Tomaz, E. Mayo, D. Lederman, E. Hallin, T. K. Sham, W. L. O'Brien, and G. R. Harp, *Magnetic properties of Co/Rh (001) multilayers studied by x-ray magnetic-circular dichroism*, Phys. Rev. B **58**, 11493 (1998).
- [165] R. Nakajima, J. Stöhr, and Y. U. Idzerda, *Electron-yield saturation effects in L-edge x-ray magnetic circular dichroism spectra of Fe, Co, and Ni*, Phys. Rev. B **59**, 6421 (1999).
- [166] B. Holst, M. Nohlen, K. Wandelt, and W. Allison, *The growth of ultra thin Cu-films on Pt(111), probed by helium atom scattering and scanning tunnelling microscopy*, Surf. Sci. **377-379**, 891 (1997), European Conference on Surface Science.
- [167] B. Holst, M. Nohlen, K. Wandelt, and W. Allison, *Observation of an adlayer-driven substrate reconstruction in Cu-Pt(111)*, Phys. Rev. B **58**, R10195 (1998).
- [168] C. Günther, J. Vrijmoeth, R. Q. Hwang, and R. J. Behm, *Strain Relaxation in Hexagonally Close-Packed Metal-Metal Interfaces*, Phys. Rev. Lett. **74**, 754 (1995).
- [169] F. El Gabaly, J. M. Puerta, C. Klein, A. Saa, A. K. Schmid, K. F. McCarty, J. I. Cerda, and J. de la Figuera, *Structure and morphology of ultrathin Co/Ru(0001) films*, New J. Phys. **9**, 80 (2007).
- [170] E. G. Moroni, G. Kresse, J. Hafner, and J. Furthmüller, *Ultrasoft pseudopotentials applied to magnetic Fe, Co, and Ni: From atoms to solids*, Phys. Rev. B **56**, 15629 (1997).
- [171] B. Hardrat, A. Al-Zubi, P. Ferriani, S. Blügel, G. Bihlmayer, and S. Heinze, *Complex magnetism of iron monolayers on hexagonal transition metal surfaces from first principles*, Phys. Rev. B **79** (2009).

- [172] M. H. Kryder and R. W. Gustafson, *High-density perpendicular recording—advances, issues, and extensibility*, J. Magn. Magn. Mater. **287**, 449 (2005).
- [173] J. Kerr, Philos. Mag. **3**, 321–343 (1877).
- [174] J. Kerr, Philos. Mag. **5**, 161–177 (1878).
- [175] J. P. Pierce, M. A. Torija, Z. Gai, Junren Shi, T. C. Schulthess, G. A. Farnan, J. F. Wendelken, E. W. Plummer, and J. Shen, *Ferromagnetic Stability in Fe Nanodot Assemblies on Cu(111) Induced by Indirect Coupling through the Substrate*, Phys. Rev. Lett. **92**, 237201 (2004).
- [176] M. Faraday, *Experimental Researches in Electricity. Nineteenth Series*, Philos. Trans. R. Soc. London **136**, 1–20 (1846).
- [177] E. Verdet, *Recherches sur les propriétés optiques développées dans les corps transparents par l'action du magnétisme*, Ann. Chim. Phys. **41**, 370 (1854).
- [178] P. N. Argyres, *Theory of the Faraday and Kerr Effects in Ferromagnetics*, Phys. Rev. **97**, 334 (1955).
- [179] A. Kundt, Wied. Ann. **23**, 228 (1884).
- [180] A. Kundt, Wied. Ann. **27**, 191 (1886).
- [181] H. E. J. G. Du Bois, Wied. Ann. **31**, 941 (1887).
- [182] W. Voigt, *Magneto- und Elektrooptik*, Teubner, Leipzig, 1908.
- [183] H. R. Hulme, *The Faraday Effect in Ferromagnetics*, Proc. R. Soc. Lon. Ser.-A **135**, 237 (1932).
- [184] O. Halpern, *Notiz über die Rotationspolarisation ferromagnetischer Festkörper*, Ann. Phys.-Berlin **5**, 181 (1921).
- [185] R. Carey and B. W. J. Thomas, *The theory of the Voigt effect in ferromagnetic materials*, J. Phys. D: Appl. Phys. **7**, 2362 (1974).
- [186] G. Metzger, P. Pluinage, and R. Torguet, *Termes linéaires et quadratiques dans l'effet magnéto-optique de Kerr*, Ann. Phys.-Paris **10**, 5 (1965).
- [187] J. D. Jackson, *Classical Electrodynamics*, John Wiley & Sons, Inc., Hoboken, New York, 1962.
- [188] L. D. Landau and E. M. Lifschitz, *Electrodynamics of Continuous Media*, Course of Theoretical Physics, vol. 8, Pergamon Press, London, Great Britain, 1960.

- [189] L. D. Landau and E. M. Lifschitz, *Statistical Physics*, Course of Theoretical Physics, vol. 5, Pergamon Press, London, Great Britain, 1960.
- [190] Z. Q. Qiu and S. D. Bader, *Surface magneto-optic Kerr effect*, Rev. Sci. Instrum. **71**, 1243 (2000).
- [191] R. Vollmer, *30. IFF Ferienkurs: Magnetische Schichtsysteme*, ch. C7, Institut für Festkörperforschung der Forschungszentrum Jülich GmbH, 1998.
- [192] P. B. Johnson and R. W. Christy, *Optical constants of transition metals: Ti, V, Cr, Mn, Fe, Co, Ni, and Pd*, Phys. Rev. B **9**, 5056 (1974).
- [193] L.G. Schulz, *The Optical Constants of Silver, Gold, Copper, and Aluminum. I. The Absorption coefficient k* , J. Opt. Soc. Am. **44**, 357 (1954).
- [194] L.G. Schulz and F. R. Tangherlini, *The Optical Constants of Silver, Gold, Copper, and Aluminum. I. The Index of Refraction n* , J. Opt. Soc. Am. **44**, 362 (1954).
- [195] Chun-Yeol You and Sung-Chul Shin, *Generalized analytic formulae for magneto-optical Kerr effects*, J. Appl. Phys. **84**, 541 (1998).
- [196] N. Weiss, *Propriétés magnétiques de nanostructures de cobalt adsorbées*, Ph.D. thesis, no. 2980, Ecole Polytechnique Fédérale de Lausanne, 2004.
- [197] G. Baudot, S. Rohart, V. Repain, H. Ellmer, Y. Girard, and S. Rousset, *Temperature dependence of ordered cobalt nanodots growth on Au(7 8 8)*, Appl. Surf. Sci. **212-213**, 360 (2003).
- [198] S. Rohart, V. Repain, A. Tejada, P. Ohresser, F. Scheurer, P. Bencok, J. Ferre, and S. Rousset, *Distribution of the magnetic anisotropy energy of an array of self-ordered Co nanodots deposited on vicinal Au(111): X-ray magnetic circular dichroism measurements and theory*, Phys. Rev. B **73**, 165412 (2006).
- [199] J. V. Barth, H. Brune, G. Ertl, and R. J. Behm, *Scanning tunneling microscopy observations on the reconstructed Au(111) surface: Atomic structure, long-range superstructure, rotational domains, and surface defects*, Phys. Rev. B **42**, 9307 (1990).
- [200] T. Koide, H. Miyauchi, J. Okamoto, T. Shidara, A. Fujimori, H. Fukutani, K. Amemiya, H. Takeshita, S. Yuasa, T. Katayama, and Y. Suzuki, *Direct Determination of Interfacial Magnetic Moments with a Magnetic Phase Transition in Co Nanoclusters on Au(111)*, Phys. Rev. Lett. **87**, 257201 (2001).
- [201] J. J. Lu, H. L. Huang, and I. Klik, *Field orientations and sweep rate effects on magnetic switching of Stoner–Wohlfarth particles*, J. Appl. Phys. **76**, 1726 (1994).

- [202] H. A. Dürr, S. S. Dhesi, E. Dudzik, D. Knabben, G. van der Laan, J. B. Goedkoop, and F. U. Hillebrecht, *Spin and orbital magnetization in self-assembled Co clusters on Au(111)*, Phys. Rev. B **59**, R701 (1999).
- [203] R. W. Chantrell, N. Walmsley, J. Gore, and M. Maylin, *Calculations of the susceptibility of interacting superparamagnetic particles*, Phys. Rev. B **63**, 024410 (2000).
- [204] H. Brune, M. Giovannini, K. Bromann, and K. Kern, *Self-organized growth of nanostructure arrays on strain-relief patterns*, Nature **294**, 451 (1998).
- [205] A. T. N'Diaye, S. Bleikamp, P. J. Feibelman, and T. Michely, *Two-Dimensional Ir Cluster Lattice on a Graphene Moiré on Ir(111)*, Phys. Rev. Lett. **97**, 215501 (2006).
- [206] S. Degen, C. Becker, and K. Wandelt, *Thin alumina films on Ni₃Al(111): A template for nanostructured Pd cluster growth*, Faraday Discuss. **125**, 343 (2004).
- [207] F. Troiani, A. Ghirri, M. Affronte, S. Carretta, P. Santini, G. Amoretti, S. Piligkos, G. Timco, and R. E. P. Winpenny, *Molecular Engineering of Antiferromagnetic Rings for Quantum Computation*, Phys. Rev. Lett. **94**, 207208 (2005).
- [208] M. N. Leuenberger and D. Loss, *Quantum computing in molecular magnets*, Nature **410**, 789 (2001).
- [209] S. Hill, R. S. Edwards, N. Aliaga-Alcalde, and G. Christou, *Quantum Coherence in an Exchange-Coupled Dimer of Single-Molecule Magnets*, Science **302**, 1015 (2003).
- [210] L. Bogani and W. Wernsdorfer, *Molecular spintronics using single-molecule magnets*, Nat. Mater. **7**, 179 (2008).
- [211] M. Corso, W. Auwärter, M. Muntwiler, Anna T., T. Greber, and J. Osterwalder, *Boron Nitride Nanomesh*, Science **303**, 217 (2004).
- [212] R. Laskowski, P. Blaha, T. Gallauner, and K. Schwarz, *Single-Layer Model of the Hexagonal Boron Nitride Nanomesh on the Rh(111) Surface*, Phys. Rev. Lett. **98**, 106802 (2007).
- [213] G. B. Grad, P. Blaha, K. Schwarz, W. Auwärter, and T. Greber, *Density functional theory investigation of the geometric and spintronic structure of h-BN/Ni(111) in view of photoemission and STM experiments*, Phys. Rev. B **68**, 085404 (2003).
- [214] A. Catellani, M. Posternak, A. Baldereschi, and A. J. Freeman, *Bulk and surface electronic structure of hexagonal boron nitride*, Phys. Rev. B **36**, 6105 (1987).

- [215] A. K. Geim and K. S. Novoselov, *The rise of graphene*, Nat. Mater. **6**, 183 (2007).
- [216] A. Goriachko, Y. B. He, and H. Over, *Complex Growth of NanoAu on BN Nanomeshes Supported by Ru(0001)*, J. Phys. Chem. C **112**, 814 (2008).
- [217] F. Nguyen Van Dau C. Chappert, A. Fert, *The emergence of spin electronics in data storage*, Nat. Mater. **6**, 813 (2007).

Acknowledgements

First of all, I thank my advisor Professor Harald Brune who gave me the opportunity to continue studying in his group and to make a PhD thesis. He was available any time for discussion, questions, and wishes. I am very grateful to Stefano Rusponi who was working closely with me on many projects in the laboratory in Lausanne and at different synchrotron radiation sources in Grenoble, Villigen, and Trieste. I learned a lot -anche l'italiano- and appreciated this enjoyable and successful collaboration. I wish to thank Philipp Bulushek for teaching me the laboratory work in Lausanne, Markus Etzkorn for the large contribution to the work on Fe and Co single atoms on Cu_2N , and Safia Ouazi and Géraud Moulas for carrying out the Kerr measurements on $\text{Fe}_x\text{Co}_{1-x}/\text{Pt}(111)$.

Further, I wish to thank the beamline staff for the support before, during, and after the beamtimes and all persons having shared some beamtime with me. Especially, I want to mention the joint project of Fe and Co on Cu_2N with Andreas Heinrich and Cyrus Hirjibehedin from the IBM research lab in Almaden and Pietro Gambardella and Sebastian Stepanow from Barcelona as well as the nightshifts with Emilio Bellingeri and Daniele Marré measuring $Zn_xCo_{1-x}O$ samples.

Un grand merci au personnel technique qui effectue un travail impressionnant. Sans eux la réalisation de nos idées souvent phantasiées n'était pas possible.

Je tiens aussi à remercier tous les autres membres de mon groupe pour une atmosphère agréable pendant et au delà des heures de travail. J'aimerais remercier mes amis physiciens et non-physiciens qui m'ont accueilli chaleureusement à l'EPFL en 2002. Les fidèles des pauses à midi, qui m'ont appris le chibre; les adeptes des soirées à sat et des grillades au bord du lac. Un grand merci à mon équipe de foot et le staff de Yverdon. C'était un grand plaisir découvrir les terrains de foot de toute la Suisse.

Last but not least, möchte ich meinen Eltern, meinem Bruder und meiner Familie danken, die mir eine gute Ausbildung ermöglicht haben, mich immer in meinen Entscheidungen unterstützt haben und jeder Zeit ein offenes Ohr hatten.

Curriculum Vitae

Name: Anne Lehnert
Nationality: German
Date of birth: 23.04.1981

2005 - 2009 PhD studies, Ecole Polytechnique Fédérale de Lausanne (Switzerland)
2005 Research Assistant, University of Aarhus (Denmark)
2000 - 2005 Physics studies, Technische Universität Darmstadt (Germany)
2000 Abitur, Justus - Liebig - Gymnasium Darmstadt (Germany)

Publications

Nucleation of ordered Fe islands on $Al_2O_3/Ni_3Al(111)$, [A. Lehnert](#), A. Krupski, S. Degen, K. Franke, R. Decker, S. Rusponi, M. Kralj, C. Becker, H. Brune, and K. Wandelt, Surf. Sci. **600**, 1804 (2006)

High magnetic moments and anisotropies for Fe_xCo_{1-x} monolayers on $Pt(111)$, G. Moulas, [A. Lehnert](#), S. Rusponi, J. Zabloudil, C. Etz, S. Ouazi, M. Etzkorn, P. Bencok, P. Gambardella, P. Weinberger and H. Brune, Phys. Rev. B **78**, 214421 (2008)

High resolution in situ magneto-optic Kerr effect and scanning tunneling microscopy setup with all optical components in UHV, [A. Lehnert](#), P. Buluschek, N. Weiss, J. Giesecke, M. Treier, S. Rusponi, and H. Brune, Rev. Sci. Instrum. **80**, 023902 (2009)

Opposite Magnetization Axis for Fe and Co Overlayers on $Rh(111)$, [A. Lehnert](#), S. Denmler, S. Rusponi, G. Moulas, M. Etzkorn, J. Hafner, P. Bencok, P. Gambardella, J. Hafner, and H. Brune, Phys. Rev. B in preparation (2009).

Comparison of magnetic anisotropies and moments deduced from atomic scale STS- and from ensemble XMCD-measurements, M. Etzkorn, [A. Lehnert](#), S. Rusponi, S. Ouazi, S. Stepanow, P. Gambardella, C. F. Hirjibehedin, C. P. Lutz, M. Ternes, C. Tieg, P. K. Thakur, A. J. Heinrich, and H. Brune, Phys. Rev. Lett. in preparation (2009).

